USING X-PARAMETERS FOR SIGNAL INTEGRITY APPLICATIONS

BY

THOMAS MATTHEW COMBERIATE

DISSERTATION

Submitted in partial fulfillment of the requirements
for the degree of Doctor of Philosophy in Electrical and Computer Engineering
in the Graduate College of the
University of Illinois at Urbana-Champaign, 2013

Urbana, Illinois

Doctoral Committee:

Professor José E. Schutt-Ainé, Chair
Professor Jennifer T. Bernhard
Professor Andreas C. Cangellaris
Professor Steven J. Franke

ABSTRACT

X-parameters,* the nonlinear extension of scattering parameters, have been shown to have a wide array of applications in the modeling of nonlinear devices and systems. In this dissertation, the use of X-parameters is extended to signal integrity applications, particularly to the modeling of input/output buffers. These input/output buffers are the nonlinear terminations of the high-speed links that the signal integrity engineer is tasked with designing and optimizing. Brief treatments of the X-parameter formalism, the harmonic balance simulation method, the latency insertion method, and the Input/Output Buffer Information Specification (IBIS) are provided as background information along with some examples of how X-parameters are generated via simulation and measurement and used in simulation. Two processes for using X-parameters for signal integrity purposes, lim2x and x2ibis, are described and analyzed in detail.

The process lim2x uses the latency insertion method to perform a transient simulation of a given circuit with specific port stimuli and terminations. It then uses Fourier analysis to extract X-parameters from the simulation results. This process leverages the linear numerical complexity of the latency insertion method to provide a viable X-parameter generation platform that is well-suited for very large, high-frequency circuits, particularly those which are seen in input/output buffers. The lim2x process is demonstrated on a simple buffer circuit. The X-parameters generated from it are compared to those generated with harmonic balance and are shown to be in excellent agreement.

IBIS models are the current standard for modeling input/output buffer circuits. The process x2ibis uses X-parameter models to generate the current-voltage and voltage-time tables used in an IBIS file. This process shows that properly generated X-parameter models contain the information needed to

*"X-parameters" is a registered trademark of Agilent Technologies.

describe the behavior of an input/output buffer. Results are compared with those of another method of IBIS model generation.

Ad majorem Dei gloriam.

In memory of my grandmother, Josephine Comberiate, whose love of music has inspired my faith, and my grandfather, Michael Comberiate, whose study of engineering has inspired my work.
In memory of Philip Edgerly and Daniel Howe, two brothers and fellow University of Illinois students who left this world far too soon. Eternal rest grant unto them, O Lord, and may perpetual light shine upon them. May their souls and the souls of all the faithful departed, through the mercy of God, rest in peace.

I dedicate this dissertation to the hope that each engineer may come to understand that his or her ability to solve problems is a gift from God and a mandate to make the world a better place.

Our Lady of Peace, pray for us!

ACKNOWLEDGMENTS

I am very blessed to have a huge community of supporters, family, and friends. I cannot possibly name all of them, but I would like to acknowledge several directly.

This research was made possible with United States Government support under and awarded by DoD, Air Force Office of Scientific Research, National Defense Science and Engineering Graduate (NDSEG) Fellowship, 32 CFR 168a and the National Science Foundation.

I thank Agilent Technologies Inc. for their financial support of this dissertation and for providing the ADS X-parameter generation platform and the Nonlinear Vector Network Analyzer for X-parameter measurements. I especially thank Eric Iverson, Loren Betts, Steve Fulwider, and David Root from Agilent for their fruitful discussions, insightful comments and helpful suggestions.

I thank my fellow graduate students in the Signal Integrity Group: Pavle Milosevic, Dmitri Klokotov, Patrick Goh, Chia-Lun Cheng, Si Win, Karan Bhagat, Yubo Liu, Da Wei, and especially Xu Chen, Rishi Ratan, and Drew Newell for their camaraderie, their willingness to edit this manuscript, and their patience in answering my questions. I also acknowledge Erica Daly of the Bernhard Research Group at the University of Illinois. Erica is the lead on the project using X-parameters to model the behavior of a varactor diode on which I have happily consulted and assisted. I thank her for allowing me to include the results of our measurement and modeling of the varactor diode with X-parameters in the appendix of this dissertation and I wish her the very best as she continues her work.

I thank Karen Kuhns, Jan Progen, Mandy Wisehart, and the rest of the staff in the Department of Electrical and Computer Engineering for their patience with and compassion for me.

I would also like to thank my doctoral committee members, the four ex-

cellent professors who have advised me over the course of my time at the University of Illinois: Professor Andreas Cangellaris, my undergraduate adviser, Professor Jennifer Bernhard, my senior thesis adviser, Professor Steven Franke, my master's thesis adviser, and especially Professor José Schutt-Ainé, my doctoral advisor. It is my sincere hope that my career reflects well on them and on the reputation of ECE Illinois, my home for eight years.

Last, I would like to thank my family and friends who have supported me throughout my time in graduate school and before. In particular, I would like to thank my mother, Janet, for selflessly sacrificing her career and so much of her time, effort, and sleep to help me become the best version of myself and for encouraging me to leave Maryland to attend the University of Illinois for my undergraduate studies. She is the person most responsible for any good that I might do in this world. I thank my father, Anthony, for developing in me a passion for engineering and for being an example of spotless professional integrity and diligence for me. It is my hope to emulate that example throughout my career. I thank my godparents Tom Hafer and Roberta Ferro for praying for me and supporting me at every opportunity. I thank my older brother Anthony for being a wonderful friend when nobody else could be. I thank my older sister Angela for showing me the power of ambition guided by faith. I thank my older brother Joseph for blazing so many trails for me and for his patient advice. I thank my older brother John for all of the adventures we have shared together and for his continued willingness to reach out to me during both the good and the bad times. I thank my younger brother Dave for teaching me the importance of joy through his witness. I thank my younger brother Dan for his love of beauty and his subtle humor. I thank my brother-in-law Jimmy for his support and encouragement and for asking me to be the godfather of my niece, Jennfier. I thank my sister-in-law Amy for showing us all the value of a smile. I thank my girlfriend Emily for being my sunshine and my love. I look forward to our lives together. I thank the members of the Catholic Illini Community, particularly those involved with the Koinonia retreat program, who have been such a huge part of my life during my time in grad school. I thank Monsignor Gregory Ketcham for all of his moving words and prayers and his example of the servant's heart. I thank Fr. Charles Klamut for his inspiring homilies and music that helped me get through the toughest parts of writing this dissertation. I thank my spiritual director Fr. Jim Pankiewicz for teaching

me the importance of abandoning my will to God. I thank Sr. Loretta Dedomenicis for teaching me the Salesian secret of optimism. I thank my roommates at the Fever House, particularly Brian Miller, Greg Morehouse, Tim Fox, Jason Buenker, Will Hay, Dan Kubacki, Matt Brenner, Colten Maertens, Doug Alleman, and Tim Cohan. Graduate school can easily be the loneliest time in a person's life. You guys have made it awesome. The fraternal fellowship I have experienced with all of you is something that I will carry with me for the rest of my life.

TABLE OF CONTENTS

CHAPTER 1

INTRODUCTION

"There are two kinds of engineers, those that have signal integrity problems and those that will." -Eric Bogatin [1]

1.1 Motivation

Signal integrity is the field of electrical engineering concerned with the accurate transmission of data from one source to another through an interconnect. The classic interconnect of interest in signal integrity, the high-speed link, is shown in Fig. 1.1. The high-speed link is composed of a nonlinear transmitter buffer circuit with packaging and a connector, a channel that consists of some type of transmission line and connection, and a nonlinear receiver buffer circuit with packaging and a connector. The purpose of a high-speed link is to transmit a signal from one circuit to another at a very fast rate with maximum accuracy. The transmitter circuit takes as its input a digital waveform containing information bits in the form of high and low voltages, and it launches an electromagnetic wave encoded with these bits onto the channel. This wave propagates down the channel until it reaches the receiver. The receiver decodes the received electromagnetic wave to recover the transmitted information bits, which can then be used by the rest of the receiver's circuit.

With the rapid increase in computer processing power, a similar growth is occurring in the data transmission speeds of input and output (I/O) buffer circuits. This reality has taken signal integrity from being solely a system-level integration problem to being also a microwave engineering problem. As transmission speeds increase, the waveforms which contain the encoded data begin to contain spectral content at microwave frequencies. This high-frequency content, as it propagates through the channel, suffers from dis-

tortion effects that are typical at microwave frequencies such as dispersion, loss, crosstalk, jitter, and noise. Consequently, the waveforms sent by the transmitter are distorted when they arrive at the receiver. Dispersion is the phenomenon by which different frequency components of a signal propagate through a medium at different velocities. Loss is the attenuation, or drop in magnitude, that occurs to a signal as it propagates through a lossy medium [2]. Both of these effects tend to become more significant when frequency increases. When the microwave energy from one link couples to another due to mutual inductance or mutual capacitance, there is said to be crosstalk between the two links. Often, this coupling is an undesirable effect, but it can be leveraged to improve the performance of the total coupled line system [3]. Jitter is the deviation in time of a signal timing event, such as a bit transition, from its ideal time whereas noise is the deviation in amplitude of a signal from its ideal value [4]. Jitter is time uncertainty and noise is amplitude uncertainty. Both jitter and noise have many different sources. See [1] and [4] for excellent introductions into the studies of jitter and noise.

Overall, dispersion, loss, jitter, noise, and crosstalk can severely limit the maximum rate at which a link can transmit data accurately. These challenges have motivated the evolution of I/O buffers to include portions which perform complicated signal processing functions, such as adaptive equalization or automatic gain control, in order to compensate for signal distortion during data transmission. These new I/O buffers are very large, making full transistor-level simulations of a large number of bits streaming through a high-speed link intractable.

This problem motivates the need for behavioral models of buffers. These behavioral models can be used to perform simplified simulations that are

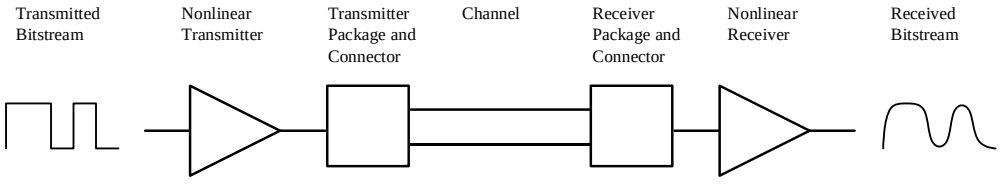

Figure 1.1: The high-speed link is composed of a nonlinear transmitter buffer circuit with packaging and a connector, a channel that consists of some type of transmission line, and a nonlinear receiver buffer circuit with packaging and a connector.

much faster than full transistor-level simulations while still maintaining a high level of accuracy. Because these buffer circuits are so complicated, the process of designing them can be incredibly expensive. Hence, it is very important that any behavioral models of buffers also hide the specific design of the I/O buffer in order to protect the intellectual property (IP) involved in the creation of a functioning high-speed I/O. The Input/Output Buffer Information Specification (IBIS) is the current standard for the behavioral modeling of I/O buffer circuits [5]. IBIS describes an analog equivalent circuit that contains a buffer's DC behavior in both the high and low states and includes some waveforms describing the circuit's switching behavior. IBIS has recently evolved to complement this analog equivalent circuit with an Algorithmic Modeling Interface (AMI) to capture the effects of the signal processing techniques used in high-speed buffers, such as equalization, gain control, and clock/data recovery. The traditional analog IBIS model is also being patched to include methods of modeling new effects, such as simultaneous switching noise (SSN), but there is a desire for a more mathematically robust solution to these new challenges [6].

Frequency-domain modeling and measurement methods are attractive for signal integrity purposes because they offer exceptional accuracy, even at the very high frequencies at which buffers in the near-future will be operating. The use of scattering parameters, a popular frequency-domain modeling tool, has proved incredibly effective as a blackbox model of the linear time-invariant (LTI) components of high-speed links [7]; however, since scattering parameters are only valid for LTI components or small-signal linearizations of nonlinear devices, they provide no assistance in behavioral modeling of the large-signal behavior of nonlinear I/O circuits that compose part of every high-speed link.

X-parameters* [8], a frequency-domain measurement formalism, has been identified as a potential tool for modeling I/O buffers [9]. The purpose of this dissertation is to provide an accessible introduction to the X-parameter formalism and demonstrate its utility in signal integrity applications, particularly modeling I/O circuits. The X-parameter formalism, the mathematically correct large-signal superset of the scattering parameter formalism, is a relation of scattered waves to incident waves based on a linearization of a non-

*"X-parameters" is a registered trademark of Agilent Technologies.

linear system around a dynamic large-signal operating point. X-parameters can be measured with high fidelity using a Nonlinear Vector Network Analyzer (NVNA) [10]. In particular, the novel contributions in this dissertation are a process to generate X-parameters using the latency insertion method, a process to generate IBIS models from X-parameter measurements, and the use of X-parameters to model the steady-state behavior of a buffer circuit directly.

1.2 Outline

This dissertation is organized as follows. Chapter 1 provides the motivation and outline of the dissertation. Chapter 2 is a thorough description of the X-parameter formalism. Chapter 3 provides background on how X-parameters are measured and used as well as some actual measurements and examples. Chapter 4 outlines the signal integrity concepts used in this dissertation, particularly the latency insertion method (LIM) and IBIS.

In Chapter 5, to begin our objective of adapting X-parameters to the signal integrity field, we introduce lim2x, a process for generating X-parameters via simulation based on LIM. LIM is a transient circuit simulation technique that runs in linear time by taking advantage of the inherent latencies in a high-frequency circuit [11]. Because of this, it is ideal for solving the very large, high-frequency I/O buffer circuits simulated in signal integrity problems. The process lim2x provides an alternative for X-parameter generation in simulation, which could previously only be done using harmonic balance (HB), a steady-state circuit simulation technique which is not well-suited for large, high-frequency circuits. We demonstrate the use of LIM as an alternative tool for generating X-parameters and show that lim2x provides results that match those generated from HB.

We next introduce x2ibis, a process in which X-parameter models are used to generate the current-voltage and voltage-time tables used in an Input/Output Buffer Information Specification (IBIS) standard in Chapter 6. In describing the x2ibis process, we outline both the X-parameter model generation that captures the DC and switching behavior of the buffer and the conversion of these models to the tables in an IBIS file in detail. We also validate our results through comparisons with those of other methods of

IBIS model generation. This process demonstrates that X-parameter models contain much of the important information conveyed in an IBIS model. Last, in Chapter 7, we provide a discussion on the use of X-parameters for signal integrity applications as well as some ideas for future work.

CHAPTER 2

X-PARAMETER FORMALISM

In this chapter, we provide a summary of the underlying theory behind the X-parameter formalism through mathematical development and a few insightful examples garnered from the literature. We adopt our notation, along with many useful insights, from the definitive textbook written on X-parameters by Root, Verspecht, Horn, and Marcu [12]. This is an excellent and comprehensive source that should be a large part of any in-depth study of X-parameters. Here we merely provide an introduction to the X-parameter formalism and an overview of the concepts needed to understand some of its less-intuitive aspects.

The discussion begins with a basic description of linear time-invariant electrical networks extending through to the scattering parameter formalism. At that point, we loosen the linear requirement and analyze the behavior of weakly nonlinear electrical networks. Because most engineers are so well-trained and familiar with linear mappings, it can be particularly challenging for an engineer to consider a nonlinear mapping. Deeply ingrained concepts like superposition and "frequency in equals frequency out" are no longer true. However, it is true that the output of many of the memoryless[1] nonlinear devices that we encounter can be modeled as a Taylor series [13]. Because superposition is not valid for a nonlinear mapping, the output from one frequency component in the input depends on all of the other frequency components in the input. This makes characterizing a nonlinear mapping, the purpose of measuring X-parameters, very challenging. In order to make this characterization process feasible, we separate the input to a nonlinear mapping into a large-signal portion and a small-signal portion. For many of the applications that microwave engineers are addressing, such as optimizing the energy efficiency of an amplifier, this large-signal portion is not merely a

[1] A memoryless device is one for which the current value of the output depends only on the current value of its inputs and not any past values.

static bias; rather, it also includes high-frequency components. Our goal, to simplify the characterization of the nonlinear mapping by linearizing it about a large signal, is more challenging because our large-signal operating point is dynamic. To help make this concept more intuitive, we use a canonical example of a simple nonlinear mapping to contrast the difference between linearizing around a static large signal and linearizing around a dynamic large signal. In the process, we show that there is a nonanalytic mapping of small-signal inputs to their corresponding outputs in the dynamic case, that is the small-signal output depends on both the small-signal input and the complex conjugate of the small-signal input. We then demonstrate the linearization of scattering mappings about a dynamic large signal.

Returning to scattering parameters, we then generalize them to nonlinear scattering mappings that have an input composed of a single sinusoid in order to develop the single large-tone X-parameter formalism. We establish the concept of a pseudowave, a harmonic component of a power wave composed of sinusoids that are commensurate, or harmonically related. This leads us to the definition of cross-frequency phase and a study of the time-invariance of nonlinear scattering mappings of pseudowaves. We then use this time-invariant property to simplify the scattering mapping by establishing the phase of the largest input pseudowave as a reference phase.

At this point, we define a conceptually simple X-parameter that strongly depends on all of the incident pseudowaves in the system. While easy to understand, this X-parameter is extremely cumbersome to characterize because it must be evaluated for every different magnitude and phase of each of the input pseudowaves present in the system. In order to simplify this X-parameter into something more manageable, we use the concepts established prior to separate the large-signal input pseudowaves from the small-signal input pseudowaves and linearize the small-signal behavior about that of the large-signal response. This leads us to the single large-tone X-parameter formalism in its fullness. From here, we discuss the process of extracting the X-parameters from measurements, using our canonical nonlinear function example from before.

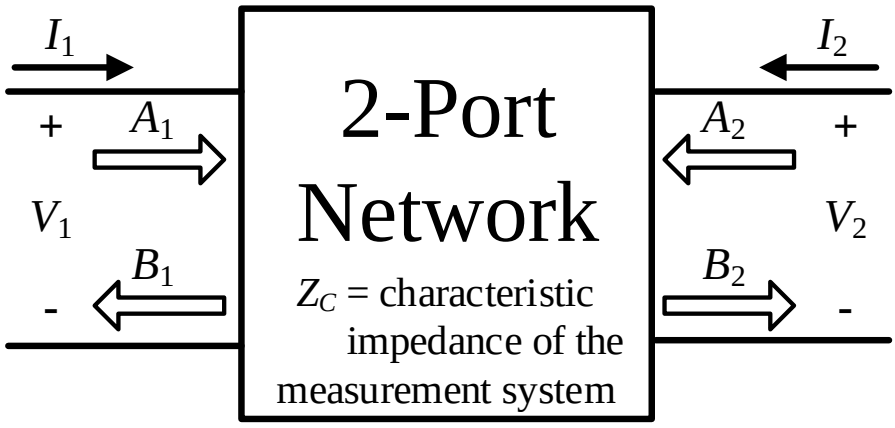

Figure 2.1: Example two-port electrical network with input and output currents, voltages, incident waves, and scattered waves denoted. The characteristic impedance of the measurement system is Z_C.

2.1 Linear Time-Invariant Electrical Networks

The field of network analysis is rich and there are many excellent resources available as references, particularly [13], [14], and [15], so we will only touch briefly on the most relevant points. A two-port network is shown in Fig. 2.1. The most natural way to define a linear time-invariant electrical network is to relate the currents and voltages of the network. When currents are the independent variables, we define an impedance matrix $\mathbf{Z}$ such that

$$\begin{bmatrix} V_1 \\ V_2 \end{bmatrix} = \underbrace{\begin{bmatrix} Z_{11} & Z_{12} \\ Z_{21} & Z_{22} \end{bmatrix}}_{\mathbf{Z}} \begin{bmatrix} I_1 \\ I_2 \end{bmatrix} \tag{2.1}$$

where

$$Z_{ba} = \left. \frac{V_b}{I_a} \right|_{I_c = 0 \,\forall\, c \neq a}. \tag{2.2}$$

So each Z term is determined by taking a ratio of voltage to current with every other port except port a left open. Leaving these other ports, denoted by c, open forces $I_c = 0$ for all but port a, eliminating them from (2.1). This drastically simplifies the equation and makes the goal of determining Z_{ba} trivial. When voltages are the independent variables, we define an admittance

matrix $\mathbf{Y}$ such that

$$\begin{bmatrix} I_1 \\ I_2 \end{bmatrix} = \underbrace{\begin{bmatrix} Y_{11} & Y_{12} \\ Y_{21} & Y_{22} \end{bmatrix}}_{\mathbf{Y}} \begin{bmatrix} V_1 \\ V_2 \end{bmatrix} \tag{2.3}$$

where

$$Y_{ba} = \left.\frac{I_b}{V_a}\right|_{V_c=0\,\forall\, c\neq a}. \tag{2.4}$$

So each Y term is determined by taking a ratio of current to voltage with every port except port a shorted. Shorting these other ports, denoted by c, forces $V_c = 0$ for all but port a, eliminating them from (2.3). Again, this drastically simplifies the equation and makes the goal of determining Y_{ba} trivial.

Impedance and admittance parameters cannot be effectively measured at microwave frequencies; rather, scattering parameters provide the best way to characterize a linear time-invariant network at microwave frequencies for multiple reasons. First, reference impedances like 50 ohms are possible to manufacture over a broad frequency range even at these microwave frequencies (unlike shorts and opens). Second, terminating microwave circuits with shorts or opens often causes their outputs to become unstable, which is very undesirable. The scattering matrix provides a complete description of the network as seen at its ports, just like Z and Y parameters, but while the impedance and admittance matrices relate the total voltages and currents at the ports, the scattering matrix relates the voltage traveling waves incident on the ports to those scattered from the ports

$$A_a = \frac{(V_a + Z_C I_a)}{2\sqrt{Z_C}} \tag{2.5a}$$

$$B_a = \frac{(V_a - Z_C I_a)}{2\sqrt{Z_C}}. \tag{2.5b}$$

Essentially, scattering parameters are a linear transformation of impedance or admittance parameters with incident waves as the independent variables

and scattered waves as the dependent variables

$$\begin{bmatrix} B_1 \\ B_2 \end{bmatrix} = \begin{bmatrix} S_{11} & S_{12} \\ S_{21} & S_{22} \end{bmatrix} \begin{bmatrix} A_1 \\ A_2 \end{bmatrix}. \tag{2.6}$$

In addition, these scattering parameters can be measured directly with the use of a vector network analyzer. For a thorough description of the operation and calibration of a vector network analyzer, see [15].

2.2 Linearization of Nonlinear Mappings

At this point, we divert from the primary focus of this chapter, nonlinear scattering mappings, to discuss in general the concept of a nonlinear mapping and the linearization commonly performed on nonlinear mappings to reduce their complexity to something manageable. We do so in order to motivate the idea of a linearization about a non-static operating point and to show how this leads to a mixing between the large-signal portion and the small-signal portion, both of which are frequency-dependent. This mixing results in the positive and negative frequency portions of the small signal being treated differently in the nonlinear mapping that is linearized about a dynamic operating point. This disparate treatment of positive and negative frequency portions means that the linearized mapping is nonanalytic. Thus the output depends on both the complex phasor of the small signal and its complex conjugate, as we will demonstrate.

The scattering parameter formalism only applies in small-signal, linear time-invariant conditions or those that can be approximated as such. The general form of Y, which is the result of a nonlinear mapping f of the input X is

$$Y = f(X). \tag{2.7}$$

The relationship in (2.7) can be very complicated and thus challenging to characterize or implement. In order to simplify the nonlinear mapping, we often decompose the input X into a large static term X_0 and a time-varying, zero-mean term x, which is much smaller. This leads to a similar decomposition of the output $Y = Y_0 + y$, where $Y_0 = f(X_0)$ and y is the perturbation of the output due to the addition of x. From here, we use a Taylor series

expansion of Y at the point X_0

$$Y = f(X_0) + x \left.\frac{df}{dX}\right|_{X=X_0} + \frac{1}{2}x^2 \left.\frac{d^2f}{dX^2}\right|_{X=X_0} + \ldots + \frac{1}{n!}x^n \left.\frac{d^nf}{dX^n}\right|_{X=X_0} \tag{2.8}$$

to find the part of the output perturbation resulting from the time-varying part of the input to be[2]

$$y = Y - Y_0 = k_1x + k_2x^2 + k_3x^3 + \ldots \tag{2.9}$$

where $k_i = \frac{1}{i!} \left.\frac{d^if}{dx^i}\right|_{X=X_0}$.

2.3 Properties of Weakly Nonlinear Systems with Large-Signal Bias

Of interest to us in this section are weakly nonlinear time-invariant devices. A weakly nonlinear time-invariant device is one whose output signals are a stable, single-valued, and continuous function of the input signals around the large-signal operating point. An example function of a weakly nonlinear device is shown in (2.10) where the output Y is defined as a cubic polynomial function of the input X

$$Y = f(X) = k_1X + k_2X^2 + k_3X^3. \tag{2.10}$$

When we input $X(t) = A_1\cos(\omega_1 t) + A_2\cos(\omega_2 t)$ into (2.10), where $\omega_i = 2\pi f_i$ for each value of i, the output $Y(t)$ contains only spectral components at frequencies which are linear combinations with integer coefficients of f_1 and f_2 as given by [13]

$$f_{\text{out}} = nf_1 + mf_2 \tag{2.11}$$

for integer values of n and m. Frequency components of a signal output of the form nf_1 and mf_2 are referred to as harmonics of f_1 and f_2 respectively. The outputs where both m and n are non-zero are referred to as intermodulation

[2]Note that the expression in (2.9) is not time-invariant. Expressions of this nature are only used in this dissertation for the purpose of explanation of other concepts not related to time-invariance, so we ignore this concern for the sake of simplicity. A similar expression to (2.9) that is time-invariant is $y = k_1x + k_2|x|x + k_3|x^2|x + \ldots$. This expression can be substituted where desired.

products. As we develop our discussion of weakly nonlinear time-invariant devices, we will use (2.10) as a canonical function representing a static algebraic nonlinearity to demonstrate the output for varying inputs, borrowing heavily from the discussion in [16]. These examples will allow us to build toward an understanding of the nonanalytic property of the small-signal portion of the X-parameter formalism and how X-parameters are extracted in modern measurement systems. We will also demonstrate how the outputs of these systems contain spectral components at harmonics of the frequencies present in the input signals.

The first example will consider an input signal $X(t) = X_0(t) + x(t)$, composed of a real DC component and a small tone at frequency $f = \omega/2\pi$,

$$X_0(t) = A_0 \tag{2.12}$$

$$x(t) = \frac{\delta e^{j\omega t} + \delta^* e^{-j\omega t}}{2} = |\delta| \cos(\omega t + \arg(\delta)) \tag{2.13}$$

where A_0 is a purely real number and δ is a small complex phasor which allows for $x(t)$ to have an arbitrary phase. This case is pictured in Fig. 2.2.

We approximate $y(t)$, the linearized response to $x(t)$, to be

$$\begin{aligned} y(t) = Y(t) - Y_0(t) &= f(X_0(t) + x(t)) - f(X_0(t)) \\ &\approx f'(X_0(t))x(t) \end{aligned} \tag{2.14}$$

where the approximations become exact as $x(t) \to 0$. Evaluating $f'(X_0(t))$ at $X_0 = A_0$ yields

$$f'(A_0) = k_1 + 2k_2A_0 + 3k_3A_0^2. \tag{2.15}$$

When we substitute (2.15) into (2.14), we obtain

$$y(t) = (k_1 + 2k_2A_0 + 3k_3A_0^2) \left(\frac{\delta e^{j\omega t} + \delta^* e^{-j\omega t}}{2} \right). \tag{2.16}$$

Observe the coefficient of $e^{j\omega t}$, which is the complex Fourier coefficient of the output at ω, $\hat{y}(\omega)$,

$$\hat{y}(\omega) = \left(\frac{k_1 + 2k_2A_0 + 3k_3A_0^2}{2} \right) \delta. \tag{2.17}$$

Of importance here is the fact that (2.17) is linear with respect to δ, the original magnitude of the input at $e^{j\omega t}$. Equation (2.17) depends nonlinearly

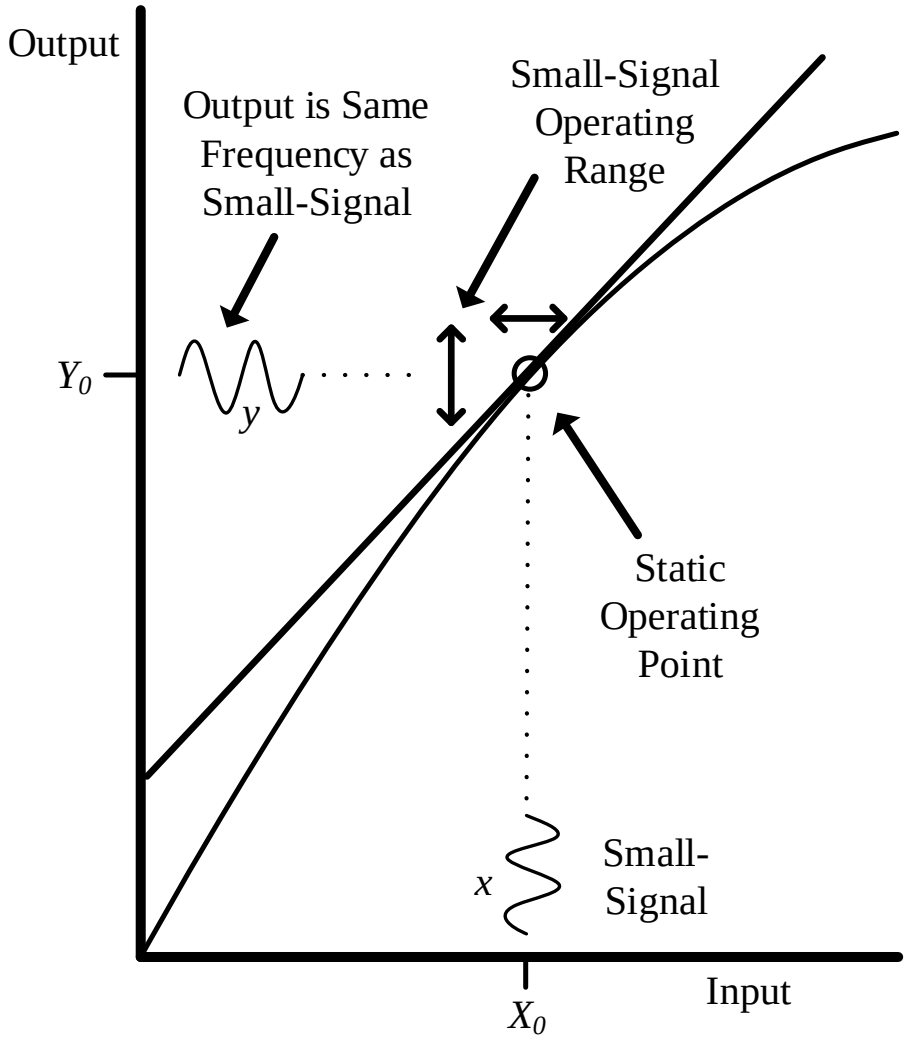

Figure 2.2: A linearization with respect to a DC operating point. There is a linear relationship between the small-signal input and the small-signal output.

on the DC operating point, A_0, but it is linear with respect to the small-signal phase δ. This is the case we encounter when we are measuring small-signal scattering parameters of an amplifier about a DC bias.

Our second example, depicted in Fig. 2.3, adds a large, periodically time-

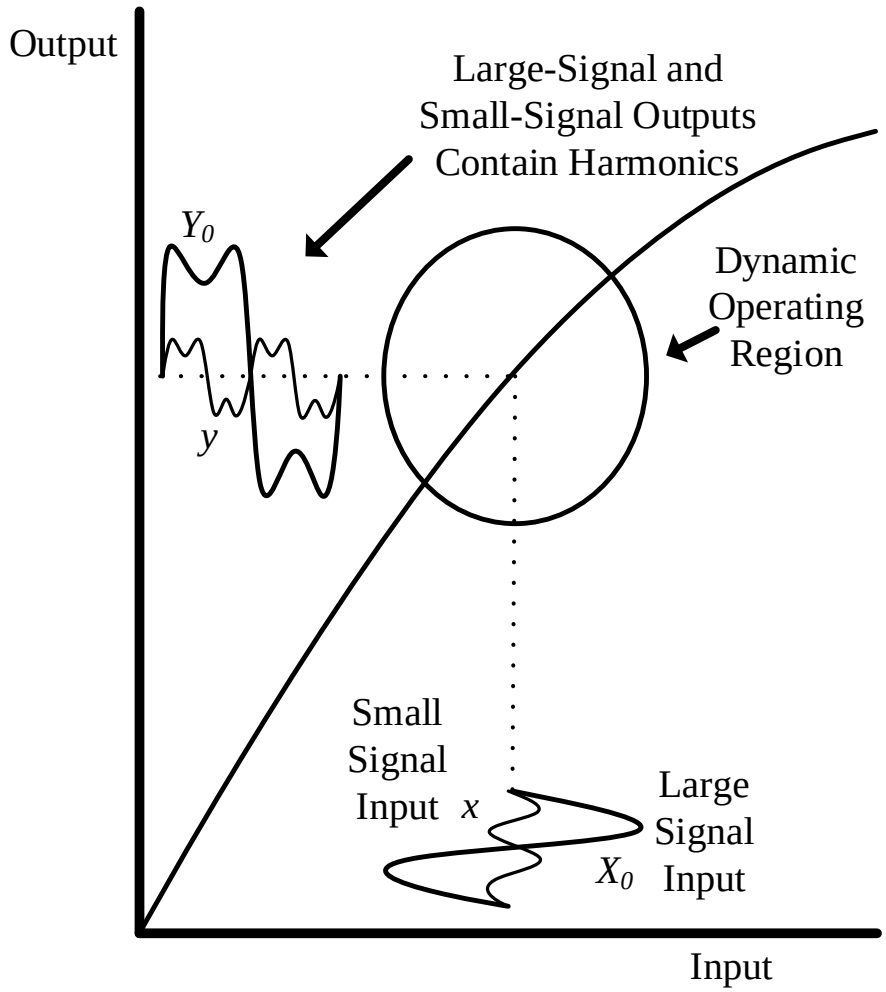

Figure 2.3: A linearization with respect to a large-signal operating point. Both the large-signal output and the small signal output contain harmonics.

varying signal to $X_0(t)$

$$X_0(t) = A_0 + A_1 \cos(\omega t) \tag{2.18}$$

$$x(t) = \frac{\delta e^{j\omega t} + \delta^* e^{-j\omega t}}{2} = |\delta| \cos(\omega t + \arg(\delta)). \tag{2.19}$$

From this, we now find $f'(X_0(t))$ at $X_0(t) = A_0 + A_1 \cos(\omega t)$ equal to

$$
\begin{aligned}
f'(A_0 + A_1\cos(\omega t)) &= \left(k_1 + 2k_2A_0 + 3k_3A_0^2 + \frac{3}{2}k_3A_1^2\right) \\
&\quad + (2k_2A_1 + 6k_3A_0A_1)\cos(\omega t) \\
&\quad + \left(\frac{3}{2}k_3A_1^2\right)\cos(2\omega t) \qquad (2.20)
\end{aligned}
$$

using the trigonometric identity

$$\cos^2(\omega t) = \frac{1}{2} + \frac{\cos(2\omega t)}{2}.$$

Inserting (2.20) into (2.14), we obtain

$$
\begin{aligned}
y(t) &= \left[\left(k_1 + 2k_2A_0 + 3k_3A_0^2 + \tfrac{3}{2}k_3A_1^2\right)\right. \\
&\quad + (2k_2A_1 + 6k_3A_0A_1)\left(\tfrac{e^{j\omega t}+e^{-j\omega t}}{2}\right) \qquad (2.21) \\
&\quad \left. + \tfrac{3}{2}k_3A_1^2\left(\tfrac{e^{j2\omega t}+e^{-j2\omega t}}{2}\right)\right] \times \left(\tfrac{\delta e^{j\omega t}+\delta^* e^{-j\omega t}}{2}\right).
\end{aligned}
$$

Grouping terms by frequency component this becomes

$$
\begin{aligned}
y(t) &= (\beta\delta + \beta\delta^*) + (\alpha\delta + \gamma\delta^*)\,e^{j\omega t} + (\gamma\delta + \alpha\delta^*)\,e^{-j\omega t} \\
&\quad + (\beta\delta)\,e^{j2\omega t} + (\beta\delta^*)\,e^{-j2\omega t} + (\gamma\delta)\,e^{j3\omega t} + (\gamma\delta^*)\,e^{-j3\omega t} \qquad (2.22)
\end{aligned}
$$

where $\alpha = \frac{1}{2}k_1 + k_2A_0 + \frac{3}{2}k_3A_0^2 + \frac{3}{4}k_3A_1^2$, $\beta = \frac{1}{2}k_2A_1 + \frac{3}{4}k_3A_0^2$, and $\gamma = \frac{3}{8}k_3A_1^2$.

Again, observe the coefficient of $e^{j\omega t}$, which is the complex Fourier coefficient of the output at ω, $\hat{y}(\omega)$,

$$\hat{y}(\omega) = \left(\frac{1}{2}k_1 + k_2A_0 + \frac{3}{2}k_3A_0^2 + \frac{3}{4}k_3A_1^2\right)\delta + \left(\frac{3}{8}k_3A_1^2\right)\delta^*. \qquad (2.23)$$

Notice how because (2.20) is a function of ω, the ω and $-\omega$ portions of (2.19) mix differently with (2.20) so that the contribution at ω of the output depends on both the input contribution at ω and the input contribution at $-\omega$. This means that the linearization of this weakly nonlinear mapping around X_0, a time-varying operating point composed of a large tone, is nonanalytic. For the mapping between the small-signal output and the small-signal input to be analytic, (2.23) would depend only on δ, not both δ and δ^*. Essentially, this means the magnitude and phase of the output at ω is a function of the phase relationship between the large-signal biasing tone and the small-signal perturbation tone. This leads to the small-signal output being the sum of a linear mapping of δ and a linear mapping of δ^*.

It is important to note that when $A_1 \to 0$, the large-signal biasing tone disappears and this case collapses into the previous one as the term containing δ^* disappears. Also of note are the (generally nonanalytic) contributions in the output at other harmonics that resulted from the single-frequency input. In the case of a higher-order nonlinearity (perhaps an amplifier driven harder into saturation) and a small-signal input at a harmonic of ω, other output frequencies will have contributions from both δ and δ^*.

Here we have established that a linearization of a nonlinear mapping about a large-signal dynamic operating point results in the sum of a simpler nonlinear mapping of the large-signal input, a linear mapping of the complex phasor of the small-signal portion, and a linear mapping of the complex conjugate of the complex phase of the small-signal portion. Armed with this concept, we reapproach the same idea in the context of nonlinear scattering mappings. We will then use this technique in the development of the X-parameter formalism.

2.4 Linearization of Nonlinear Scattering Mappings

In this section, we perform a linearization of a nonlinear time-invariant scattering mapping. This model simplifies a complicated and difficult to characterize nonlinear mapping into a nonlinear mapping of fewer variables plus a linear mapping of the remaining variables plus a linear mapping of the complex conjugate of these remaining variables. If these remaining variables are small, this linear approximation is valid. We begin this analysis by defining a nonlinear time-invariant scattering mapping $\mathcal{F}$

$$\mathbf{B} = \mathcal{F}(\mathbf{A}) \tag{2.24}$$

where $\mathbf{A}$ and $\mathbf{B}$ are vectors containing the wave coefficients of the large-signal incident and reflected waves as defined in (2.5a) and (2.5b) for all of the different frequency components present in the system. Each wave port may have an arbitrary complex impedance, but in most systems this impedance is real.

When we linearize the system in (2.24) around a stable single-valued and continuous operating point of $\mathcal{F}$, $\mathbf{A} = \mathbf{A}_0 + \mathbf{a}$ and $\mathbf{B} = \mathbf{B}_0 + \mathbf{b}$. $\mathbf{B}_0$ is the

large-signal steady-state response to the large-signal steady-state excitation $\mathbf{A}_0$ and $\mathbf{b}$ is the response to a small excitation signal $\mathbf{a}$ superimposed on $\mathbf{A}_0$.

As shown in the previous example, this mapping is generally nonanalytic so there is no direct matrix relationship between $\mathbf{b}$ and $\mathbf{a}$. However, when the elements of $\mathbf{a}$ and $\mathbf{b}$ are small, we can split them into their real and imaginary parts and approximate their relationships to one another with the Jacobian $\mathbf{J}$ of $\mathcal{F}$, evaluated at $\mathbf{A}_0$ and $\mathbf{B}_0$. This yields

$$\begin{bmatrix} \mathrm{Re}(\mathbf{b}) \\ \mathrm{Im}(\mathbf{b}) \end{bmatrix} \approx \mathbf{J} \begin{bmatrix} \mathrm{Re}(\mathbf{a}) \\ \mathrm{Im}(\mathbf{a}) \end{bmatrix} \equiv \begin{bmatrix} \mathbf{J_{rr}} & \mathbf{J_{ri}} \\ \mathbf{J_{ir}} & \mathbf{J_{ii}} \end{bmatrix} \begin{bmatrix} \mathrm{Re}(\mathbf{a}) \\ \mathrm{Im}(\mathbf{a}) \end{bmatrix} \tag{2.25}$$

where a complex number $X = \mathrm{Re}(X) + j\mathrm{Im}(X)$ and the approximation is only valid when all of the elements of $\mathbf{a}$ are small. The elements of $\mathbf{J}$ are defined as

$$\mathbf{J_{rr}} = \left.\frac{\partial \mathrm{Re}(\mathcal{F}(\mathbf{A}))}{\partial \mathrm{Re}(\mathbf{A})}\right|_{\substack{\mathbf{A}=\mathbf{A}_0 \\ \mathcal{F}(\mathbf{A})=\mathbf{B}_0}} \tag{2.26a}$$

$$\mathbf{J_{ri}} = \left.\frac{\partial \mathrm{Re}(\mathcal{F}(\mathbf{A}))}{\partial \mathrm{Im}(\mathbf{A})}\right|_{\substack{\mathbf{A}=\mathbf{A}_0 \\ \mathcal{F}(\mathbf{A})=\mathbf{B}_0}} \tag{2.26b}$$

$$\mathbf{J_{ir}} = \left.\frac{\partial \mathrm{Im}(\mathcal{F}(\mathbf{A}))}{\partial \mathrm{Re}(\mathbf{A})}\right|_{\substack{\mathbf{A}=\mathbf{A}_0 \\ \mathcal{F}(\mathbf{A})=\mathbf{B}_0}} \tag{2.26c}$$

$$\mathbf{J_{ii}} = \left.\frac{\partial \mathrm{Im}(\mathcal{F}(\mathbf{A}))}{\partial \mathrm{Im}(\mathbf{A})}\right|_{\substack{\mathbf{A}=\mathbf{A}_0 \\ \mathcal{F}(\mathbf{A})=\mathbf{B}_0}} . \tag{2.26d}$$

Next, we define $\mathbf{S}$ and $\mathbf{T}$ as

$$\mathbf{S} = \frac{1}{2}(\mathbf{J_{rr}} + \mathbf{J_{ii}} + j(\mathbf{J_{ir}} - \mathbf{J_{ri}})) \tag{2.27a}$$

$$\mathbf{T} = \frac{1}{2}(\mathbf{J_{rr}} - \mathbf{J_{ii}} + j(\mathbf{J_{ir}} + \mathbf{J_{ri}})) \tag{2.27b}$$

so that (2.25) becomes

$$\mathbf{b} \approx \mathbf{S}\mathbf{a} + \mathbf{T}\mathbf{a}^* \tag{2.28}$$

and the total response $\mathbf{B}$ is approximated

$$\begin{aligned} \mathbf{B} &= \mathbf{B}_0 + \mathbf{b} \\ &= \mathcal{F}(\mathbf{A}) \\ &= \mathcal{F}(\mathbf{A}_0 + \mathbf{a}) \\ &\approx \mathcal{F}(\mathbf{A}_0) + \mathbf{S}\mathbf{a} + \mathbf{T}\mathbf{a}^*. \end{aligned} \tag{2.29}$$

This analysis has been for the case where the phase of $\mathbf{A}_0$ is defined to be zero. This is not an issue when we are working with a single large signal that can be designated as a universal time reference for the system, but for paradigms when there are two or more large tones, this is not sufficient. To generalize this, we note that we can relate the complex frequency-domain vectors of wave coefficients $\mathbf{A}(t)$, $\mathbf{B}(t)$, $\mathbf{A}_0(t)$, $\mathbf{B}_0(t)$, $\mathbf{a}(t)$, or $\mathbf{b}(t)$ at time t to $\mathbf{A}(t_0)$, $\mathbf{B}(t_0)$, $\mathbf{A}_0(t_0)$, $\mathbf{B}_0(t_0)$, $\mathbf{a}(t_0)$, or $\mathbf{b}(t_0)$ at time t_0 with

$$\mathbf{X}(t) = e^{-j\mathbf{\Omega}(t-t_0)}\mathbf{X}(t_0) \tag{2.30}$$

where any of $\mathbf{X}$ can represent any of $\mathbf{A}$, $\mathbf{B}$, $\mathbf{A_0}$, $\mathbf{B_0}$, $\mathbf{a}$, or $\mathbf{b}$ and $\mathbf{\Omega}$ is a diagonal matrix containing the angular frequencies of each of the elements of $\mathbf{X}$. Applying (2.30) in (2.24) yields

$$\mathcal{F}(\mathbf{A}(t)) = e^{-j\mathbf{\Omega}(t-t_0)}\mathcal{F}(\mathbf{A}(t_0)) \tag{2.31}$$

which is consistent with our definition of $\mathcal{F}$ as a time-invariant mapping. Using (2.30) in (2.28), we find that

$$e^{-j\mathbf{\Omega}(t-t_0)}\mathbf{b}(t_0) \approx \mathbf{S}(t)e^{-j\mathbf{\Omega}(t-t_0)}\mathbf{a}(t_0) + \mathbf{T}(t)(e^{-j\mathbf{\Omega}(t-t_0)}\mathbf{a}(t_0))^* \tag{2.32}$$

from which we can solve for $\mathbf{S}(t)$ and $\mathbf{T}(t)$ in terms of $\mathbf{S}(t_0)$ and $\mathbf{T}(t_0)$

$$\mathbf{S}(t) = e^{-j\mathbf{\Omega}(t-t_0)}\mathbf{S}(t_0)e^{+j\mathbf{\Omega}(t-t_0)} \tag{2.33}$$

and

$$\mathbf{T}(t) = e^{-j\mathbf{\Omega}(t-t_0)}\mathbf{T}(t_0)e^{-j\mathbf{\Omega}(t-t_0)}. \tag{2.34}$$

All together, these formulas allow us to change our time reference to any arbitrary value.

2.5 Nonlinear Scattering Mappings of Pseudowaves

Having shown the linearization of a general large-signal scattering mapping, we return now to our scattering parameters from Sec. 2.1, rewriting (2.6) as

$$b_1 = S_{11}a_1 + S_{12}a_2 \tag{2.35}$$

$$b_2 = S_{21}a_1 + S_{22}a_2. \tag{2.36}$$

Because this system is linear, the different frequency content in the incident and scattered waves can be separated from each other and analyzed individually. Thus, without loss of generality, a_1 and a_2 can be said to contain spectral content at only one frequency. The same can be said of b_1 and b_2. Loosening the linear constraint and generalizing to N ports, (2.35) and (2.36) become

$$\begin{aligned} b_1 &= F_1\left(a_1, a_2, \ldots, a_N\right) && (2.37)\\ b_2 &= F_2\left(a_1, a_2, \ldots, a_N\right) && (2.38)\\ &\vdots \\ b_N &= F_N\left(a_1, a_2, \ldots, a_N\right) && (2.39) \end{aligned}$$

where F_1, F_2, ..., F_N are some nonlinear time-invariant mappings of the incident waves at each of the N ports. Loosening the linear constraint carries with it the consequence that a_1, a_2, ..., a_N, b_1, b_2, and b_N can no longer be treated as being made up of a single sinusoid, as the analysis in Sec. 2.3 implies. For the sake of simplicity, we will assume that the incident wave at port 1 is a sinusoid of frequency f_1 expressed as[3]

$$a_1(t) = |A_{1,1}|\cos(2\pi f_1 t + \arg(A_{1,1})) = \Re\left\{A_{1,1}\cdot e^{j2\pi f_1 t}\right\} \tag{2.40}$$

where $A_{1,1}$ is a complex number [12]. From here it follows that all of the energy in the system will be at frequency $f_k = kf_1$ where k is a positive

[3]It is not necessary that the incident wave at port 1 be composed of a single sinusoid. For the one-large-tone X-parameter formalism, we only require that the steady-state portion of a_1 be made up of harmonically related sinusoids, as we also do for the other power waves. For X-parameter formalisms of more than one large tone, even this constraint is lifted.

integer or zero. Hence, the incident wave at port q and the scattered wave at port p can be written as

$$a_q(t) = \sum_{l=1}^{K} |A_{q,l}| \cos\left(2\pi l f_1 t + \arg(A_{q,l})\right) \tag{2.41}$$

$$b_p(t) = \sum_{k=1}^{K} |B_{p,k}| \cos\left(2\pi k f_1 t + \arg(B_{p,k})\right) \tag{2.42}$$

where K is the total number of harmonics that are considered to be non-negligible in the system. As such, we can fully represent $a_q(t)$ by its Fourier coefficients $A_{q,l}$ for each l and $b_p(t)$ by its Fourier coefficients $B_{p,k}$ for each k. Separating (2.37) into these individual Fourier components yields

$$B_{p,k} = F_{p,k}\left(A_{1,1}, A_{1,2}, \ldots, A_{1,K}, A_{2,1}, A_{2,2}, \ldots, A_{2,K}, \ldots, A_{N,1}, A_{N,2}, \ldots, A_{N,K}\right) \tag{2.43}$$

for $p = 1, \ldots, N$ and $k = 1, \ldots, K$. $B_{p,k}$ is sometimes referred to as the scattered pseudowave at the kth harmonic of port p; correspondingly, $A_{q,l}$ is the incident pseudowave at the l harmonic of port q. It should be noted that the scattering parameters mentioned in (2.35) and (2.36) and the nonlinear mapping described in (2.43) both depend on all of the DC voltage or current biases at all of the ports of the device being measured. The incident waves can also produce DC content, but we have omitted all DC behavior for the sake of simplicity. See [12] for a similar analysis that includes the effects of the DC behavior.

2.6 Commensurate Signals and Cross-Frequency Phases

One of the potential issues associated with (2.43) is that it implies a phase relationship between phasors that are at different frequencies (for example, $B_{2,2}$ and $A_{1,1}$). This cross-frequency phase relationship is well-defined provided that the sinusoids the phasors represent are commensurate, meaning that each sinusoid has frequency $f_l = l f_1$ for some positive integer l where f_1 is the fundamental frequency of the set. When a set of sinusoids is commensurate, as is the case for the analysis in Sec. 2.5, all of these sinusoids repeat

with the period of f_1. Hence, since all the signals in a commensurate set have a common period, the cross-frequency phase of a signal in the set can be defined to be its phase at the point where the phase of the fundamental frequency component is equal to zero. Therefore, the fundamental provides a common reference for all of the higher-order harmonics. Because of this common reference, the phase of all the phasors in the system can be consistently defined and a time-domain reconstruction can be made as shown in (2.41) and (2.42) [12].

2.7 Time-Invariance of Nonlinear Scattering Mappings of Pseudowaves

As mentioned before, the nonlinear scattering mapping in (2.43) is time-invariant. This means that if the inputs are all delayed by τ seconds, the outputs will be the same as the output would have been for non-delayed inputs, only delayed by the same τ seconds.

In terms of the frequency domain, this delay is a phase shift. The actual time delay is the same for every frequency component, but in terms of phase, this constant time delay is different for each frequency. A delay of τ seconds is twice the phase delay for the second harmonic as it is for the fundamental; further, it is k times the phase delay for the kth harmonic as it is for the fundamental. Therefore, because the nonlinear mapping $F_{p,k}$ from (2.43) is time-invariant, it must satisfy this property

$$\begin{aligned} &F_{p,k}\left(A_{1,1}e^{j\theta}, A_{1,2}(e^{j\theta})^2, \ldots, A_{1,K}(e^{j\theta})^K, \ldots\right) \\ &\qquad = F_{p,k}\left(A_{1,1}, A_{1,2}, \ldots, A_{1,K}, \ldots\right)(e^{j\theta})^k \end{aligned} \tag{2.44}$$

for real values of θ [12]. Note how each element was shifted by the same time, resulting in the output being shifted by the same time as well. This property is particularly useful because it allows us to separate the magnitude and phase dependence of one of the arguments in the mapping in (2.43) by making the phase shift equal to the inverse of that argument's phase. We do so for $A_{1,1}$, the fundamental frequency term at port 1, by setting θ in (2.44)

equal to $-\arg(A_{1,1})$ to give

$$F_{p,k}\left(|A_{1,1}|, A_{1,2}(e^{-j\arg(A_{1,1})})^2, \ldots, A_{1,K}(e^{-j\arg(A_{1,1})})^K, \ldots\right) = F_{p,k}\left(A_{1,1}, A_{1,2}, \ldots, A_{1,K}, \ldots\right)(e^{-j\arg(A_{1,1})})^k \quad (2.45)$$

since $|A_{1,1}| = A_{1,1}e^{-j\arg(A_{1,1})}$. The convention is to define a variable P such that

$$P = e^{j\arg(A_{1,1})} \quad (2.46)$$

and (2.45) becomes

$$F_{p,k}\left(A_{1,1}, A_{1,2}, \ldots, A_{1,K}, \ldots\right) = F_{p,k}\left(|A_{1,1}|, A_{1,2}P^{-2}, \ldots, A_{1,K}P^{-K}, \ldots\right)P^k. \quad (2.47)$$

Taking the dependence of the phase of $A_{1,1}$ out of the argument of $F_{p,k}$ reduces the overall dimensionality of the space over which $F_{p,k}$ needs to be characterized.

2.8 Single Large-Tone X-Parameter Power Wave Relationship

We can now define a generalized X-parameter of type FB as

$$X_{p,k}^{(FB)}\left(|A_{1,1}|, A_{1,2}P^{-2}, \ldots, A_{1,K}P^{-K}, \ldots\right) = \frac{F_{p,k}\left(A_{1,1}, A_{1,2}, \ldots, A_{1,K}, \ldots\right)}{P^k}. \quad (2.48)$$

This makes (2.43)

$$B_{p,k} = X_{p,k}^{(FB)}\left(|A_{1,1}|, A_{1,2}P^{-2}, \ldots, A_{1,K}P^{-K}, \ldots\right)P^k. \quad (2.49)$$

This is the conceptually simplest set of X-parameters, one for which the X-parameter terms of type FB depend on the magnitude of $A_{1,1}$ and the magnitude and phase of all of the other incident pseudowaves [12]. Generally, these are difficult to characterize. This characterization would involve measuring the $X_{p,k}^{(FB)}$ parameter at every desired permutation of magnitude and phase of every combination of incident port and harmonic. While this

might be tractable for two ports and three harmonics, it rapidly becomes unwieldy for larger numbers. The reality of most applications is that all of the incident pseudowaves except $A_{1,1}$ are small. Thus, it becomes reasonable to use an approximation to simplify (2.47) and (2.49) into something more manageable while sacrificing minimal accuracy.

At this point, we employ the linearization outlined in Sec. 2.4, treating $|A_{1,1}|$ as the only large incident pseudowave and the other incident pseudowaves as the small signal. We linearize the mapping in (2.47) with respect to $A_{1,2}P^{-2}$, ..., $A_{1,K}P^{-K}$, ... individually all at $(|A_{1,1}|, 0, \ldots, 0, \ldots)$, taking into account the nonanalytic nature of the small-signal response resulting from this linearization. This builds the approximation

$$\begin{aligned} B_{p,k} &= F_{p,k}\left(|A_{1,1}|, A_{1,2}P^{-2}, \ldots, A_{1,K}P^{-K}, \ldots\right) P^k \\ &\approx F_{p,k}\left(|A_{1,1}|, 0, \ldots, 0, \ldots\right) P^k \\ &+ \sum_{\substack{q=1,l=1 \\ (q,l)\neq 1}}^{q=N,l=K} \left[\left.\frac{\partial F_{p,k}}{\partial\left(A_{q,l}P^{-l}\right)}\right|_{|A_{1,1}|} A_{q,l}P^{k-l} + \left.\frac{\partial F_{p,k}}{\partial\left(\left(A_{q,l}P^{-l}\right)^*\right)}\right|_{|A_{1,1}|} {A_{q,l}}^* P^{k+l} \right] \end{aligned} \tag{2.50}$$

which is only valid when $A_{1,2}P^{-2}, \ldots, A_{1,K}P^{-K}, \ldots$ are small. Following the example from Sec. 2.4, we define these partial derivatives as X-parameters of type S as

$$X^{(S)}_{p,k;q,l} \equiv \left.\frac{\partial F_{p,k}}{\partial\left(A_{q,l}P^{-l}\right)}\right|_{|A_{1,1}|} = \left.\frac{\partial F_{p,k}}{\partial\left(A_{q,l}\right)}\right|_{|A_{1,1}|} P^l \tag{2.51}$$

and type T as

$$X^{(T)}_{p,k;q,l} \equiv \left.\frac{\partial F_{p,k}}{\partial\left(A_{q,l}P^{-l}\right)^*}\right|_{|A_{1,1}|} = \left.\frac{\partial F_{p,k}}{\partial\left({A_{q,l}}^*\right)}\right|_{|A_{1,1}|} P^{-l}. \tag{2.52}$$

We then define a new X-parameter of type FB for when all the incident pseudowaves except $A_{1,1}$ are zero as

$$X^{(FB)}_{p,k}\left(|A_{1,1}|\right) = F_{p,k}\left(|A_{1,1}|, 0, \ldots, 0, \ldots\right). \tag{2.53}$$

From incorporating (2.51), (2.52), and (2.53) in (2.50), we arrive at the

power wave relationship [17]

$$
\begin{aligned}
B_{p,k} &= X^{(FB)}_{p,k}(|A_{1,1}|, DC, f) \cdot P^k \\
&+ \sum_{\substack{q=1,l=1 \\ (q,l)\neq(1,1)}}^{q=N,l=K} X^{(S)}_{p,k;q,l}(|A_{1,1}|, DC, f) \cdot A_{q,l} \cdot P^{k-l} \\
&+ \sum_{\substack{q=1,l=1 \\ (q,l)\neq(1,1)}}^{q=N,l=K} X^{(T)}_{p,k;q,l}(|A_{1,1}|, DC, f) \cdot A^*_{q,l} \cdot P^{k+l}
\end{aligned} \tag{2.54}
$$

where $A_{q,l}$ is the contribution from the incident wave of the lth harmonic at port q, $A^*_{q,l}$ is its complex conjugate, and $B_{p,k}$ is the contribution from the scattered wave of the kth harmonic at port p. $X^{(FB)}_{p,k}$ is a scattering parameter of type FB that accounts for the contribution from the large-amplitude input tone at the fundamental frequency, $A_{1,1}$, to the kth harmonic of port p for a system in which all the other incident pseudowaves are zero. All the other incident pseudowaves being equal to zero is equivalent to the system being perfectly matched at each harmonic at each point. The X-parameter of type FB has the same units as the scattered and incident waves. $X^{(S)}_{p,k;q,l}$ is a scattering parameter of type S that accounts for the contribution to the kth harmonic of the scattered wave at port p from the lth harmonic of the incident wave at port q. $X^{(T)}_{p,k;q,l}$ is a scattering parameter of type T that accounts for the contribution to the kth harmonic of the scattered wave at port p from the lth harmonic of the conjugate of the incident wave at port q. Intuitively, these parameters determine the circuit's sensitivity to mismatch to the system impedance at the kth harmonic of port p. The X-parameters of types S and T are ratios of power waves and thus, like traditional scattering parameters, unitless. DC is the DC voltage or current biasing and f is the fundamental frequency. We include them here to clarify that all of these parameters depend on the fundamental frequency and any DC biases in addition to the magnitude of the input at the fundamental frequency. $P = e^{j \cdot \arg(A_{1,1})}$ is a pure phase term that compensates for the magnitude-only dependence of $A_{1,1}$ on the X-parameters to ensure the time-invariance of the model. N is the total number of ports and K is the total number of harmonics. These X-parameters together characterize the nonlinear dynamics of the network of interest with a large-signal operating point at a particular input fundamental frequency and power. There are additional X-parameters that model the DC

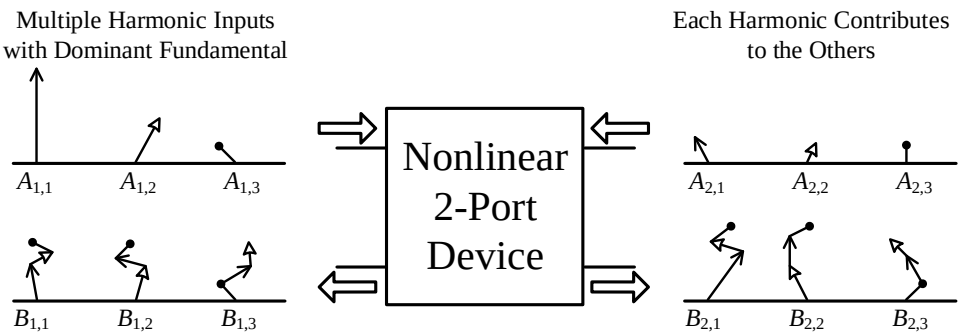

Figure 2.4: The single large-tone X-parameter formalism relates the scattered waves to the incident waves on the basis of a linearization around $A_{1,1}$ such that the harmonics add linearly on top of the large signal operating point.

biases' sensitivity to the incident waves, but these are outside the scope of this dissertation [12]. Note that because X-parameters depend on the large-signal fundamental input, they are inherently unidirectional. Figure 2.4 provides a visualization of the single large-tone X-parameter power wave relationship.

2.9 Extraction of X-Parameters from Measurements

Returning to the example device from (2.10) in Sec. 2.3, we would like to analyze it again within the context of the X-parameter formalism defined in Sec. 2.8. In the process, we will extend our example to provide some insight into how X-parameters are measured and extracted in the laboratory.

Revisiting (2.23), the complex output Fourier coefficient at ω, we take the ratio of it to the complex input Fourier coefficient, $\hat{x}(\omega) = \delta^*$, to find

$$\frac{\hat{y}(\omega)}{\hat{x}(\omega)} = \left(\frac{1}{2}k_1 + k_2 A_0 + \frac{3}{2}k_3 A_0^2 + \frac{3}{4}k_3 A_1^2\right) + \left(\frac{3}{8}k_3 A_1^2\right) e^{-j2\arg(\delta)}. \quad (2.55)$$

If we consider the input x to be port 1 and the output y to be port 2, (2.55) is

$$\frac{\hat{y}(\omega)}{\hat{x}(\omega)} = X^{(S)}_{2,1;1,1} + X^{(T)}_{2,1;1,1}\left(e^{-j2\arg(\delta)}\right). \quad (2.56)$$

Therefore, to isolate the S- and T-parameters, one would have to measure the value of (2.55) for at least two difference phases of δ. This was the

original technique for extracting X-parameters from measurements [18], but the measurement technique has since been simplified to require only one measurement. We will outline this improved technique [19] by extending this example.

In order to do so, we replace (2.19) with a slightly more complicated expression

$$x(t) = \frac{\delta e^{j(l\omega+\epsilon)t} + \delta^* e^{-j(l\omega+\epsilon)t}}{2} = |\delta| \cos\left[(l\omega+\epsilon)\, t + \arg(\delta)\right]. \tag{2.57}$$

This expression allows for the small perturbation tone to be at the lth harmonic of the large tone with a small frequency offset of ϵ. With this new perturbation tone, (2.21) becomes

$$\begin{aligned} y(t) \;=\; & \Big[\big(k_1 + 2k_2A_0 + 3k_3A_0^2 + \tfrac{3}{2}k_3A_1^2\big) \\ & + (2k_2A_1 + 6k_3A_0A_1)\left(\tfrac{e^{j\omega t}+e^{-j\omega t}}{2}\right) \\ & + \tfrac{3}{2}k_3A_1^2\left(\tfrac{e^{j2\omega t}+e^{-j2\omega t}}{2}\right)\Big] \times \left[\tfrac{\delta e^{j(l\omega+\epsilon)t}+\delta^* e^{-j(l\omega+\epsilon)t}}{2}\right]. \end{aligned} \tag{2.58}$$

Expanding this expression using the same α, β, and γ as before, we find

$$\begin{aligned} y(t) \;=\; & \alpha\delta e^{j(l\omega+\epsilon)t} + \alpha\delta^* e^{j(-l\omega-\epsilon)t} \\ & + \beta\delta e^{j[(l+1)\omega+\epsilon]t} + \beta\delta e^{j[(l-1)\omega+\epsilon]t} \\ & + \beta\delta^* e^{j[-(l-1)\omega-\epsilon]t} + \beta\delta^* e^{j[-(l+1)\omega-\epsilon]t} \\ & + \gamma\delta e^{j[(l+2)\omega+\epsilon]t} + \gamma\delta e^{j[(l-2)\omega+\epsilon]t} \\ & + \gamma\delta^* e^{j[-(l-2)\omega-\epsilon]t} + \gamma\delta^* e^{j[-(l+2)\omega-\epsilon]t}. \end{aligned} \tag{2.59}$$

This expression has several interesting properties. First, it is purely real as it is the product of two purely real expressions. Second, the additional ϵ term creates sidebands around integer values of ω in the frequency domain. This separates the δ and δ^* terms, making the former the upper sideband and the latter the lower sideband. This is useful because it prevents the X-parameters of types S and T from aliasing on top of each other. Therefore, when we set $l = 1$, we find that

$$\frac{\hat{y}(\omega+\epsilon)}{\hat{x}(\omega+\epsilon)} = X^{(S)}_{2,1;1,1} = \frac{1}{2}k_1 + k_2A_0 + \frac{3}{2}k_3A_0^2 + \frac{3}{4}k_3A_1^2 \tag{2.60}$$

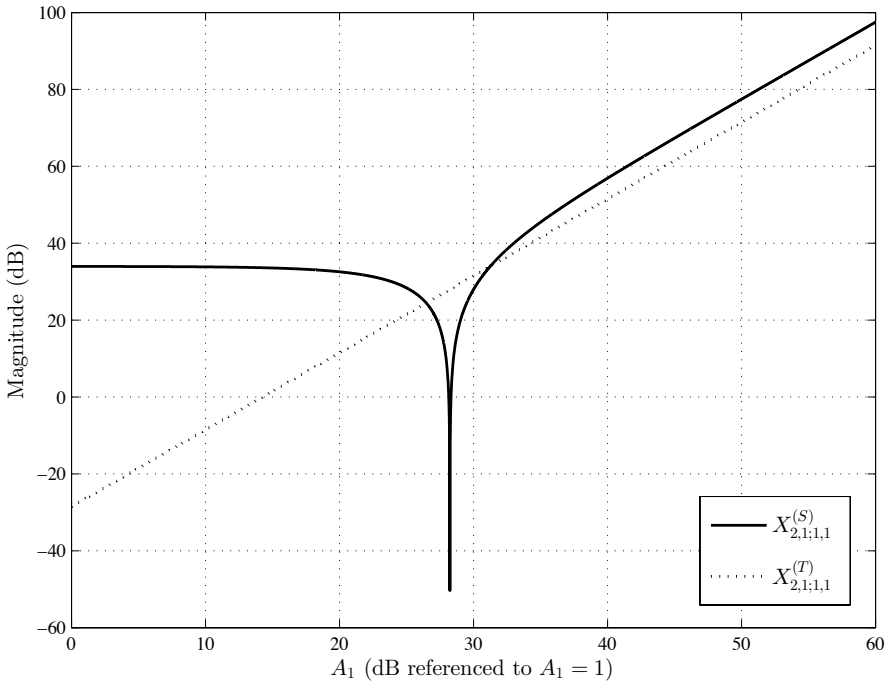

Figure 2.5: Plot of $X^{(S)}_{2,1;1,1}$ and $X^{(T)}_{2,1;1,1}$ for $k_1 = 100$, $k_2 = 0$, $k_3 = -0.01$, and $A_0 = 0$ for multiple values of large-tone input power, A_1.

and

$$\frac{\hat{y}(\omega - \epsilon)}{\hat{x}(\omega + \epsilon)} = X^{(T)}_{2,1;1,1}\left(e^{-j2\arg(\delta)}\right) = \frac{3}{8}k_3 A_1^2\left(e^{-j2\arg(\delta)}\right). \tag{2.61}$$

The S- and T-parameters are separated and we only require one measurement of $y(t)$ to extract both. In addition, the phase of the small-signal can be arbitrary, provided that we can measure it. Figure 2.5 shows a plot of $X^{(S)}_{2,1;1,1}$ and $X^{(T)}_{2,1;1,1}$ for specific values of the input parameters that reflect an amplifier with a weak cubic nonlinearity. Note how $X^{(T)}_{2,1;1,1} \to 0$ as $A_1 \to 0$. As the input power of the large tone decreases, the X-parameter formalism collapses into the small-signal, linear S-parameter formalism because all of the T-parameters and the cross-frequency terms are proportional to the power of the large tone.

The large-signal output can be extracted very simply by eliminating the small-signal input $x(t)$ and examining $Y_0(t) = f(X_0(t))$. When $X_0(t)$ is

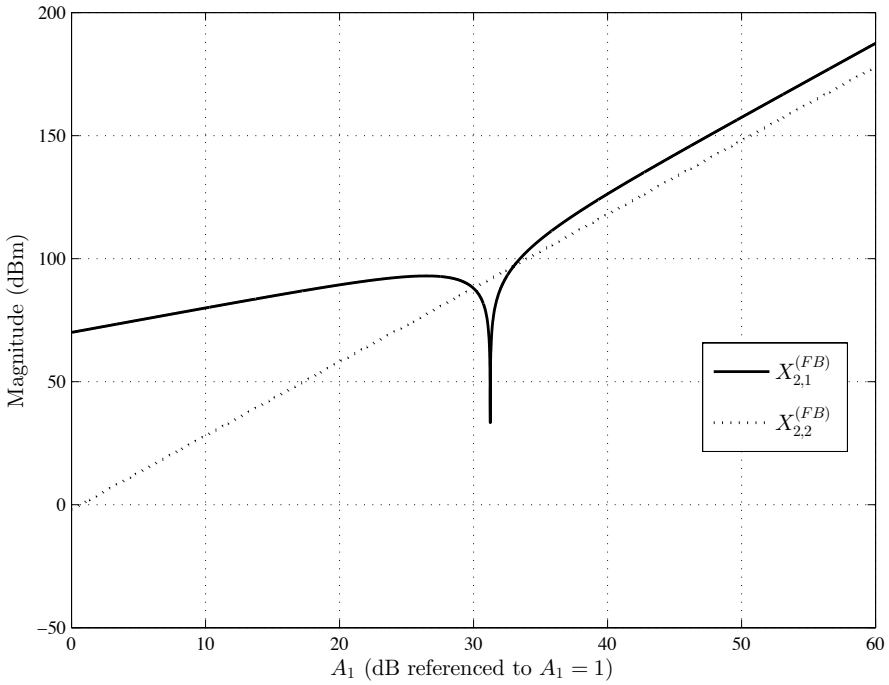

Figure 2.6: Plot of $X_{2,1}^{(FB)}$ and $X_{2,3}^{(FB)}$ for $k_1 = 100$, $k_2 = 0$, $k_3 = -0.01$, and $A_0 = 0$ for multiple values of large-tone input power, A_1.

specified as in (2.18), the large-signal output is

$$\begin{aligned} Y_0(t) &= k_1 A_0 + k_2 \left({A_0}^2 + \frac{A_1^2}{2} \right) + k_3 \left(A_0^3 + \frac{A_0 A_1^2}{2} + A_0 A_1^2 \right) \\ &\quad + \left[k_1 A_1 + 2 k_2 A_0 A_1 + k_3 \left(2 A_0^2 A_1 + A_0^2 A_1 + \frac{3}{4} A_1^3 \right) \right] \cos \omega t \\ &\quad + \left[k_2 \frac{A_1^2}{2} + k_3 \left(\frac{A_0 A_1^2}{2} + A_0 A_1^2 \right) \right] \cos 2\omega t \\ &\quad + \left(k_3 \frac{A_1^3}{4} \right) \cos 3\omega t \end{aligned} \tag{2.62}$$

which is easily separated into its frequency components. Figure 2.6 shows a plot of $X_{2,1}^{(FB)}$ and $X_{2,3}^{(FB)}$ for the same parameter values as in Fig. 2.5.

CHAPTER 3

USING X-PARAMETERS

Since we have developed the single large-tone X-parameter formalism in Chapter 2, we now explain some practical aspects behind the use of X-parameters. We begin by describing the process of measuring X-parameters in the laboratory. We then provide some background on harmonic balance (HB), the circuit simulation technique used to generate X-parameters in simulation. HB is also the technique used to generate the steady-state results of a nonlinear microwave circuit that includes X-parameter models. We next describe the circuit envelope (CE) simulation technique, which is an extension of HB. Then we outline the procedure for cascading two two-port X-parameter blocks together, first providing background on how to cascade two two-port S-parameter blocks together.

Next, we provide some examples of X-parameter measurements as well as their use in simulation. The first example involves measuring a power amplifier (PA). We begin by plotting various X-parameters of the amplifier and providing some intuition of their physical meaning. We then demonstrate the use of a CE simulation to approximate the intermodulation distortion power values for varying input powers. The next example is the X-parameter measurement of a transmitter with and without an equalization branch. We plot its large-signal X-parameters for both cases and discuss its level of nonlinearity during normal operation. We then show an HB simulation using the X-parameter model of the buffer with a sinusoidal input that matches the steady-state output generated from a transient simulation of the transistor-level model of the buffer with the same input.

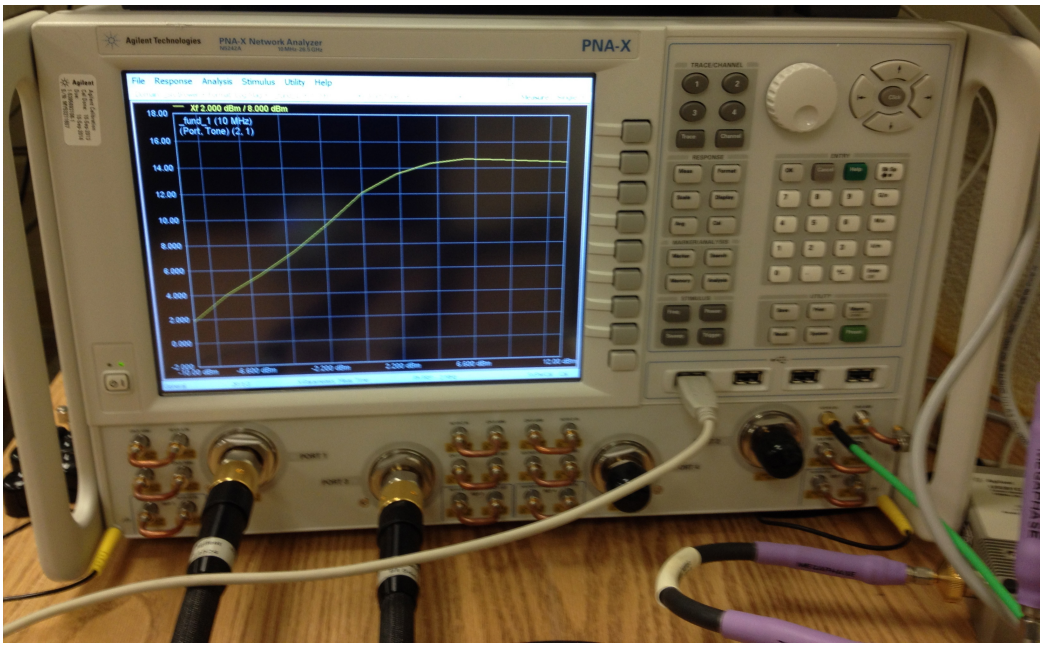

Figure 3.1: Agilent PNA-X. This network analyzer has two microwave sources and is capable of measuring nonlinear figures of merit such as intermodulation distortion (IMD) as well as frequency conversion measurements, such as mixer conversion gain. With the addition of a phase reference, the PNA-X can be used as an NVNA.

3.1 Laboratory Measurement of X-Parameters

X-parameters can be measured in the laboratory with a nonlinear vector network analyzer (NVNA) [10]. An NVNA is based on the same form factor as a PNA-X, a Vector Network Analyzer (VNA) that has two filtered microwave sources and an internal combiner, pictured in Fig. 3.1. The PNA-X on its own can use these two microwave sources to measure some nonlinear device figures of merit such as intermodulation distortion (IMD) or mixer conversion gain. Because a nonlinear system can no longer rely on the linear properties of homogeneity and superposition, any accurate measurement of a nonlinear figure of merit requires absolute power measurements. These absolute power measurements are calibrated with the use of an external power meter, pictured in Fig. 3.2. All of the nonlinear measurements made with the PNA-X are scalar because it is unable to capture cross-frequency phase information.

The additions to a PNA-X that turn it into an NVNA are designed to solve this problem and allow the device to capture cross-frequency phase re-

Figure 3.2: This power meter is used to measure the absolute power being sourced by the PNA-X. Unlike linear PNA-X measurements which leverage the linear property of homogeneity and measure the ratio of scattered to incident waves, all nonlinear PNA-X measurements require an amplitude calibration because these measurements are nonratioed.

lationships between incident and scattered waves [20]. The key addition is a phase reference repetitive-pulse generator, as pictured in Fig. 3.3. Theoretically, any stable source whose output contains spectral energy at multiple frequencies can be used as a phase reference [12]. This repetitive-pulse generator takes in a sinusoid at frequency f and generates an impulse repeating at that frequency. This time-domain impulse train is an impulse train in the frequency domain with its impulses at $n \cdot f$ for all integer values of n, having an appearance similar to the bristles of a comb. Most importantly, the phase relationship between the different harmonics at the output of the repetitive-pulse generator is constant versus input drive frequency and power. Thus, the repetitive-pulse generator can provide a static cross-frequency phase reference for a variety of measurement scenarios. Other examples of potential phase references would be devices that take in a sinusoid and output a square wave, a triangle wave, or a sawtooth wave. The repetitive-pulse generator is preferred to these other potential phase references because its frequency output spectrum decreases more slowly in magnitude with respect to increasing output frequency and includes both even and odd harmonics [12].

In the NVNA, a separate signal generator sources two phase reference repetitive-pulse generators. The input frequency to these repetitive-pulse generators is planned carefully so that every frequency seen at the output of the DUT—harmonics, intermods, mixing products, etc.—will have a corresponding harmonic component at the same frequency in the output of the repetitive-pulse generators. The output of the first repetitive-pulse generator is connected to a receiver in the NVNA, where it is used as an absolute phase

Figure 3.3: Repetitive-pulse generator (also referred to as a comb generator) that serves as a phase reference for cross-frequency phase measurements.

reference for all of the incident and scattered test signals. During phase calibration, the second repetitive-pulse generator is connected to the NVNA test port that will provide the large-signal stimulus to the input of the DUT. This is used to calibrate the cross-frequency phase relationships at the device plane [21].

Maintaining an accurate, static, cross-frequency phase relationship allows the NVNA to make vector measurements across different frequencies. This allows for the conversion of the nonlinear frequency-domain measurements to the time domain as well as the generation of accurate distortion models for a device.

The calibration of an NVNA is a three-step process. The first step is the aforementioned phase calibration to measure cross-frequency phase. The second is an amplitude calibration using a power meter to calibrate the microwave sources and receivers of the NVNA. Last, the NVNA performs a vector error correction, usually made using an Electronic Calibration (ECal) Module like the one pictured in Fig. 3.4, to move the reference planes of the measurement to the ports of the device under test (DUT).

This vector error correction in NVNA measurements is different from that

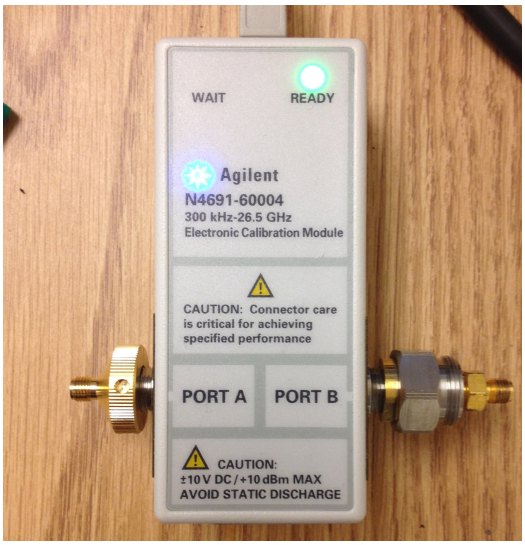

Figure 3.4: Electronic Calibration (ECal) Module used to perform vector error correction for NVNA measurements.

of a typical VNA. A typical VNA uses the error model in Fig. 3.5 [15]. Because of the superposition property of linear devices and the fact that the stimuli needed for S-parameter extraction are only applied at one port at a time, the forward and reverse error models can be separated to form the ten-term error model, each direction being comprised of five error terms. This error model compensates for errors caused by imperfections in the VNA measurement components, imperfect directivity, reflectivity, and transmission tracking, and source and load mismatch. To minimize the number of terms in the model, the error model combines the e_{1f}^{10} and e_{1f}^{01} terms and the e_{2r}^{10} and e_{2r}^{01} by normalizing one parameter to unity. This is possible because a VNA only makes ratios of power waves so no absolute measurements are needed.

The NVNA needs to be able to measure absolute power and cross-frequency phase and it does not assume that the DUT has linear behavior. Thus, no error terms can be normalized or combined. Since stimuli in X-parameter measurements are often simultaneously applied to both input and output ports, the error model can no longer be separated into forward and reverse portions. Because of all of this, the NVNA uses a single eight-term error model, as shown in Fig. 3.6 [12]. After calibration is completed, X-parameters can be measured as described in Sec. 2.9.

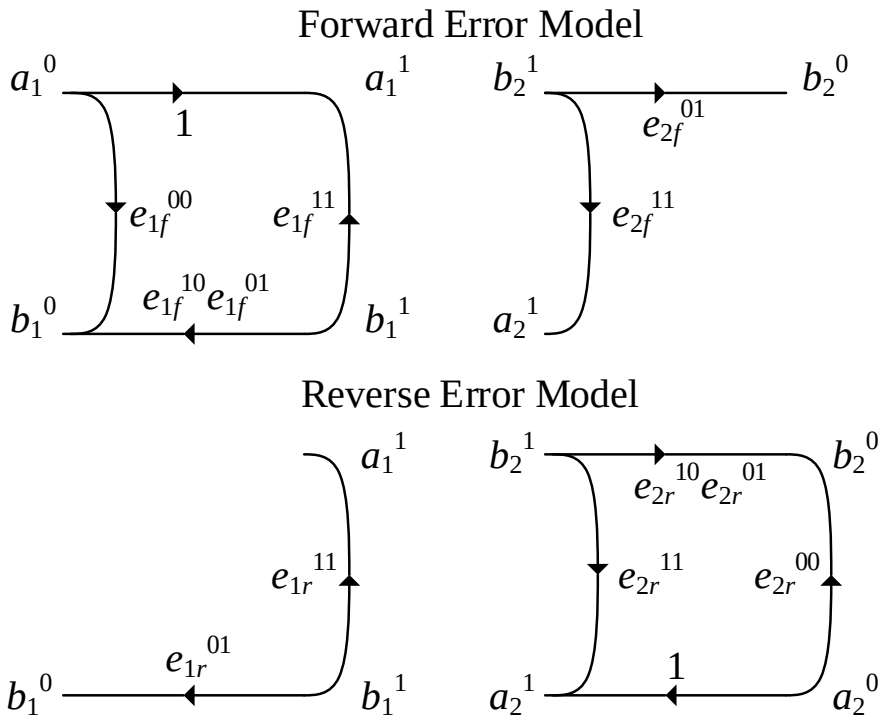

Figure 3.5: Linear ten-term error model. Because a VNA only makes ratioed measurements, one term of both the forward error model and the reverse error model can be normalized to unity to decrease the number of error terms to five for each direction.

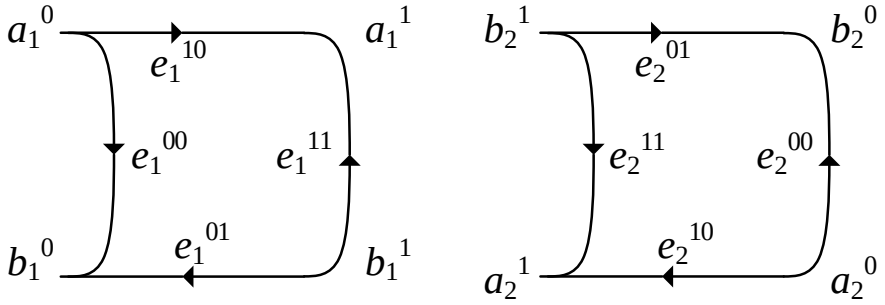

Figure 3.6: Nonlinear eight-term error model. Note that no terms are normalized or combined. Stimuli are often applied in both the forward and reverse directions at the same time.

3.2 Harmonic Balance Simulation

The current preferred method for the generation of X-parameters and the simulation of circuits that include X-parameter models is Harmonic Balance (HB). For a detailed analysis, see [22], [23], or [24]. We will provide a summary of its basic operation, drawing from all of these works.

The standard method for circuit analysis, including nonlinear, transient analysis, has been the Simulation Program with Integrated Circuit Emphasis (SPICE) [25]. SPICE is a general-purpose circuit simulator which has stood as the golden standard for circuit simulation for much of its over forty years of existence. It is based on modified nodal analysis (MNA) and performs nonlinear analysis by iterating through the Newton-Raphson algorithm.

The challenge of using SPICE or any other time-domain simulator is that the simulation must run long enough to reach the steady-state solution, which, for a circuit with slow transient properties, might take hundreds of thousands of periods. Fourier analysis must then be done to the output steady-state waveforms in order to recover the spectral content of these waveforms [22].

HB provides an attractive alternative to time-domain simulation for finding the steady-state solution of the circuit, which can be described by a nonlinear differential equation of the form [23]

$$g\left(v(t)\right) + \frac{d}{dt} q\left(v(t)\right) + y(t) \otimes v(t) = i(t) \tag{3.1}$$

where $g(\cdot)$ and $q(\cdot)$ are nonlinear functions, $y(\cdot)$ is an impulse response, $\otimes$ is the convolution operator, and $i(t)$ is the excitation current.

While HB still uses MNA to construct its equations, it assumes that the inputs to the circuit are a discrete number of steady-state sinusoids. This means that all of the node voltages $v(t)$ in the system can be written as the sum of steady-state sinusoids. For a circuit with n input sources, $v(t)$ is approximated as an n-dimensional Fourier series

$$v(t) = \mathrm{Re}\left[\sum_{k_1=0}^{K_1}\sum_{k_2=0}^{K_2}\cdots\sum_{k_n=0}^{K_n} V_{k_1,k_2,\ldots,k_n} e^{j2\pi(k_1 f_1+\ldots+k_n f_n)t}\right] \tag{3.2}$$

where $f_1, \ldots, f_n$ are the fundamental frequency of the n sources and $K_1, \ldots, K_n$ are the maximum number of harmonics for each source tone. This setup

allows for mixing products and harmonics of the input frequencies to be produced in the outputs of the sources. The Fourier coefficients $V_{k_1,k_2,\ldots,k_n}$ for each node voltage and frequency combination are now the unknowns in the circuit which compose the approximate solution.

We can then use Fourier analysis to expand the n nonlinear differential equations into $m \cdot n$ nonlinear algebraic equations, where m is the total number of frequencies, the sum of the input frequencies, their harmonics, and their mixing terms. This transforms (3.1) into

$$F_k \{g(v(t))\} + j\omega_k F_k \{q(v(t))\} + \hat{Y}(\omega_k)V_k = \hat{I}(\omega_k) \tag{3.3}$$

for every $k = 1, \ldots, n$. F_k is the kth spectral component of the Fourier transform of (3.1) and $\omega_k = 2\pi f k$. $\hat{Y}(\omega_k)$ and $\hat{I}(\omega_k)$ are the Fourier transforms of $y(t)$ and $i(t)$, respectively. This formulation can result in a very large number of unknowns, especially as m grows large.

The circuit is then subdivided into linear and nonlinear subcircuits. X-parameter models are, of course, included in the nonlinear subcircuit. The HB solution is found iteratively, as shown in the flow chart in Fig. 3.7. First, the currents sourced by linear elements are calculated in the frequency domain from $\hat{Y}(\omega_k)$ and $\hat{I}(\omega_k)$. Then the nonlinear circuit voltages in the frequency domain are inverse Fourier-transformed and used to calculate the currents for the nonlinear portion of the circuit in the time domain. These currents are then Fourier-transformed back into the frequency domain when they are summed with the linear currents in the frequency domain. Since by Kirchkoff's current law (KCL) the currents at each node must sum to zero, the residual of this sum is error. This error is used to update the circuit voltages, usually by some form of the Newton-Raphson method, and the process is iterated until the error is less than a tolerance, μ, that can be set by the user. Sometimes the user must increase the number of harmonics used to approximate the solution in order to find an error less than μ.

3.3 Circuit Envelope Simulation

Circuit envelope simulation is another option for simulation with X-parameter models. Circuit envelope simulation is a hybrid time and frequency simula-

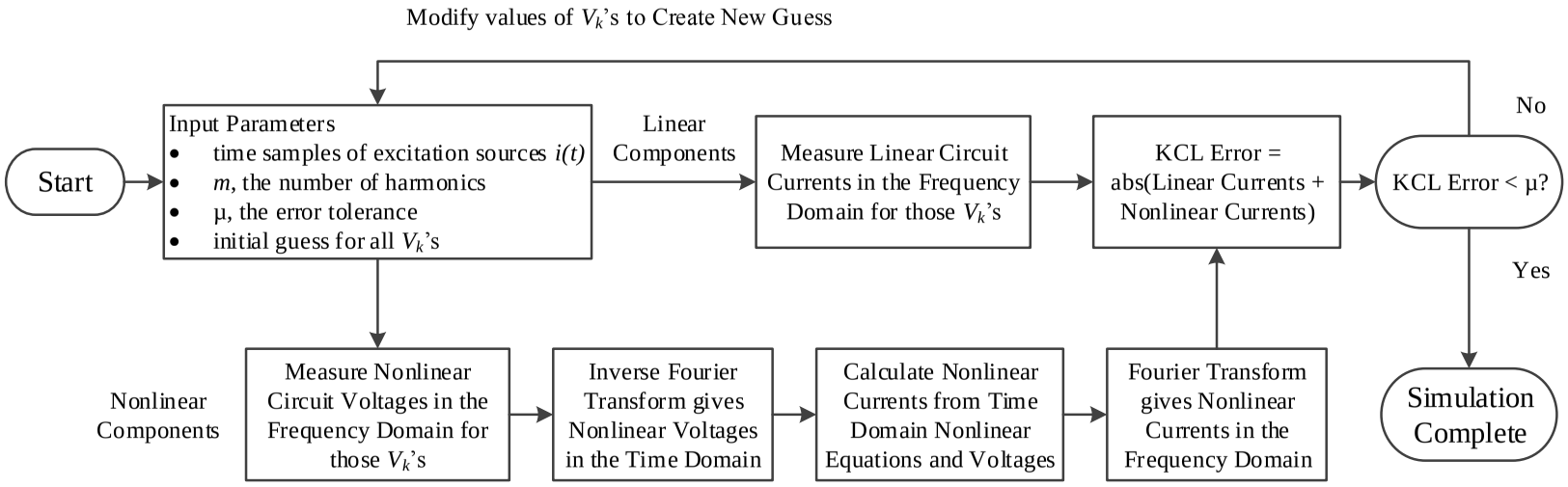

Figure 3.7: Flow chart describing the harmonic balance simulation flow. The linear and nonlinear portions of the circuit are solved separately and then equated together. This process is iterated until the error between the two portions is below the error tolerance, μ [23].

tion technique [26]. The premise is that the any signal $v(t)$ in the simulation can be represented as

$$v(t) = E(t)\mathrm{Re}\left[\sum_{k_1=0}^{K_1}\sum_{k_2=0}^{K_2}\cdots\sum_{k_n=0}^{K_n} V_{k_1,k_2,\ldots,k_n} e^{j2\pi(k_1 f_1+\ldots+k_n f_n)t}\right] \tag{3.4}$$

where $E(t)$ is a time-varying envelope function that modulates the rest of the expression, hereafter referred to as the carrier [27]. The envelope function $E(t)$ varies much more slowly than the carrier. Essentially, this allows for the Fourier coefficients that HB typically solves for to be time-varying. Circuit envelope simulation is simply several HB simulations performed at user-defined time samples of $E(t)$. The input signals for each HB simulation are supplied by the amplitudes and phases of the envelope functions. HB simulation is performed at each time sample and the results from these individual HB simulations are then stitched together to form the circuit envelope outputs, which can be viewed in either the time domain or the frequency domain.

The time-domain data extracted from circuit envelope simulations can be used to model phenomena such as oscillator start up, response to a pulsed RF response, phase-locked loop lock time, and constellation plots. The frequency-domain data can be used to measure intermodulation distortion and other forms of spectral regrowth [27].

3.4 Cascading X-Parameter Blocks

One of the most useful benefits of S-parameters is that two or more two-port S-parameter models, $[S]^{(1)}$ and $[S]^{(2)}$ defined as

$$\begin{bmatrix} {B_1}^{(1)} \\ {B_2}^{(1)} \end{bmatrix} = \begin{bmatrix} {S_{11}}^{(1)} & {S_{12}}^{(1)} \\ {S_{21}}^{(1)} & {S_{22}}^{(1)} \end{bmatrix} \begin{bmatrix} {A_1}^{(1)} \\ {A_2}^{(1)} \end{bmatrix} \tag{3.5}$$

and

$$\begin{bmatrix} {B_1}^{(2)} \\ {B_2}^{(2)} \end{bmatrix} = \begin{bmatrix} {S_{11}}^{(2)} & {S_{12}}^{(2)} \\ {S_{21}}^{(2)} & {S_{22}}^{(2)} \end{bmatrix} \begin{bmatrix} {A_1}^{(2)} \\ {A_2}^{(2)} \end{bmatrix} \tag{3.6}$$

can be cascaded together as if they were one model $[S]^{(T)}$, defined as

$$\begin{bmatrix} {B_1}^{(2)} \\ {B_2}^{(2)} \end{bmatrix} = \begin{bmatrix} {S_{11}}^{(T)} & {S_{12}}^{(T)} \\ {S_{21}}^{(T)} & {S_{22}}^{(T)} \end{bmatrix} \begin{bmatrix} {A_1}^{(1)} \\ {A_2}^{(1)} \end{bmatrix} \tag{3.7}$$

as demonstrated in Fig. 3.8.

The cascade analysis begins by using Kirchhoff's voltage law (KVL) and Kirchhoff's current law (KCL) at the internal node between the two blocks to equate the incident and scattered waves

$$A_2^{(1)} = B_1^{(2)}, \tag{3.8}$$

$$A_1^{(2)} = B_2^{(1)}. \tag{3.9}$$

We then convert each S-parameter model into a T-parameter model,[1] also known as a chain scattering parameter model or a scattering transfer parameter model. The T-parameters have the form

$$\begin{bmatrix} A_1 \\ B_1 \end{bmatrix} = \begin{bmatrix} T_{11} & T_{12} \\ T_{21} & T_{22} \end{bmatrix} \begin{bmatrix} B_2 \\ A_2 \end{bmatrix}. \tag{3.10}$$

The relationship between the S- and T- parameters is [28]

$$\begin{bmatrix} T_{11} & T_{12} \\ T_{21} & T_{22} \end{bmatrix} = \begin{bmatrix} \frac{1}{S_{21}} & -\frac{S_{22}}{S_{21}} \\ \frac{S_{11}}{S_{21}} & S_{12} - \frac{S_{11}S_{22}}{S_{21}} \end{bmatrix} \tag{3.11}$$

and

$$\begin{bmatrix} S_{11} & S_{12} \\ S_{21} & S_{22} \end{bmatrix} = \begin{bmatrix} \frac{T_{21}}{T_{11}} & T_{22} - \frac{T_{21}T_{12}}{T_{11}} \\ \frac{1}{T_{11}} & -\frac{T_{12}}{T_{11}} \end{bmatrix}. \tag{3.12}$$

The benefit of the conversion to T-parameters is that for two T-parameter blocks, $[T]^{(1)}$ and $[T]^{(2)}$,

$$\begin{bmatrix} {A_1}^{(1)} \\ {B_1}^{(1)} \end{bmatrix} = \begin{bmatrix} {T_{11}}^{(1)} & {T_{12}}^{(1)} \\ {T_{21}}^{(1)} & {T_{22}}^{(1)} \end{bmatrix} \begin{bmatrix} {B_2}^{(1)} \\ {A_2}^{(1)} \end{bmatrix} \tag{3.13}$$

and

$$\begin{bmatrix} {A_1}^{(2)} \\ {B_1}^{(2)} \end{bmatrix} = \begin{bmatrix} {T_{11}}^{(2)} & {T_{12}}^{(2)} \\ {T_{21}}^{(2)} & {T_{22}}^{(2)} \end{bmatrix} \begin{bmatrix} {B_2}^{(2)} \\ {A_2}^{(2)} \end{bmatrix} \tag{3.14}$$

[1] These are not to be confused with X-parameters of types S and T.

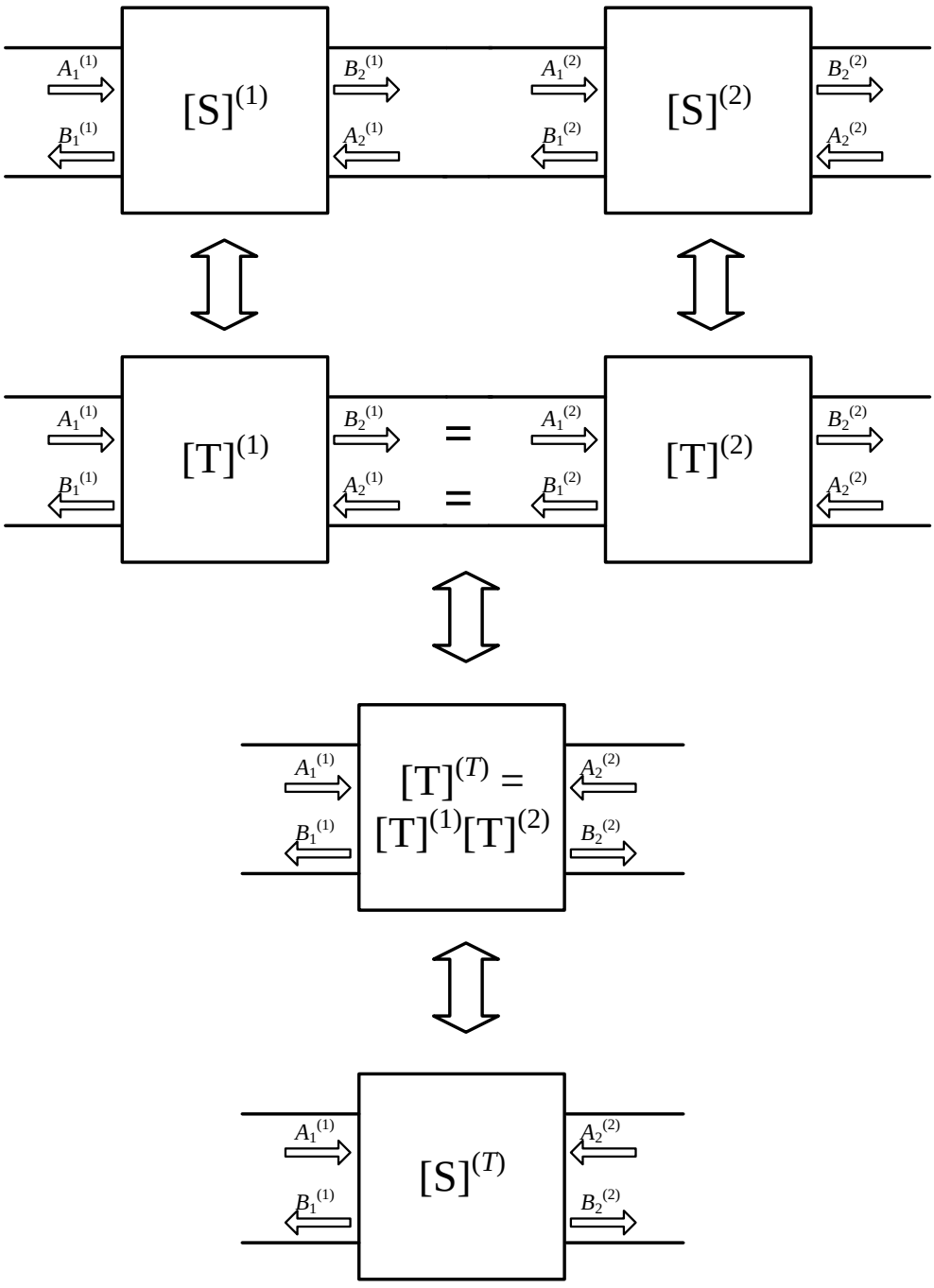

Figure 3.8: Cascade of two S-parameter blocks, $[S]^{(1)}$ and $[S]^{(2)}$ to form one combined S-parameter block $[S]^{(T)}$. The S-parameter blocks are first converted into equivalent T-parameter blocks, $[T]^{(1)}$ and $[T]^{(2)}$. These T-parameter blocks can then be combined to form $[T]^{(T)}$, which is then converted back to an S-parameter block $[S]^{(T)}$.

and using (3.8) and (3.9), we find

$$\begin{bmatrix} {A_1}^{(1)} \\ {B_1}^{(1)} \end{bmatrix} = \begin{bmatrix} {T_{11}}^{(1)} & {T_{12}}^{(1)} \\ {T_{21}}^{(1)} & {T_{22}}^{(1)} \end{bmatrix} \begin{bmatrix} {A_1}^{(2)} \\ {B_1}^{(2)} \end{bmatrix} \tag{3.15}$$

$$\begin{bmatrix} {A_1}^{(1)} \\ {B_1}^{(1)} \end{bmatrix} = \begin{bmatrix} {T_{11}}^{(1)} & {T_{12}}^{(1)} \\ {T_{21}}^{(1)} & {T_{22}}^{(1)} \end{bmatrix} \begin{bmatrix} {T_{11}}^{(2)} & {T_{12}}^{(2)} \\ {T_{21}}^{(2)} & {T_{22}}^{(2)} \end{bmatrix} \begin{bmatrix} {B_2}^{(2)} \\ {A_2}^{(2)} \end{bmatrix} \tag{3.16}$$

$$\begin{bmatrix} {A_1}^{(1)} \\ {B_1}^{(1)} \end{bmatrix} = \begin{bmatrix} {T_{11}}^{(T)} & {T_{12}}^{(T)} \\ {T_{21}}^{(T)} & {T_{22}}^{(T)} \end{bmatrix} \begin{bmatrix} {B_2}^{(2)} \\ {A_2}^{(2)} \end{bmatrix} \tag{3.17}$$

where the combined T-parameter model $[T]^{(T)}$ is

$$[T]^{(T)} = [T]^{(1)}[T]^{(2)} \tag{3.18}$$

which can be converted back into S-parameters using (3.12) to give the combined S-parameter block, $[S]^{(T)}$ [28]. The combined S-parameter block requires no knowledge of the internal node between $[S]^{(1)}$ and $[S]^{(2)}$. It can be completely treated as though this node no longer exists. Being able to do this hinges on the linearity of both blocks, which allows each different frequency component of an incident wave to be evaluated separately.

For the cascade of two X-parameter blocks, $[X]^{(1)}$ and $[X]^{(2)}$, shown in Fig. 3.9, we use KVL and KCL to obtain the following relations at the internal node between the two blocks

$$B_{2,k}^{(1)} = A_{1,k}^{(2)}, \tag{3.19}$$

$$A_{2,k}^{(1)} = B_{1,k}^{(2)}. \tag{3.20}$$

When K harmonics are included in the simulation and the set of $2K$ equations defined by (3.19) and (3.20) are always enforced, we can treat the combined network as one network, $[X]^{(T)}$. If K is large enough, the complete solution can be determined without approximation. An HB simulator solves for cascaded nonlinear blocks in this way, albeit most HB simulators solve in terms of currents and voltages rather than incident and scattered waves. Hence, X-parameters, which are defined in terms of harmonic phasors $A_{q,l}$ and $B_{p,k}$, work natively in an HB simulation environment [12].

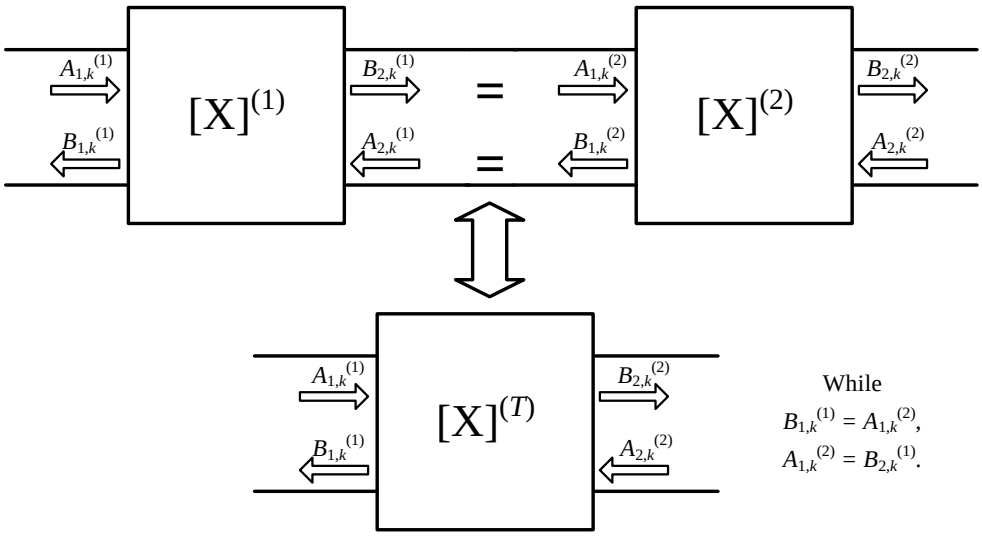

Figure 3.9: Cascade of two X-parameter blocks, $[X]^{(1)}$ and $[X]^{(2)}$ to form one combined X-parameter block $[X]^{(T)}$. Note that in the cascade of X-parameter blocks, (3.19) and (3.20) at the internal node must still be enforced.

3.5 Example X-Parameter Measurement of an Amplifier

As can be seen from Chapter 2, the X-parameter formalism is a powerful and mathematically robust tool for modeling nonlinear circuits. Since the X-parameter formalism most naturally applies to modeling devices that operate natively in the frequency domain, we will begin our instructional experiments with a power amplifier (PA). In this experiment, we use the Mini-Circuits Gali-1+ PA [29] on the Mini-Circuits TB-409-1+ amplifier evaluation board [30]. We measure the amplifier's X-parameters for three harmonics from 1 to 4 GHz at 1 GHz steps and from -20 to 5 dBm with 1 dB steps with an intermediate frequency bandwidth (IFBW) of 30 Hz. As with many other measurements, a smaller IFBW will result in a lower noise floor at the cost of longer measurement time. We choose a very small IFBW here because measurement time was not a concern. The amplifier is also biased with 12 V DC as recommended by [30] for normal operation.

We first observe the magnitude and phase of $X_{2,1}^{(FB)}/A_{1,1}$ versus input power in Fig. 3.10 at 1, 2, 3, and 4 GHz. Since the X-parameter of type FB measures the output response when all incident waves except the large signal $A_{1,1}$ are

zero, the available input power P_{In} in dBm in this case is defined as

$$P_{\text{In}} = 10 \cdot \log_{10}\left(|A_{1,1}|^2 \cdot 1000\right). \tag{3.21}$$

Assuming perfect matching at both the input port and the output port of the amplifier, the magnitude of $X_{2,1}^{(FB)}/A_{1,1}$ versus input power is identical to the AM/AM distortion curve typically measured for amplifiers. The phase of $X_{2,1}^{(FB)}/A_{1,1}$ versus input power is equal to the AM/PM distortion curves. These curves can be used to generate a memoryless input-output relationship for the amplifier [31]. There is a slight decrease in the magnitude of $X_{2,1}^{(FB)}/A_{1,1}$ as frequency increases. Frequency dependence of the AM/AM and AM/PM curves is indicative of memory effects in an amplifier, although the memory effect seen here is fairly minimal, particularly for 1 GHz frequency steps [32].

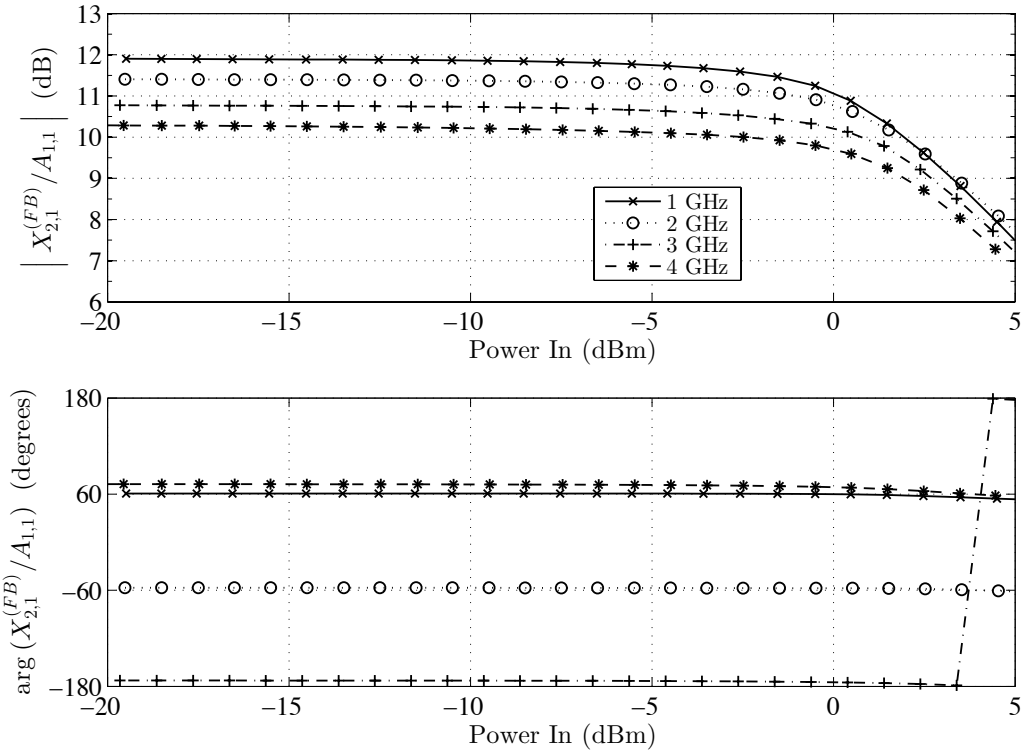

Figure 3.10: Plots of the magnitude and phase of $X_{2,1}^{(FB)}/A_{1,1}$ versus input power of the Mini-Circuits TB-409-1+ amplifier evaluation board at 1, 2, 3, and 4 GHz. At low input power levels, $X_{2,1}^{(FB)}/A_{1,1} \approx S_{21}$, the traditional S-parameter representing small-signal gain.

As is shown in Fig. 3.10, $X_{2,1}^{(FB)}/A_{1,1}$ is constant for low input power levels.

This makes sense because as input power becomes smaller, the amplifier is operating in the small-signal linear region. Hence, $X_{2,1}^{(FB)}/A_{1,1} \approx S_{21}$, the traditional S-parameter representing small-signal gain, at these low power levels. At higher power levels, we observe that $X_{2,1}^{(FB)}/A_{1,1}$ begins to saturate. From this plot, the 1-dB compression point can be easily observed for each frequency.

Figures 3.11 and 3.12 plot the magnitudes and phases of $X_{2,2}^{(FB)}/A_{1,1}$ and $X_{2,3}^{(FB)}/A_{1,1}$ versus input power. These parameters can be used to determine the levels of harmonic distortion from the second and third harmonics versus input power. As expected, both of these parameters approach zero in the small-signal input limit, with the third harmonic decaying faster than the second harmonic. Second harmonic distortion appears to be a fairly strong function of frequency.

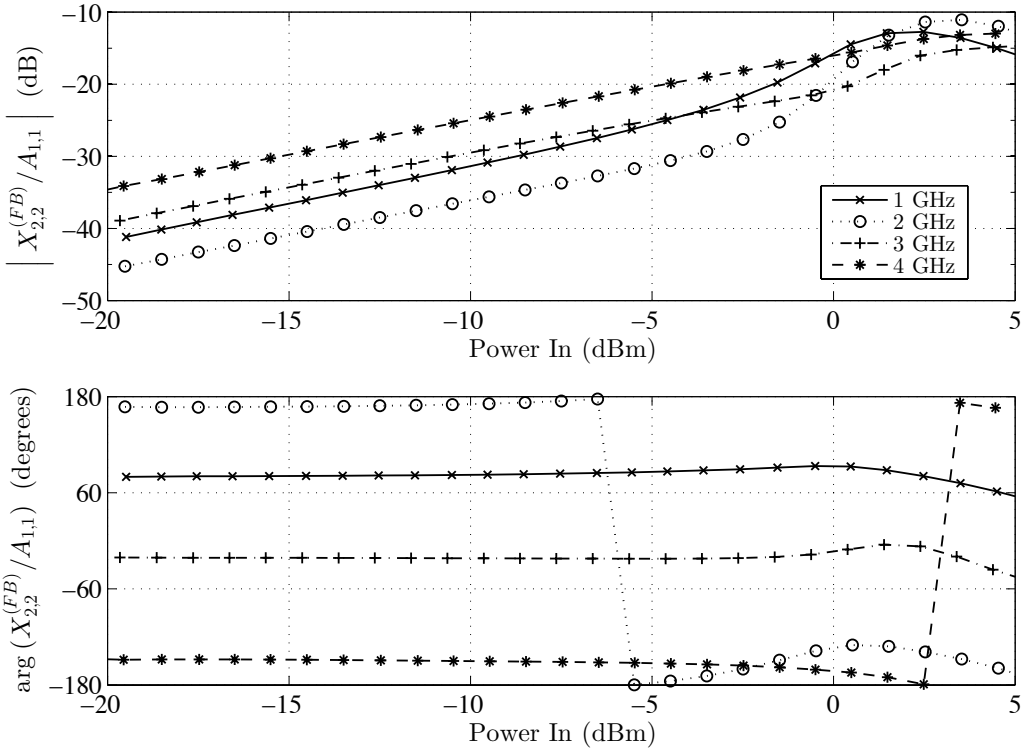

Figure 3.11: Plots of the magnitude and phase of $X_{2,2}^{(FB)}/A_{1,1}$ versus input power of the Mini-Circuits TB-409-1+ amplifier evaluation board at 1, 2, 3, and 4 GHz. The parameter $X_{2,2}^{(FB)}/A_{1,1}$ approaches zero as input power decreases.

Next, we observe the magnitude and phase of $X_{1,1}^{(FB)}/A_{1,1}$ in Fig. 3.13. This is the large-signal input match. In the small-signal limit, $X_{1,1}^{(FB)}/A_{1,1} \approx S_{11}$,

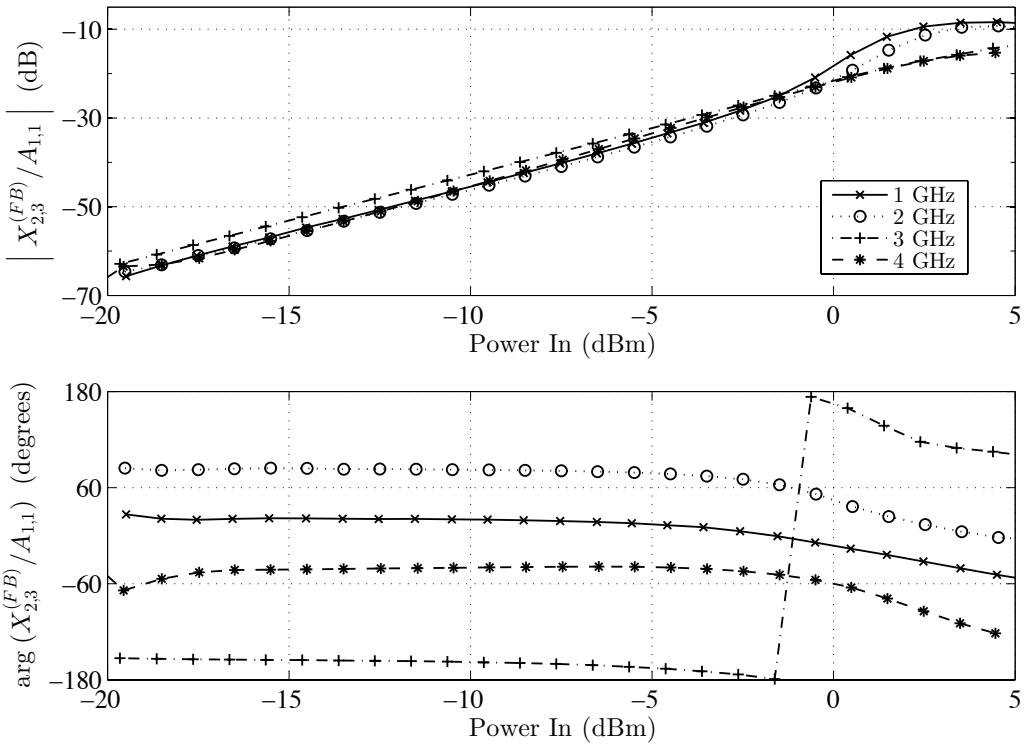

Figure 3.12: Plots of the magnitude and phase of $X_{2,3}^{(FB)}/A_{1,1}$ versus input power of the Mini-Circuits TB-409-1+ amplifier evaluation board at 1, 2, 3, and 4 GHz. The parameter $X_{2,3}^{(FB)}/A_{1,1}$ approaches zero as input power decreases.

the traditional S-parameter representing small-signal input match. As the input power increases, the amplifier enters saturation and more power is reflected.

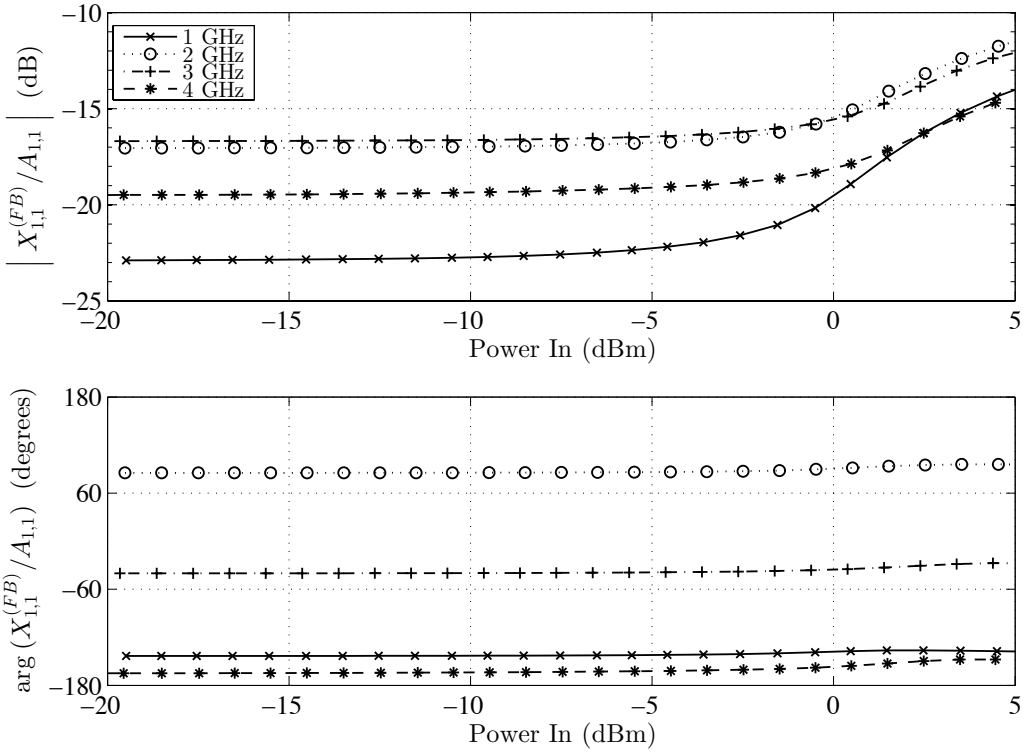

Figure 3.13: Plots of the magnitude and phase of $X_{1,1}^{(FB)}/A_{1,1}$ versus input power of the Mini-Circuits TB-409-1+ amplifier evaluation board at 1, 2, 3, and 4 GHz. This is the large-signal input match. In the small-signal limit, $X_{1,1}^{(FB)}/A_{1,1} \approx S_{11}$, the traditional S-parameter representing small-signal input match.

We now move on to our analysis of the small-signal parameters at the output, port 2. These X-parameters give us a sense of the amplifier match at the output for different harmonics. We see that for high input powers, the X-parameters of type T become significant. At low powers, all of these parameters approach zero. Figures 3.14 and 3.15 show $X_{2,1;2,1}^{(S)}$ and $X_{2,1;2,1}^{(T)}$ versus input power. In the small-signal limit, $X_{2,1;2,1}^{(S)} \approx S_{22}$, the traditional S-parameter representing small-signal output match. This is seen in the figure for all frequencies except 4 GHz. It is likely that $X_{2,1;2,1}^{(S)}$ at 4 GHz will become constant at input powers lower than -20 dBm. This is a reasonable assumption because the PA being measured is designed to operate from DC to 8 GHz. It is likely that it has its best return loss in the middle of its

bandwidth. This assumption can be easily tested by measuring the $X^{(S)}_{2,1;2,1}$ of the PA for input powers lower than -20 dBm. In doing so, care must be taken to ensure that this measurement is above the noise floor of the measurement system.

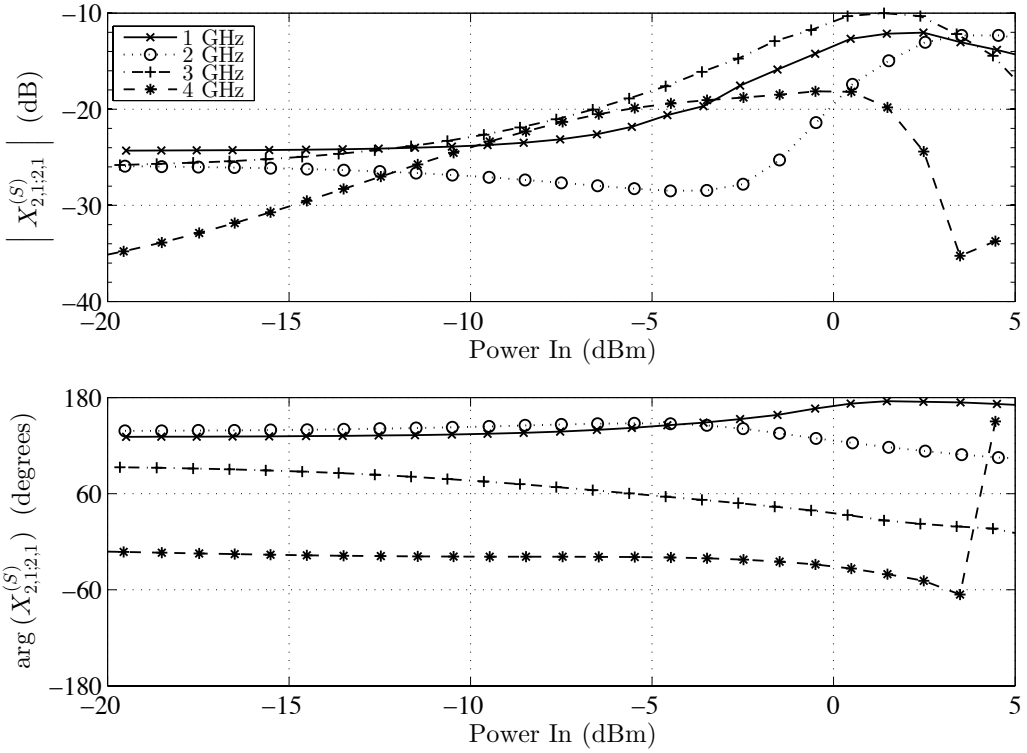

Figure 3.14: Plots of the magnitude and phase of $X^{(S)}_{2,1;2,1}$ versus input power of the Mini-Circuits TB-409-1+ amplifier evaluation board at 1, 2, 3, and 4 GHz. In the small-signal limit, $X^{(S)}_{2,1;2,1} \approx S_{22}$, the traditional S-parameter representing small-signal output match.

Figures 3.16 and 3.17 show $X^{(S)}_{2,1;2,2}$ and $X^{(T)}_{2,1;2,2}$ versus input power. As shown from the plots of $X^{(FB)}_{2,2}/A_{1,1}$, the PA will output spectral energy at the second harmonic, particularly when it being driven hard. Parameters $X^{(S)}_{2,1;2,2}$ and $X^{(T)}_{2,1;2,2}$ provide intuition into how sensitive the circuit is to the reflection of the second harmonic from the load. Both of these parameters approach zero as input power decreases.

Figures 3.18 and 3.19 show $X^{(S)}_{2,1;2,3}$ and $X^{(T)}_{2,1;2,3}$ versus input power. As shown from the plots of $X^{(FB)}_{2,3}/A_{1,1}$, the PA will also output spectral energy at the third harmonic, particularly when it being driven hard. Parameters $X^{(S)}_{2,1;2,3}$ and $X^{(T)}_{2,1;2,3}$ provide intuition into how sensitive the circuit is to the reflection of the third harmonic from the load. Both of these parameters

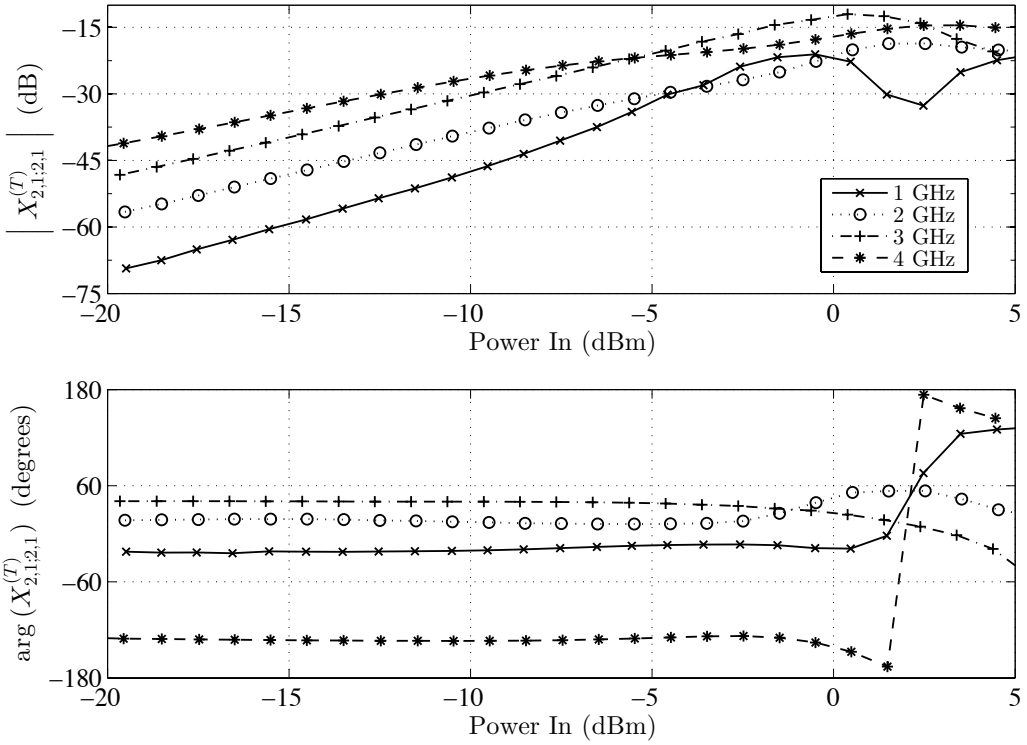

Figure 3.15: Plots of the magnitude and phase of $X^{(T)}_{2,1;2,1}$ versus input power of the Mini-Circuits TB-409-1+ amplifier evaluation board at 1, 2, 3, and 4 GHz. The parameter $X^{(T)}_{2,1;2,1}$ approaches zero as input power decreases.

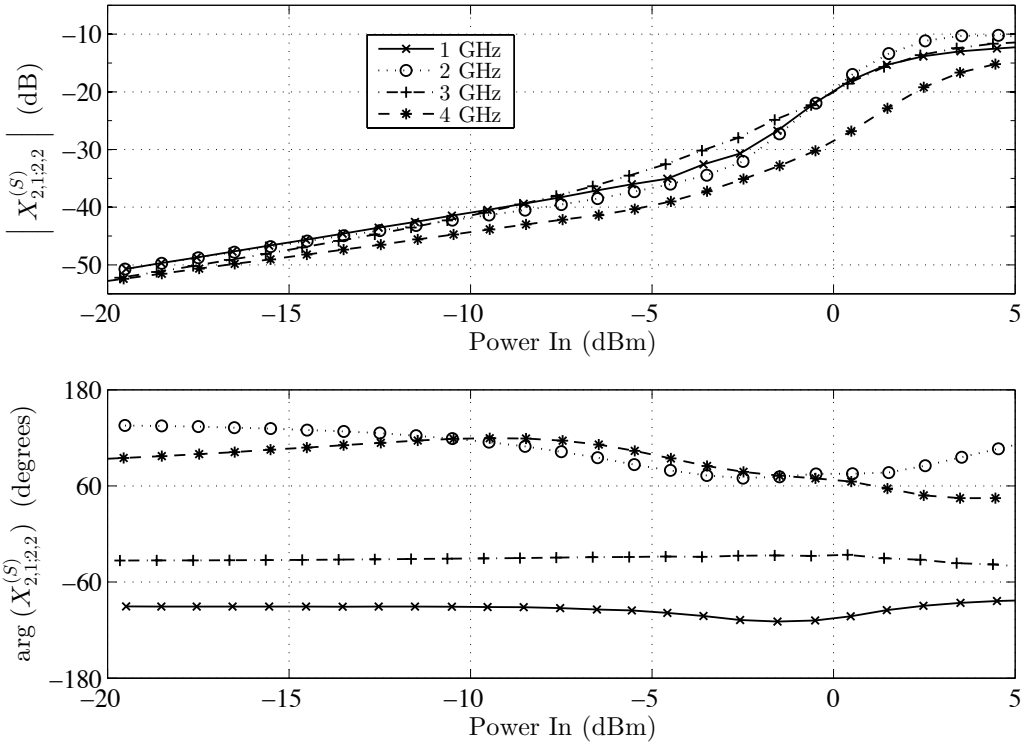

Figure 3.16: Plots of the magnitude and phase of $X^{(S)}_{2,1;2,2}$ versus input power of the Mini-Circuits TB-409-1+ amplifier evaluation board at 1, 2, 3, and 4 GHz.

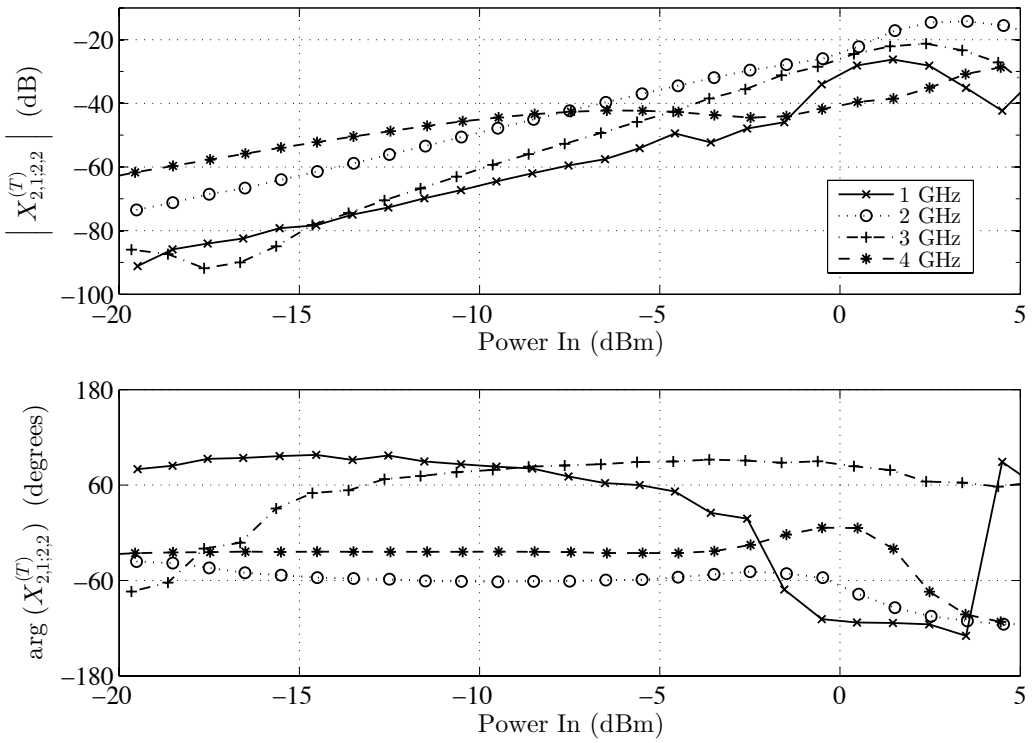

Figure 3.17: Plots of the magnitude and phase of $X^{(T)}_{2,1;2,2}$ versus input power of the Mini-Circuits TB-409-1+ amplifier evaluation board at 1, 2, 3, and 4 GHz.

approach zero as input power decreases.

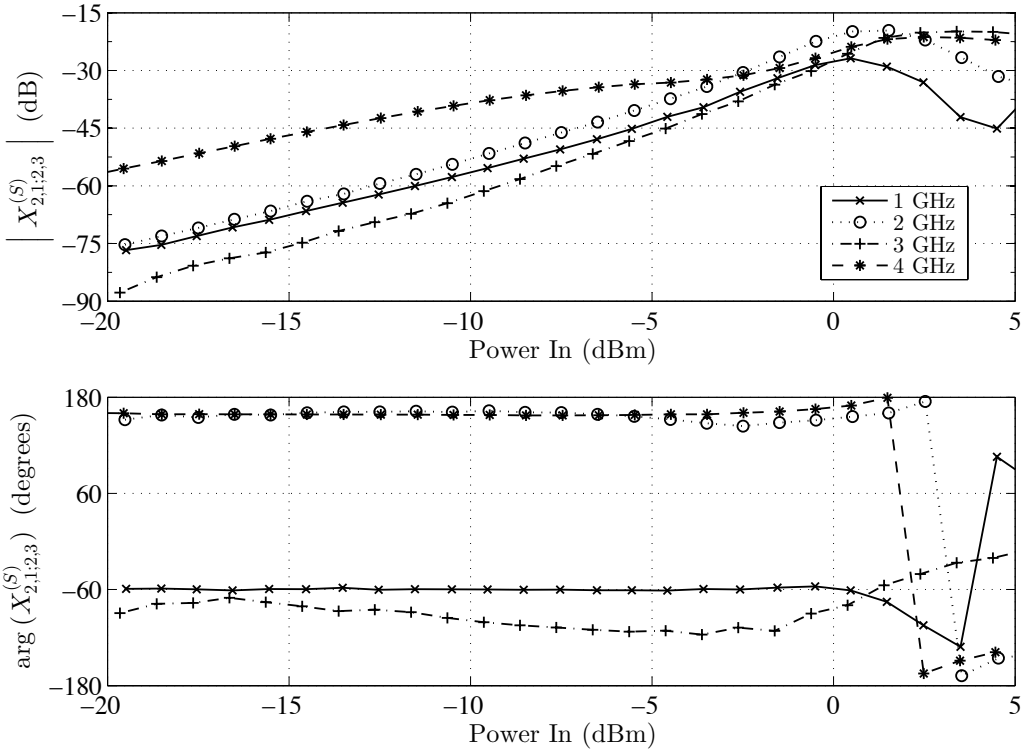

Figure 3.18: Plots of the magnitude and phase of $X^{(S)}_{2,1;2,3}$ versus input power of the Mini-Circuits TB-409-1+ amplifier evaluation board at 1, 2, 3, and 4 GHz.

Next, we use these measured X-parameters of the PA perform a circuit envelope simulation as pictured in Fig. 3.20. This simulation is meant to emulate an in-band intermodulation distortion measurement [15]. Here, the carrier is f_c and the envelope is made up of two tones centered at f_c with a separation of f_{offset} between the tones. This stimulus will produce in-band intermodulations at $f_c \pm n \cdot \frac{f_{\text{offset}}}{2}$ for all integer values of n. The magnitude of these in-band intermodulations will increase with the power of the input tones. This simulation, when parameterized for a wide range of input powers, can be used to measure the power of in-band intermodulations as a function of input power. The tones at $f_c \pm n \cdot \frac{f_{\text{offset}}}{2}$ are said to be in-band intermodulation tones of $(2n-1)$th order, termed IMDn. For example, the tones at $f_c \pm 5 \cdot \frac{f_{\text{offset}}}{2}$ are the IMD9 or ninth-order in-band intermodulation tones.

Figures 3.21–3.24 contain plots of the fundamental power as well as IMD3, IMD5, IMD7, and IMD9 for $f_c = 1$, 2, 3, and 4 GHz, respectively, $f_{\text{offset}} = 10$

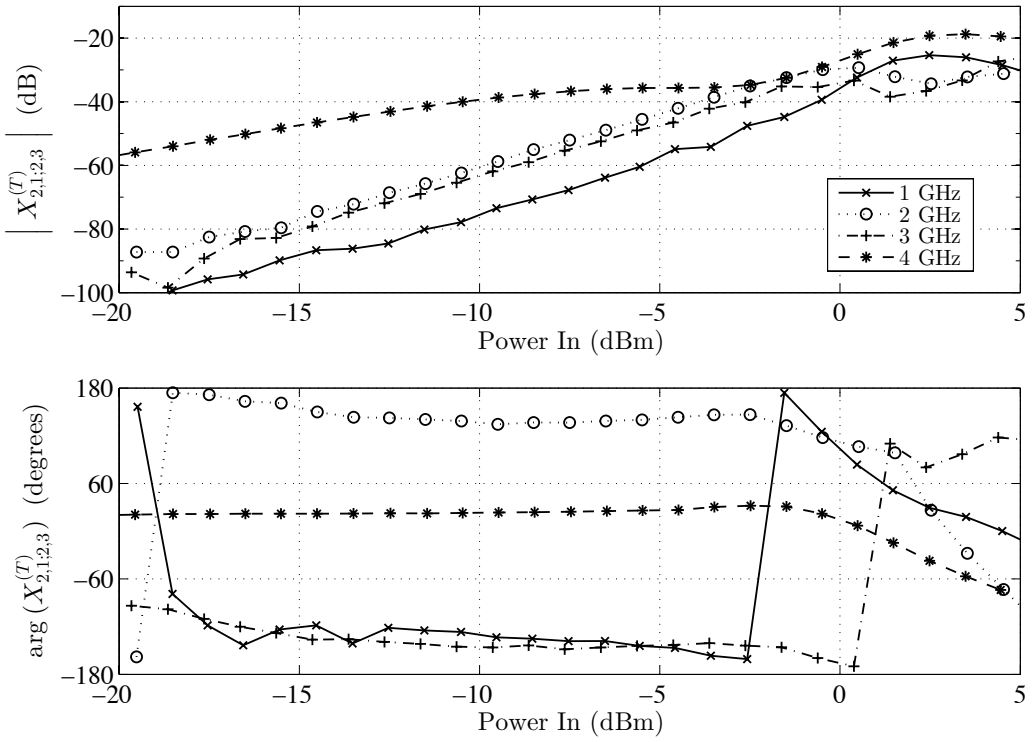

Figure 3.19: Plots of the magnitude and phase of $X^{(T)}_{2,1;2,3}$ versus input power of the Mini-Circuits TB-409-1+ amplifier evaluation board at 1, 2, 3, and 4 GHz.

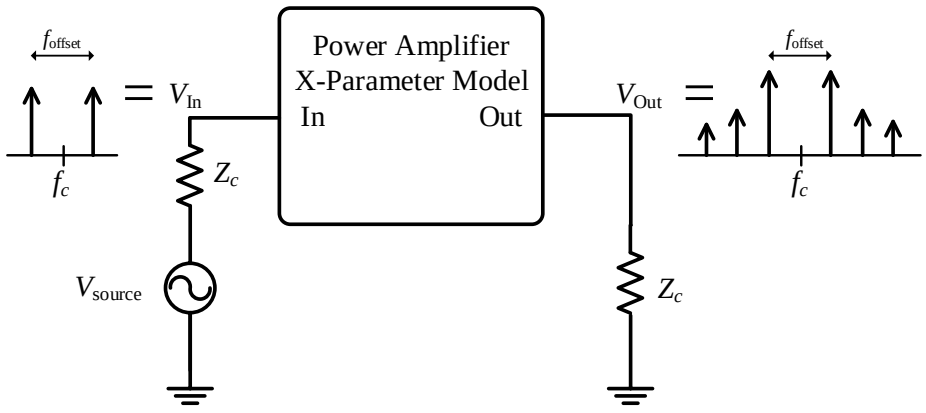

Figure 3.20: Block diagram for CE simulation. The envelope is made up of two tones centered at f_c with a separation of f_{offset} between the tones. This stimulus will produce in-band intermodulations at $f_c \pm n \cdot \frac{f_{\text{offset}}}{2}$ for all integer values of n. The magnitude of these in-band intermodulations will increase with the power of the input tones.

kHz. The envelope was simulated for two milliseconds with ten microsecond time steps. From these powers, the third-order, fifth-order, seventh-order, and ninth-order intercepts can be determined. For example, the third-order intercept (TOI) is found by

$$\mathrm{TOI} = P_{\mathrm{Fund}} + \frac{P_{\mathrm{Fund}} - \mathrm{IP3}}{2} \tag{3.22}$$

where the units of P_{Fund} and IP3 are dBm. At 2 GHz, the maximum of TOI versus input power is 24.931 dBm. This is 2.069 dB lower than the 27 dBm value listed on the Mini-Circuits Gali-1+ PA datasheet for the PA without the evaluation board, which confirms that we are able to generate a reasonable approximation of the TOI with a CE simulation from a single large-tone X-parameter measurement of this PA. None of the in-band intermodulation products appear to have a strong dependent on frequency.

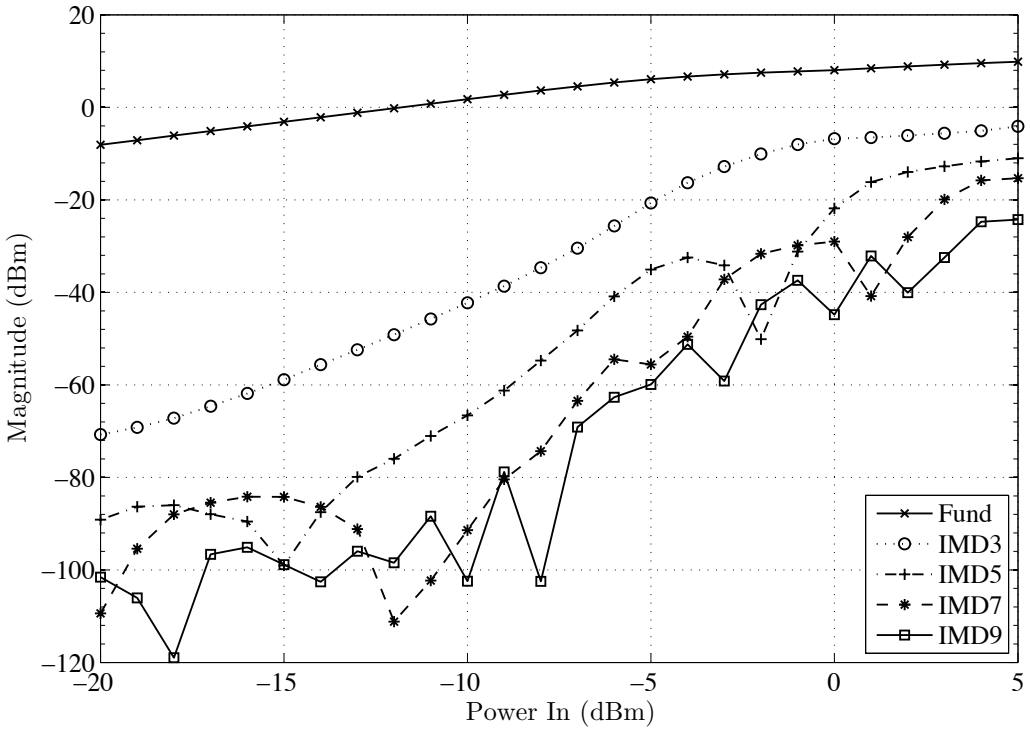

Figure 3.21: Plot of powers of the fundamental, IMD3, IMD5, IMD7, and IMD9 at 1 GHz for the Mini-Circuits TB-409-1+ amplifier evaluation board.

Overall, one single large-tone measurement allows us to recover a plethora of traditional nonlinear circuit figures of merit, including AM/AM distortion,

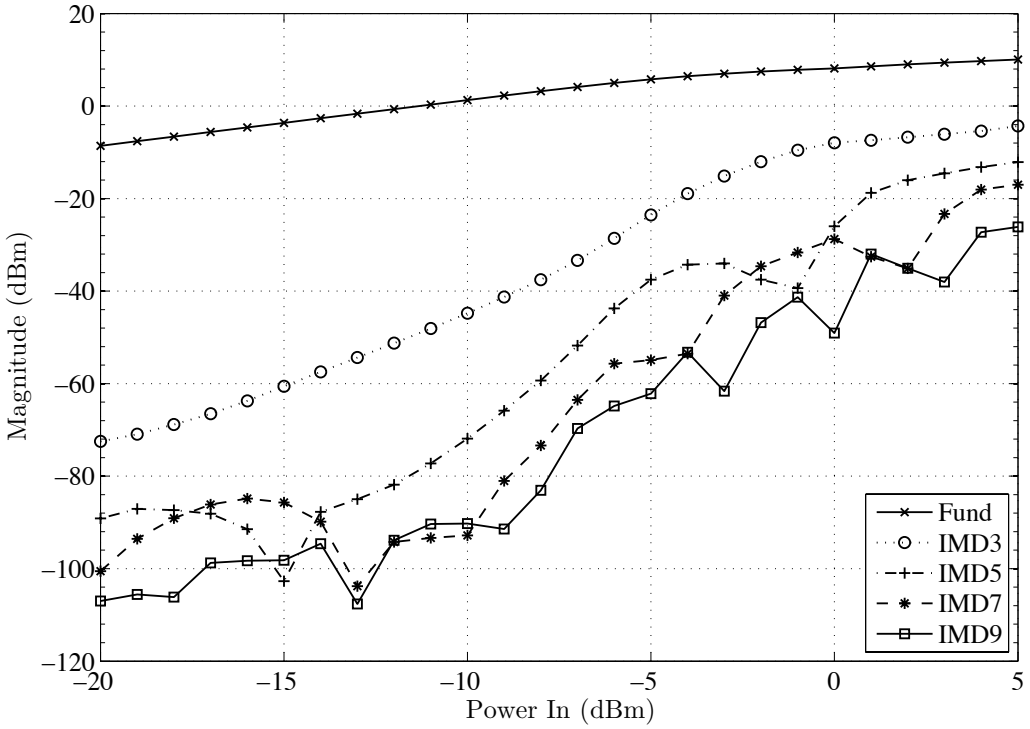

Figure 3.22: Plot of powers of the fundamental, IMD3, IMD5, IMD7, and IMD9 at 2 GHz for the Mini-Circuits TB-409-1+ amplifier evaluation board.

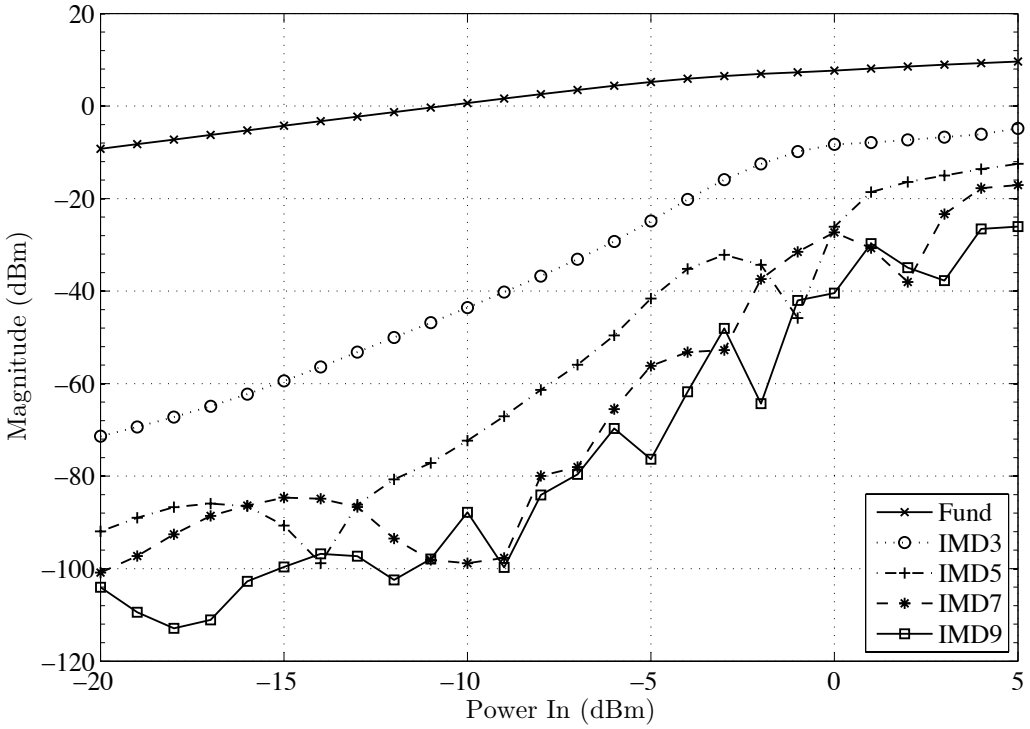

Figure 3.23: Plot of powers of the fundamental, IMD3, IMD5, IMD7, and IMD9 at 3 GHz for the Mini-Circuits TB-409-1+ amplifier evaluation board.

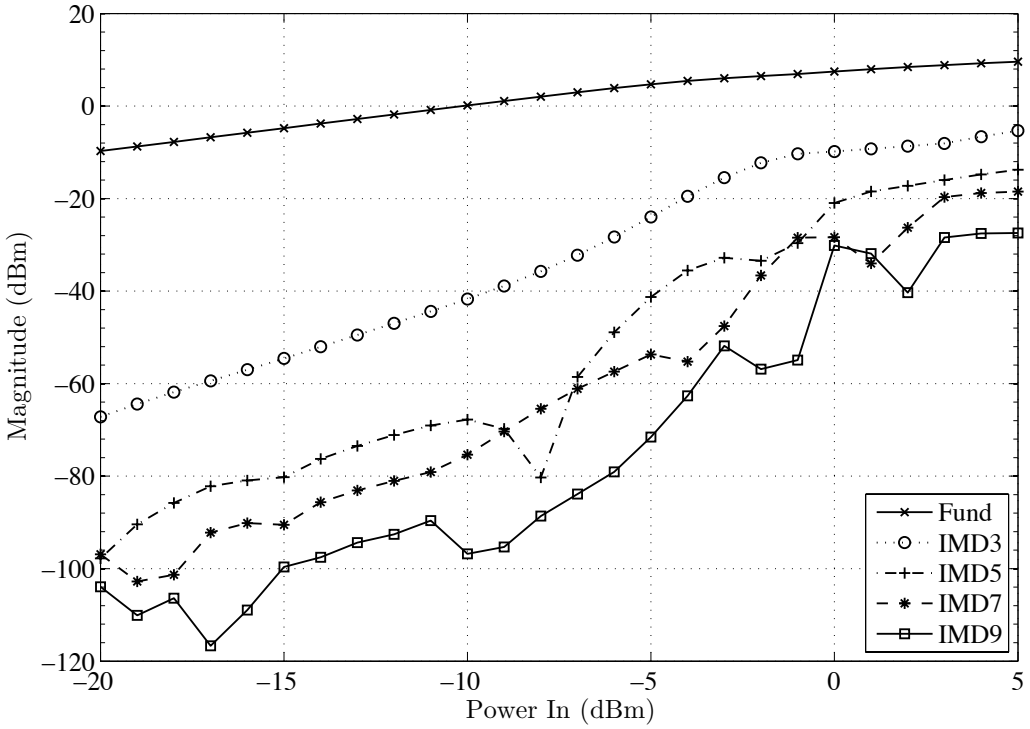

Figure 3.24: Plot of powers of the fundamental, IMD3, IMD5, IMD7, and IMD9 at 4 GHz for the Mini-Circuits TB-409-1+ amplifier evaluation board.

AM/PM distortion, 1-dB compression point, harmonic distortion, and IMDn. In addition to all of these, we are also able to use the X-parameter model as an electronic datasheet to be used in an HB or CE simulation to find the model's response to a myriad of stimuli.

3.6 Example X-Parameter Simulation of an I/O Buffer

Although much work on X-parameters has been published, there is very little sense of what X-parameters, particularly the large-signal parameters, actually look like, especially for an I/O buffer. Here we investigate properties of the simple nonlinear function of the large signal and its DC bias in the context of using X-parameters to model the behavior of a simple I/O buffer [33]. The example circuit analyzed here, shown in Fig. 3.25, is an equalized buffer consisting of a one-tap FIR filter implemented in a modified single-ended push-pull configuration using a typical 2.5 V CMOS process. The near-end signal driving the channel is obtained by voltage division, and the tap delay is implemented using a simple four-inverter chain. This circuit will also be analyzed without the equalization branch to provide additional intuition into the large-signal response of a buffer and its corresponding X-parameters.

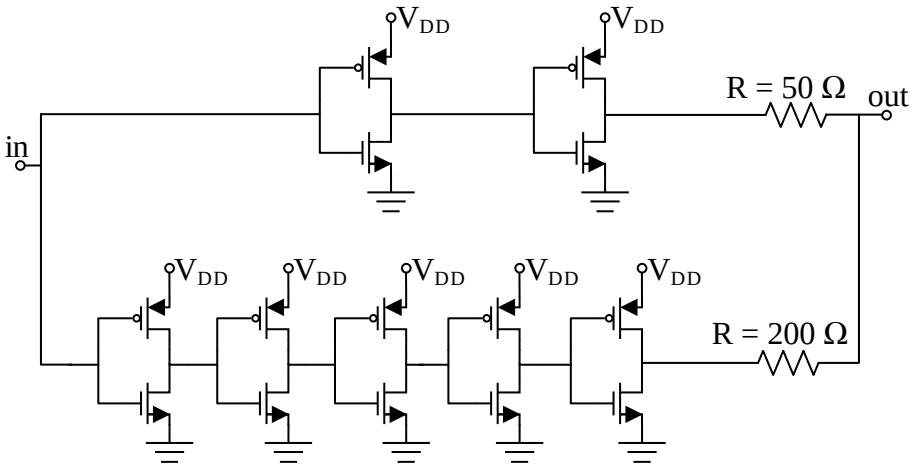

Figure 3.25: Transmitter with equalization branch using a 2.5 V CMOS process. This circuit is used with and without the equalization branch.

First, we demonstrate the effects of a DC voltage bias at the buffer input on the large-signal X-parameters. Then we study the degree of nonlinearity and frequency dependence on the large-signal response of an I/O buffer in the context of its normal operation. Next, we provide a comparison between a transient simulation of the transistor-level model of the example buffer and an HB simulation made with its X-parameter model with a large-signal stimulus to show that the X-parameter model captures the nonlinear behavior of the buffer.

The first nuance of using the X-parameter formalism for I/O buffers is the DC bias voltage on the input. Typical amplifiers might not need a DC bias at the input, but most I/O buffers are operated from rail-to-rail where the lower rail is the ground. As Fig. 3.26 shows, a bias voltage away from the middle of the rails produces data that is not useful because much of the input signal is outside of the rail-to-rail voltage range and is being clipped. Therefore, care must be taken to include this DC voltage while making X-parameter measurements of I/O buffers with an NVNA in the laboratory.

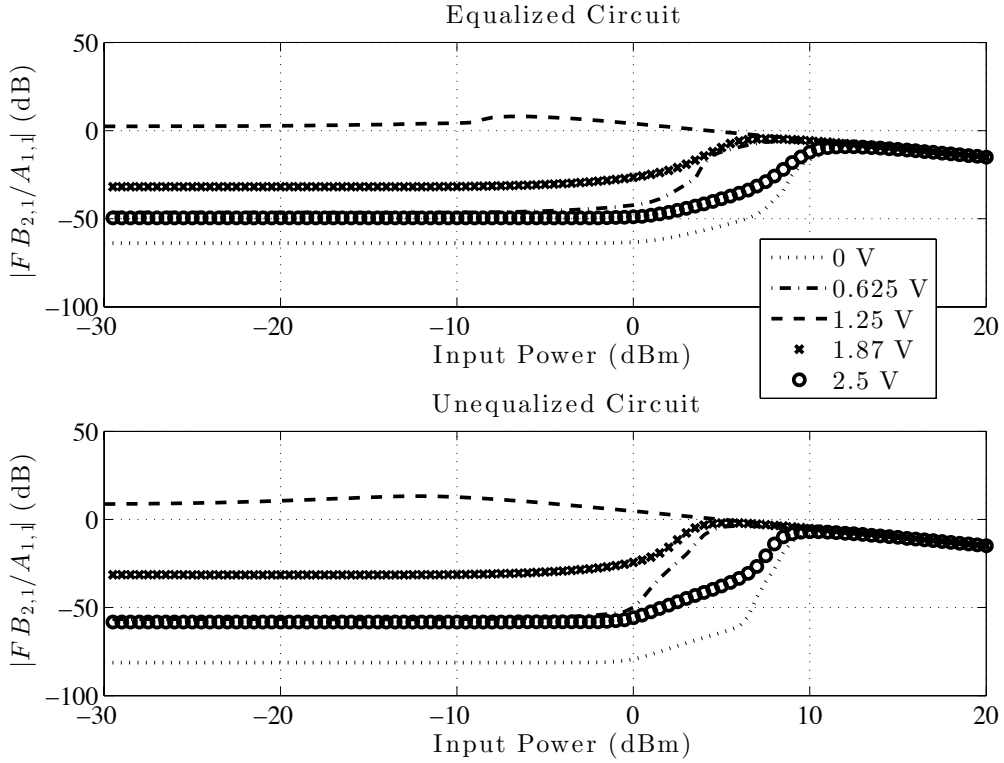

Figure 3.26: Magnitude of $FB_{2,1}/A_{1,1}$ for the test circuit with and without equalization for multiple values of input DC voltage.

As the magnitude of $A_{1,1}$ shrinks and approaches the linear operating region, the linear approximation of $X_{2,1}^{(FB)} = X_{2,1;1,1}^{(S)} \cdot A_{1,1}$, where $X_{2,1;1,1}^{(S)}$ is a constant, can be used. This approximation was leveraged in the transient simulation technique in [9]. In doing so, that work essentially assumed that all of the nonlinear behavior is modeled in the existence of harmonics and that all of the X-parameters are constant with respect to the magnitude of $A_{1,1}$. By then separating the real and imaginary portions of the incident and scattered waves for each harmonic, the relationship between the scattered and incident waves can be written as a linear transformation. Because the large-signal fundamental behavior is assumed to be linear, the S- and T-parameters that normally vary with respect to $|A_{1,1}|$ can instead be treated as constants. While this matrix representation is an incredibly desirable form, the linear approximation of the large-signal response is often not valid for the typical buffer that switches from rail to rail at its input. Figure 3.27 shows a plot of the simulated $X_{2,1}^{(FB)}$ term versus input power for the test circuit with and without equalization operating at 1, 2, and 3 GHz. The vertical line marks the input power equivalent to an input voltage with magnitude equal to the rail-to-rail voltage of the circuit. This line was determined from

$$\begin{aligned} V_1 &= V_{DC1} + 2\sqrt{Z_0}\,(A_1 + B_1) \\ &\approx V_{DC1} + 2\sqrt{Z_0}\left(|A_{1,1}| + \sum_{k=1}^{K}\left|X_{1,k}^{(FB)}\right|\right) \end{aligned} \tag{3.23}$$

where A_1 and B_1 are the total incident and scattered waves at the input port. These waves can be decomposed into K harmonic wave components and the scattered wave harmonic components are equal to the X-parameters of type FB assuming that there are no small-signal incident waves on either port. This is approximately true when the ports are well-matched, which was shown to be a reasonable assumption through comparison to a full HB simulation taking mismatch into account. In addition, a DC voltage bias, V_{DC1}, of one-half of the rail-to-rail voltage, in this case equal to 1.25 volts, was provided so as to minimize the clipping of the large-signal input $A_{1,1}$ as discussed above.

As can be seen, the typical operating input amplitude is well into the nonlinear region for both the unequalized and the equalized circuits. There is a short region of gain expansion before the device enters saturation, more

exaggerated for the equalized circuit. The large-signal term of the equalized circuit also exhibits stronger frequency-dependence than the unequalized circuit. This is appropriate because the equalization is a short-term memory effect.

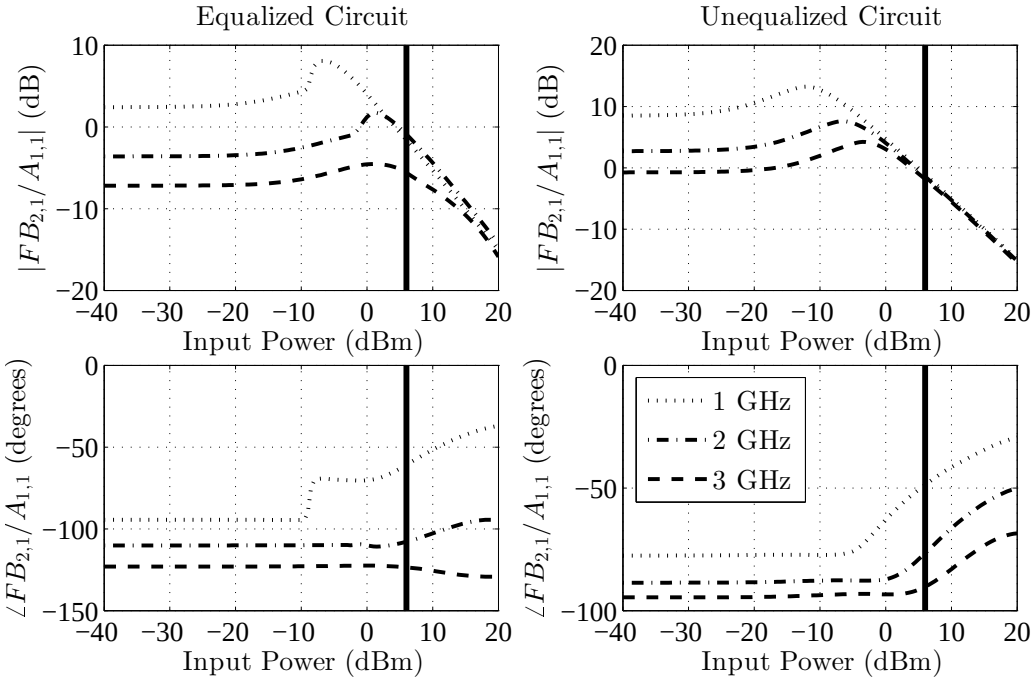

Figure 3.27: Magnitude and phase of gain = $X_{2,1}^{(FB)}/A_{1,1}$ for the test circuit with and without equalization at frequencies equal to 1, 2, and 3 GHz and a DC voltage bias of 1.25 V. The thick black line marks the input power level where the input voltage waveform amplitude is equal to 2.5 V, the rail-to-rail voltage.

While the AM/AM and AM/PM curves of a device can tell a great deal about a device's nonlinear distortion, especially in a well-matched environment, the large signal also produces a response at each harmonic k, characterized at port p by $X_{p,k}^{(FB)}$. The large-signal return losses at port 1, the input for each harmonic k, denoted by $X_{1,k}^{(FB)}$, are dominated by the fundamental, $X_{1,1}^{(FB)}$, which is at least 40 dB larger than that for every other harmonic at an input equal to the rail-to-rail voltage. Figure 3.28 shows the large-signal response at port 2, the output port, denoted by $X_{2,k}^{(FB)}$ for $k = 1$ to 5. As can be seen, $X_{2,3}^{(FB)}$ is less than 15 dB smaller than $X_{2,1}^{(FB)}$ for both the equalized and unequalized circuits. The second, fourth, and fifth harmonics are about 20 dB smaller than the fundamental. Thus, these harmonics have significant

contributions on the large-signal output and cannot be neglected.

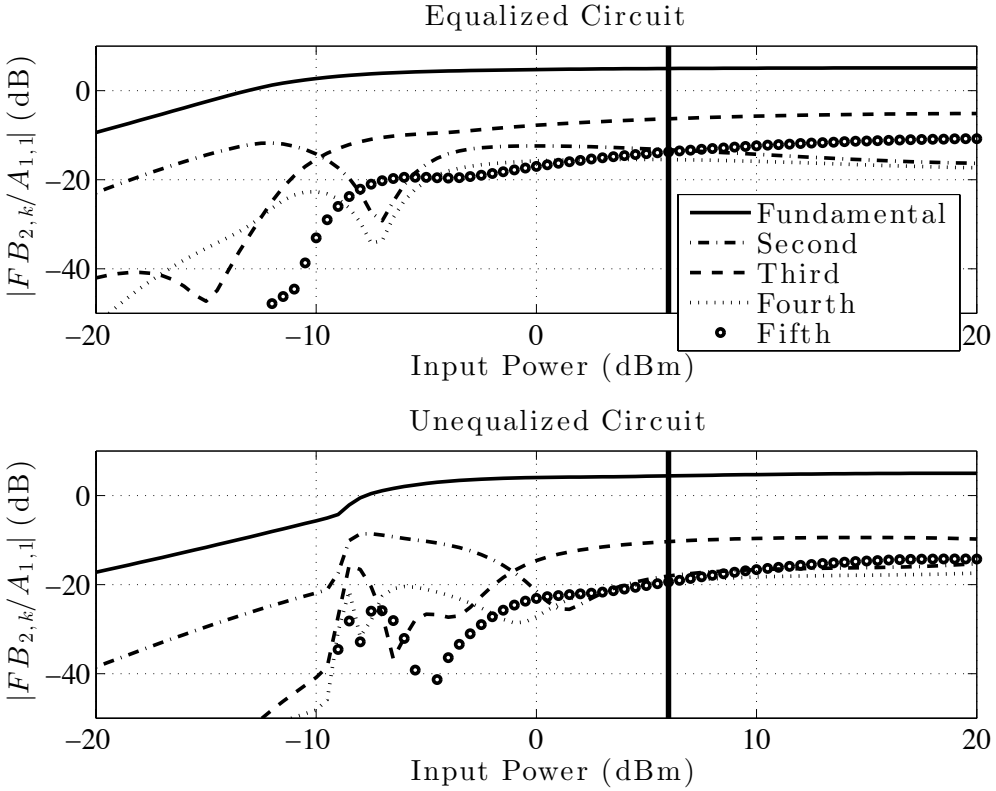

Figure 3.28: Magnitude of $X_{2,k}^{(FB)}/A_{1,1}$ for $k = 1$ to 5 for the test circuit with and without equalization at 1 GHz and a DC voltage bias of 1.25 V. The thick black line marks the input power level where the input voltage waveform amplitude is equal to 2.5 V, the rail-to-rail voltage.

Combining the fundamental and DC portions completes the large-signal stimulus, which spans the rail-to-rail voltage of the input. This is well into the saturation region of both the equalized and unequalized circuits, so harmonics will be produced at the output. Figure 3.29 shows a comparison between an HB simulation performed with ADS [34] using the X-parameter models of both circuits with only the large-signal stimulus using 11 harmonics to a transient simulation of the transistor-level model of the circuit, also performed in ADS. The nonlinear behavior is matched very well for both the equalized and unequalized circuits, save for some Gibbs phenomenon ripple in the unequalized case. The DC-to-DC response was calculated separately and added into the solution. Thus, there is potential for accurate modeling of the nonlinear behavior of a buffer with X-parameters.

In this section we have provided some intuition into the behavior of the

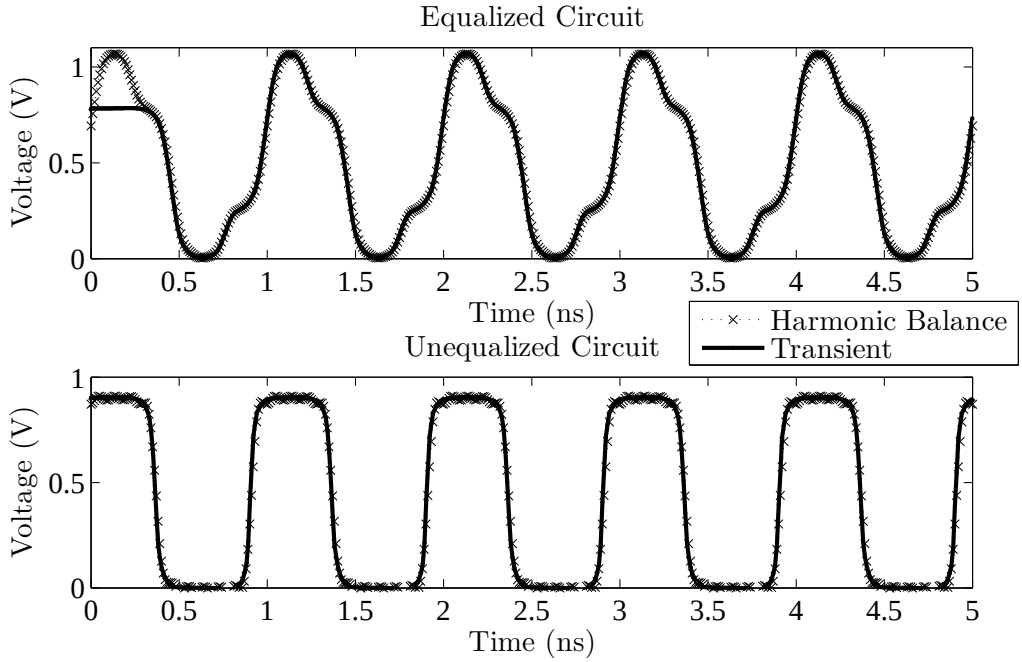

Figure 3.29: Comparison of HB simulation of X-parameter model of the equalized and unequalized circuits with $V_{DC1} = 1.25$ V and input fundamental spanning the rail-to-rail voltage versus transient simulation of the transistor-level model with similar excitation. The model is terminated on both ends with 50 Ω in addition to the excitation at the input. The plots match very closely except in the beginning where the transient simulation has not reached its operating state.

large-signal response of an I/O buffer in the context of the X-parameter formalism. The example buffer has both significant nonlinear distortion and harmonic generation at a power level equivalent to an input spanning the rail-to-rail voltage. Thus, it is appropriate to model the large-signal response as nonlinear. As has been shown, X-parameters can capture the nonlinear behavior seen in I/O buffers. They remain a very exciting platform for the modeling of I/O buffers because of this, their mathematical robustness, and their IP protection.

Future work into modeling I/O buffers with X-parameters should leverage the insights of nonlinear modeling found in the power amplifier community, but could possibly use the multitone X-parameter extension to emulate the wideband inputs to an I/O buffer [12]. Most of the signals that drive a buffer can be modeled with only a few large tones and harmonic superposition for the very high-frequency components. From these, an arbitrary bit stimulus with noise and jitter can be generated and used to construct an eye diagram for bit error rate estimation.

CHAPTER 4

SIGNAL INTEGRITY BACKGROUND

In this chapter, we provide background information on some signal integrity concepts. We begin by presenting the basic formulation for the Latency Insertion Method (LIM). We then extend this formulation to model CMOS devices. Next, we outline the Input/Output Buffer Information Specification (IBIS), the current standard for modeling input/output (I/O) circuits, and we describe the process for generating IBIS models. Finally, we describe the Algorithmic Modeling Interface (AMI) extension to IBIS as well as briefly addressing the kinds of components it is used to model.

4.1 Basic Latency Insertion Method Formulation

In this section, we present the basic formulation of the latency insertion method (LIM). LIM is a conditionally-stable circuit solver that has linear numerical complexity [11]. Through the use of Thévenin and Norton transformations, all circuits can be formulated into the basic building blocks of LIM, nodes and branches. A node, shown in Fig. 4.1a, is constructed as a parallel combination of a current source, a conductance, and a capacitance to ground. Two different nodes are connected by a current-carrying branch. A branch, shown in Fig. 4.1b, is a series combination of a voltage source, a resistance, and an inductance. In order to solve for the node voltages and branch currents, LIM discretizes the time variable so the voltages and currents are collected in alternating half time steps. The voltages are solved at half time steps while the currents are solved at full time steps in a leapfrog manner. This scheme is similar to Yee's method for discretizing Maxwell's equations in the finite-difference time-domain (FDTD) formulation [35].

To find the voltage update equation, we start by writing Kirchhoff's current law (KCL) at node i of Fig. 4.1a using the semi-implicit LIM formulation

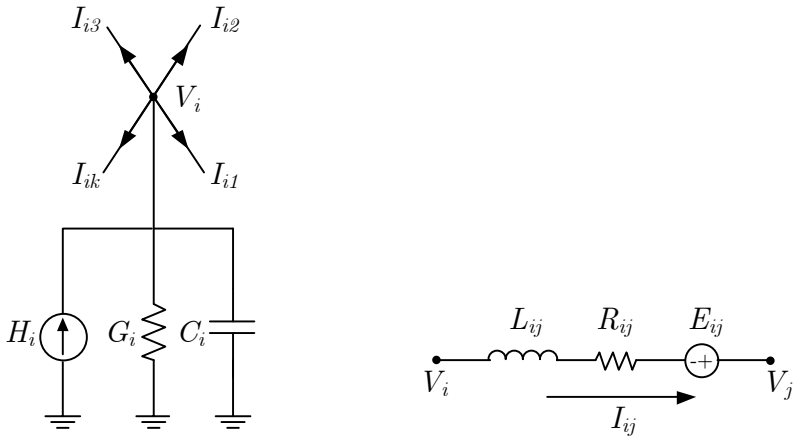

(a) LIM node. (b) LIM branch.

Figure 4.1: Topologies of basic LIM elements.

[36]

$$C_i\left(\frac{V_i^{n+1/2}-V_i^{n-1/2}}{\Delta t}\right)+\frac{G_i}{2}(V_i^{n+1/2}+V_i^{n-1/2})=-\sum_{k=1}^{M_i} I_{ik}^n+H_{ij}^n \quad (4.1)$$

and solving (4.1) for $V_i^{n+1/2}$

$$V_i^{n+1/2}=\frac{V_i^{n-1/2}(2C_i-G_i\Delta t)+2\Delta t(H_{ij}^n-\sum_{k=1}^{M_i} I_{ik}^n)}{2C_i+G_i\Delta t}. \quad (4.2)$$

Next, we find the current update equation by writing Kirchhoff's voltage law (KVL) at branch ij in Fig. 4.1b

$$V_i^{n+1/2}-V_j^{n+1/2}=L_{ij}\left(\frac{I_{ij}^{n+1}-I_{ij}^n}{\Delta t}\right)+\frac{R_{ij}}{2}(I_{ij}^{n+1}+I_{ij}^n)-E_{ij}^{n+1/2} \quad (4.3)$$

and solving (4.3) for the next current step, I_{ij}^{n+1}, yielding

$$I_{ij}^{n+1}=\frac{I_{ij}^n(2L_{ij}-R_{ij}\Delta t)+2\Delta t(E_{ij}^{n+1/2}+V_i^{n+1/2}-V_j^{n+1/2})}{2L_{ij}+R_{ij}\Delta t}. \quad (4.4)$$

Equations (4.2) and (4.4) require capacitance at each node and inductance at each branch [36]. These reactances create latency in the circuit. These latencies prevent a change in a node's voltage from affecting anything but

the currents of its adjacent branches during the span of any given time step. Similarly, they prevent a change in a branch's current from affecting anything but the voltages of its source and sink nodes during the span of a single time step. This makes the matrix formulation of LIM only locally dense, which enables it to run with linear numerical complexity with respect to the number of nodes and branches [37]. If a node does not have capacitance or a branch does not have inductance, fictitious values for these reactances must be inserted for the algorithm to be able to run. These fictitious reactances can distort the answer so they are made very small to minimize their impact. Similar to FDTD, LIM is only stable for time steps smaller than a certain upper bound, as discussed by [38], [39], and [40]. This upper bound is a function of the smallest inductances and capacitances in the circuit. Therefore there is a tradeoff: choosing small fictitious reactances will require a small time step that will result in long simulation times, whereas using larger fictitious reactive elements will allow for a larger time step but might also distort the final results.

The semi-implicit form, which averages the present and future values of the voltage across the conductance in (4.1) and the present and future values of the current through the resistance in (4.3), has better stability characteristics than the implicit or explicit forms and it is second-order accurate with respect to the time step, Δt [36].

4.2 Extension of LIM to Model CMOS Devices

Since most I/O circuits contain complementary metal-oxide-semiconductor (CMOS) devices, we use an extension to LIM outlined in [41] in order to model these elements. A CMOS device is represented by a branch for which the drain current is determined by the gate, drain, and source node voltages, as shown in Fig. 4.2.

Any behavioral model can be used to relate I_D from V_G, V_S, and V_D, but we follow [41] and use the Shichman-Hodges model as originally described in [42] for its simplicity. The Shichman-Hodges model describes the behavior

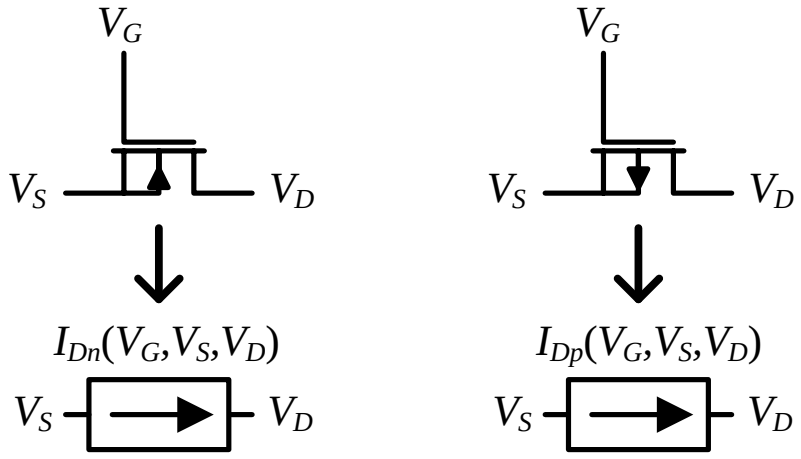

(a) NMOS (b) PMOS

Figure 4.2: NMOS and PMOS transistors are described by LIM branches whose currents are controlled by the gate, source, and drain voltages. A behavioral model like the Shichman-Hodges model can be used to determine the drain current from these voltages and the physical properties of the transistor.

of a NMOS with the composite function

$$\begin{gathered} I_{Dn} = 0, \\ V_G - V_S < V_{Tn}; \quad V_D - V_S \geq 0 \end{gathered} \tag{4.5a}$$

$$\begin{gathered} I_{Dn} = \frac{K_n W_n}{L_n} \left(V_G - V_S - V_{Tn} - \frac{1}{2}(V_D - V_S)\right)(V_D - V_S), \\ V_G - V_S > V_{Tn};\ 0 < V_D - V_S < V_G - V_S - V_{Tn} \end{gathered} \tag{4.5b}$$

$$\begin{gathered} I_{Dn} = \frac{K_n W_n}{2L_n}(V_G - V_S - V_{Tn})^2, \\ V_G - V_S > V_{Tn};\ V_D - V_S > V_G - V_S - V_{Tn} \end{gathered} \tag{4.5c}$$

where K_n is the NMOS process conductance parameter, W_n is the NMOS transistor width, and L_n is the NMOS transistor length.

The same model describes the behavior of a PMOS with the composite function

$$\begin{gathered} I_{Dp} = 0, \\ V_G - V_S > V_{Tp}; \quad V_D - V_S \leq 0 \end{gathered} \tag{4.6a}$$

$$I_{Dp} = \frac{-K_p W_p}{L_p}\left(V_G - V_S - V_{Tp} - \frac{1}{2}(V_D - V_S)\right)(V_D - V_S), \quad V_G - V_S < V_{Tp}; \quad 0 > V_D - V_S > V_G - V_S - V_{Tp} \tag{4.6b}$$

$$I_{Dp} = \frac{-K_p W_p}{2L_p}(V_G - V_S - V_{Tp})^2, \quad V_G - V_S < V_{Tp};\ V_D - V_S < V_G - V_S - V_{Tp} \tag{4.6c}$$

where K_p is the PMOS process conductance parameter, W_p is the PMOS transistor width, and L_p is the PMOS transistor length. The Shichman-Hodges model, which splits the behavior of NMOS and PMOS devices into cutoff, linear, and saturation regions, is generally designated a level 1 transistor model and thus, in the case described above, it is frequency-independent.

There are many additional extensions to LIM, all of which can be useful for modeling I/O buffer circuits but are outside the scope of this dissertation. These extensions include methods for simulating dependent sources, blackbox macromodeling, and phase-locked loops with LIM [43]. LIM can also be used to simulate IBIS models [44].

4.3 IBIS Model Composition

Our next signal integrity topic is IBIS, which is the industry standard for modeling I/O buffers. IBIS 1.0 was introduced by the IBIS Open Forum in 1993 to provide a vendor-neutral, simulation tool-neutral standard for specifying the electrical behavior of integrated circuit I/O buffers [45]. Subsequent versions of IBIS have allowed it to model the dynamic switching behavior of a buffer and have enabled support for modeling complex I/O behavior by linking the IBIS model with analog and mixed signal extensions of hardware description languages, such as VHDL-AMS and Verilog-AMS, as well as SPICE netlists. More recent updates have introduced an Algorithmic Modeling Interface (AMI), which allows for a model developer to include C++ scripts that perform software approximations of the complicated signal processing techniques that are used in modern I/O buffers. We will discuss IBIS-AMI further in Sec. 4.5.

The basic IBIS output model, based on the equivalent circuit shown in Fig. 4.3, includes a pullup network, a pulldown network, a power clamp network, and a ground clamp network. These are all described by current vs. voltage (I-V) tables that need not be linear. The parasitic resistance, inductance,

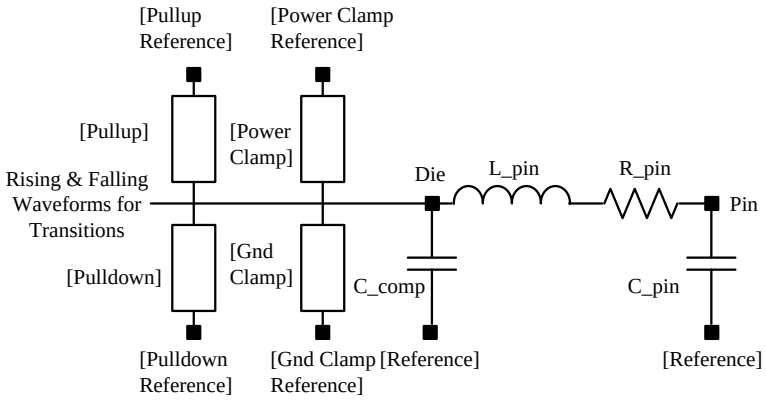

Figure 4.3: IBIS output buffer model.

and capacitance are all described by lumped elements. For the discussion in this dissertation, we will be ignoring everything but the pullup and pulldown networks.

The switching dynamics of the system are described by voltage vs. time (V-t) tables that chart the response of the buffer to bit transitions at its input. These rising and falling V-t tables are generated for a variety of voltage/resistance terminations: typically, V_{cc} and R_{out} or Gnd and R_{out}, where V_{cc} is the voltage of the high rail, Gnd is the voltage of the low rail, and R_{out} is the typical output termination resistance that the buffer sees during operation. These waveforms are combined to generate dynamic functions that regulate the contributions of the pullup and pulldown networks when the buffer is switching during operation [46]. All of these tables and parameters are compiled into a *.ibs file with a specific format as outlined in [5].

Each revision of IBIS comes packaged with a golden parser, called ibischk, that can be freely downloaded as an executable [47]. The executable can analyze any *.ibs file to check for compatibility with the standard. The IBIS Open Forum provides very little guidance on how to perform simulations with IBIS files, leaving that implementation to the electronic design automation (EDA) tool vendor. One example IBIS simulator is based on a LIM framework and has been shown to have excellent convergence characteristics when compared to other methods [44].

4.4 IBIS Model Generation

The methods for proper generation of the I-V and V-t tables are outlined in the IBIS Cookbook [48]. The Pulldown I-V table is generated by first applying a DC voltage bias to the input of the circuit to put the output in the low state (high input bias for inverting buffers, low for non-inverting). Then, a DC sweep of up to 100 different voltages spanning from $-V_{cc}$ to $+2V_{cc}$ is run at the output and the corresponding current into the output port is measured for each voltage. This steady-state measurement can be approximated by applying a low-frequency voltage waveform that spans the entire voltage range and then measuring the corresponding current waveform going into the output port. The change in the voltage waveform should be gradual enough that the reactive effects of the circuit are negligible and the current measurement is approximately DC. The Pullup I-V table is generated in a similar manner, except the input is biased to put the output in the high state.

A Rising V-t curve is generated by terminating the circuit's output with one of the desired voltage/resistance terminations mentioned above, applying an ideal rising ramp function with a rise time similar to what will be used in device operation, and measuring up to 1,000 points of the output voltage waveform. A Falling V-t curve is generated in a similar way, just using an ideal falling ramp function with a falling time similar to that seen in normal device operation.

An open source tool for generating IBIS files called s2ibis [49] takes a SPICE netlist with an accompanying information file, generates the I-V and V-t curves, and outputs a properly formatted IBIS file. This tool will be compared to the process developed in Chapter 6, named x2ibis, in which X-parameter measurement files for an output buffer are first generated under specific conditions and then are used to generate IBIS current-voltage (I-V) and voltage-time (V-t) tables.

4.5 Algorithmic Modeling Interface

As the bit rates of I/O links have increased, energy at higher frequencies is being passed through the channel, where this high-frequency content

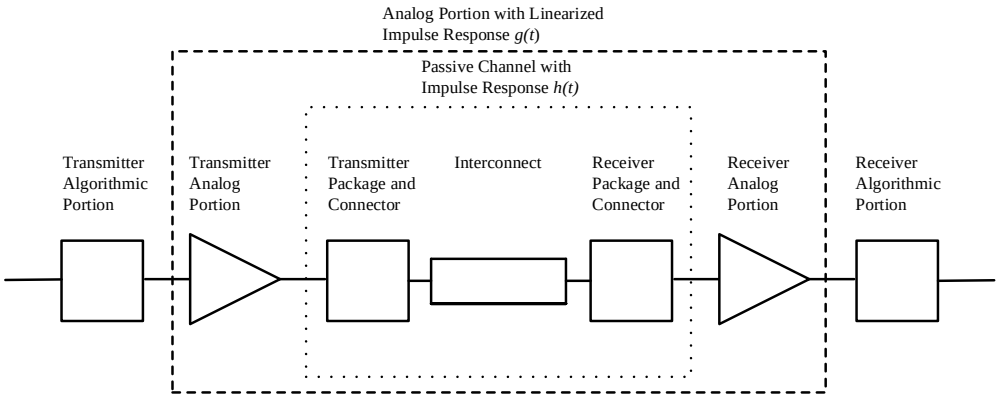

Figure 4.4: The IBIS-AMI simulation flow separates the transmitter and receiver into analog and algorithmic components.

experiences more attenuation and dispersion effects. In order to minimize the bit error rate (BER) of the information being sent through the channel, I/O links now contain complicated circuits that are potentially nonlinear and time-varying such as adaptive equalizers, automatic gain control circuits, or clock recovery components. These circuits combat the performance challenges of operating in the gigabits-per-second range. With the release of IBIS 5.0 and later IBIS 5.1 and IBIS 6.0, the IBIS Open Forum introduced the IBIS Algorithmic Modeling Interface (IBIS-AMI) [5]. Because I/O links have become so large, it is not practical to perform full transistor-level simulations of an entire link. IBIS-AMI is a method for performing behavioral modeling of a link.

An in-depth analysis of IBIS-AMI is outside the scope of this document, but [50], [51], and [52] provide excellent descriptions of the structure of IBIS-AMI and the simulation flow. To summarize, IBIS-AMI divides a buffer into an analog portion identical to traditional IBIS that interfaces with the interconnect and an algorithmic portion that is assumed to be electrically isolated from it, as shown in Fig. 4.4. There are two different IBIS-AMI simulation flows, statistical and bit-by-bit. First, we describe the bit-by-bit simulation.

The IBIS-AMI simulation flow begins by obtaining an impulse response $h(t)$ of the passive channel and then approximating the response of the entire analog channel by an impulse response $g(t)$. One approach to doing this is to apply a unit step input to the entire analog channel, which is composed of

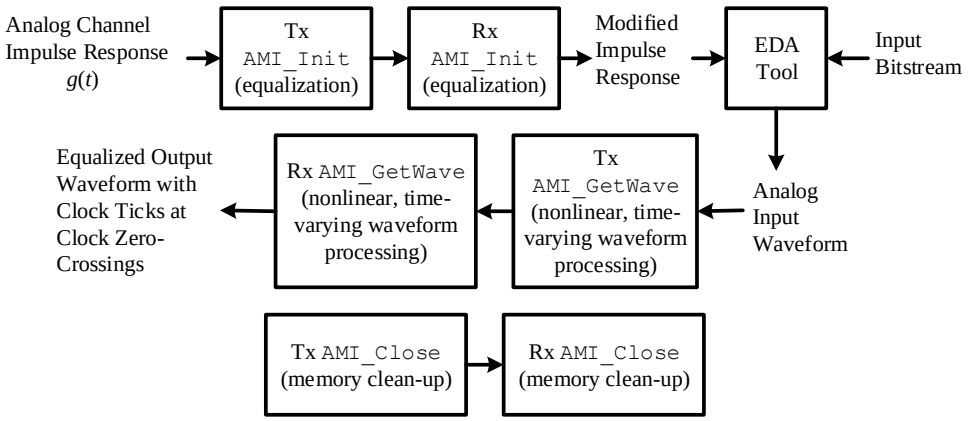

Figure 4.5: The AMI simulation flow first performs all of the LTI processing in the Tx and Rx `AMI_Init` functions. It then takes this modified impulse response and the input bitstream to form the input waveform. The NLTV processing is then performed on the input waveform in the Tx and Rx `AMI_GetWave` functions, which output the final waveform. The Tx and Rx `AMI_Close` functions are then run to deallocate memory in the computer.

the transmitter, the channel, and the receiver. We then differentiate the step response at the receiver output to find the impulse response. This process effectively linearizes the analog channel [53]. This approximation is only valid when the nonlinear behavior of the buffer is taken into account in the algorithmic portion.

The EDA tool then inputs $g(t)$ into the algorithmic portion of the model, whose flow is shown in Fig. 4.5. The algorithmic model has been standardized to include three high-level functions, `AMI_Init`, `AMI_GetWave`, and `AMI_Close`. The transmitter (Tx) `AMI_Init` takes as its input $g(t)$, which is sampled and is essentially an array, and performs LTI signal processing functions on it, such as feed-forward equalization (FFE) or pre-emphasis. This modified impulse response is then inputted into the receiver (Rx) `AMI_Init` function, which might approximate an Rx continuous-time linear equalization with a difference equation, to output a further modified impulse response.

The EDA tool then combines this modified impulse response with the input bitstream to form the input waveform, which is sent to the Tx `AMI_GetWave` function and then to the Rx `AMI_GetWave` function. The Rx `AMI_GetWave` is generally the most complicated function in the entire AMI model, as it is used to model highly nonlinear time-varying (NLTV) components like a decision-

feedback equalizer (DFE) circuit, a clock-data recovery (CDR) circuit, or an automatic gain control (AGC) circuit. For a description of the structure or function of any of these circuits, see [54]. The output waveform from the Rx `AMI_GetWave` can be processed to generate an eye diagram or a bathtub curve. Finally, the Tx and Rx `AMI_Close` functions are run to deallocate computer memory.

The statistical simulation requires the entire AMI model to be linear time-invariant (LTI). It omits the `AMI_GetWave` functions, which are the only parts of the flow that contain NLTV behavior. It generates eye diagrams by convolving the equalized analog channel impulse response with a probability distribution function describing the input signal variations.

The entire AMI model is contained in two files that are referenced by the top-level *.ibs file. The first is a *.ami file contains the input arguments to each of the three standard AMI functions, including any model-specific parameters that the developer has exposed. The second is a *.dll or a *.so file, depending on the operating system of the computer running the simulation, that contains the three compiled AMI functions and any supporting code. Because these files are compiled, the intellectual property contained in the model remains hidden.

CHAPTER 5

LIM2X

Now that we have outlined the X-parameter formalism and given some background into signal integrity, we begin our use of X-parameters for signal integrity applications. The first step is to ensure that X-parameters can be accurately and efficiently generated for extremely large circuits like I/O buffers. The current state-of-the-art method for generating X-parameters via simulation is harmonic balance (HB), which is outlined in Sec. 3.2. While this method works very well for most microwave circuits, these circuits are generally not particularly large, at most on the order of hundreds of transistors. Because HB is inherently based on MNA, it has to invert a matrix as part of its algorithm, just like SPICE does. Matrix inversion has super-linear numerical complexity with respect to the number of elements involved. This puts HB at a disadvantage when circuit sizes reach the order of thousands or tens of thousands of transistors, as they commonly do in modern I/O buffers, especially since the number of unknowns in the HB algorithm also at best scales linearly with the number of harmonics. This motivates the use of a simulation framework that scales well with increasing numbers of elements.

The latency insertion method (LIM), whose basic formulation was described in Sec. 4.1 and whose extension to simulating with CMOS devices was shown in Sec. 4.2. LIM is an all-purpose circuit solver with linear numerical complexity. This property of LIM positions it as an attractive tool for the generation of the X-parameters for very large I/O buffer circuits. The purpose of this chapter is to show how we can use the LIM toolbox and extend its capabilities to include X-parameter generation, called lim2x. To do so, we first determine the proper port excitations and terminations. Next, we explain the processing of the output voltages and currents generated by the LIM transient simulation needed to extract the X-parameters. We then demonstrate lim2x for a simple I/O buffer circuit, the basic inverter. We show comparisons of the generated results with those made by HB. Finally,

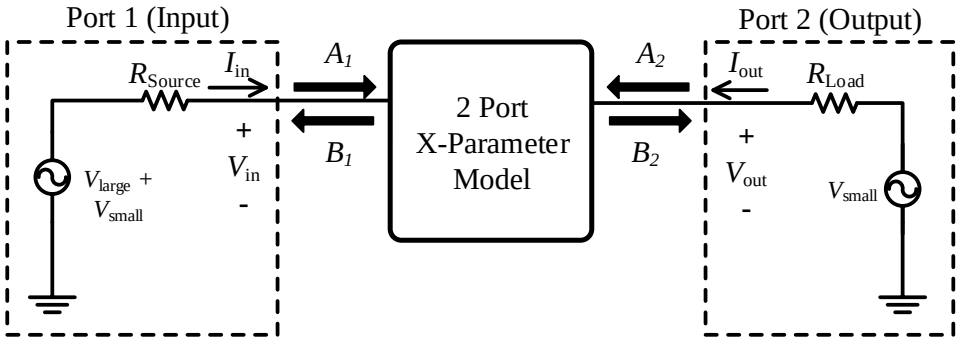

Figure 5.1: Two-port described by X-parameters with termination and source. Port 1 is the input port and port 2 is the output port. Only port 1 has the large-signal excitation.

we offer a critique of the method and possible avenues for its expansion.

5.1 Excitations and Terminations Needed for X-Parameter Extraction

Here we leverage the theory of Sec. 2.9 to implement the lim2x process. Single large-tone X-parameter extraction requires analysis of the circuit's response to a particular excitation for each fundamental frequency, harmonic, and input power level. The excitation design was first discussed in [18] and later improved in [19] to require fewer measurements. This is the method used here. In the following analysis, two ports are used, but the result generalizes. Since I/O buffer circuits can be treated as unidirectional, port 1 and port 2 are designated the input and output ports, respectively, as shown in Fig. 5.1.

The total excitation is the sum of a large-signal voltage tone at the fundamental frequency f and a small-signal voltage tone at a slight offset in frequency from a harmonic of the large-signal tone. The large-signal voltage tone, which is $A_{1,1}$, is

$$V_{\text{large}} = |A_{1,1}| \sqrt{\frac{2}{Z_C}} (Z_S + Z_C) \cos\left(2\pi f t + \arg\left(A_{1,1}\right)\right) \tag{5.1}$$

and the small-signal voltage tone, which is either $A_{1,l}$ or $A_{2,l}$ depending on

which port it is applied, is

$$V_{\text{small}} = |\delta| \cdot \cos\left(2\pi(lf + \epsilon)t + \arg(\delta)\right). \tag{5.2}$$

In these equations, $|A_{1,1}|$ is the magnitude of the normalized incident wave, Z_C is the characteristic impedance of the system (normally 50 Ω), Z_S is the source impedance of the excitation port, $\arg(A_{1,1})$ is the phase to which all other signals are referenced (usually set to zero for convenience), ϵ is a frequency offset, and δ is a complex number containing the magnitude and phase of the small signal. The phase of δ can take any value but it needs to be known. The ϵ frequency offset serves the purpose of separating the X-parameters of types S and T from each other in frequency, thus preventing aliasing and allowing the extraction of both in one measurement. The ϵ and δ parameters should be as small as possible to ensure that the approximations used in the X-parameter formalism derivation are valid, but larger values make it easier to process the circuit's output waveforms through Fourier series analysis. Some general rules of thumb that produce good results are

$$|\delta| < \frac{|A_{1,1}|}{20}\sqrt{\frac{2}{Z_C}}\,(Z_S + Z_C) \tag{5.3}$$

and

$$\epsilon < \frac{f}{10}. \tag{5.4}$$

The scaling factor comes from the definition of power waves, a voltage divider, and root-mean-square to peak-to-peak conversion.

The excitation is applied for all pertinent values of l to determine the contribution at the qth harmonic of port k from the lth input harmonic. To calculate $X^{(S)}_{k,q;2,l}$ and $X^{(T)}_{k,q;2,l}$ parameters, the small harmonic tone is to be applied at port 2 while the large tone is still applied at port 1. The output impedance termination is merely a resistor with the desired characteristic impedance of the system.

5.2 LIM Output Processing

The LIM engine solves for peak voltages and currents, so the following definitions are necessary to convert these quantities to power waves

$$A_1 = \frac{(V_{\text{in}} + Z_C I_{\text{in}})}{\sqrt{8 \cdot \text{Re}(Z_C)}} = \sum_l A_{1,l} \tag{5.5a}$$

$$B_1 = \frac{(V_{\text{in}} - Z_C I_{\text{in}})}{\sqrt{8 \cdot \text{Re}(Z_C)}} = \sum_k B_{1,k} \tag{5.5b}$$

$$A_2 = \frac{(V_{\text{out}} + Z_C I_{\text{out}})}{\sqrt{8 \cdot \text{Re}(Z_C)}} = \sum_l A_{2,l} \tag{5.5c}$$

$$B_2 = \frac{(V_{\text{out}} - Z_C I_{\text{out}})}{\sqrt{8 \cdot \text{Re}(Z_C)}} = \sum_k B_{2,k} \tag{5.5d}$$

where each of the voltages is defined at the ports of the network and each of the currents is defined as pointing into the network, similar to the conventions used for scattering parameters. The second equality separates the power wave into a sum of its contributions from each harmonic, as defined in (2.54).

We then condition the signal to improve our results. The first step is to truncate the initial transient behavior from the beginning of the waveforms. Next, we truncate more samples from the beginning so that our time series data have as close to an integer number of periods of the large signal as possible. Doing this minimizes the spectral leakage from the large tone, which otherwise can very easily obscure the adjacent small tones [55]. As demonstrated in Sec. 2.9, the $X^{(S)}_{p,k;q,l}$ and $X^{(T)}_{p,k;q,l}$ are

$$X^{(S)}{}_{p,k;q,l} = \frac{\hat{B}_p\left(2\pi\left(kf + \epsilon\right)\right)}{\hat{A}_q\left(2\pi\left(lf + \epsilon\right)\right)} \tag{5.6a}$$

$$X^{(T)}{}_{p,k;q,l} = \frac{\hat{B}_p\left(2\pi\left(kf - \epsilon\right)\right)}{\hat{A}^*_q\left(2\pi\left(lf + \epsilon\right)\right)} e^{j2\arg(\delta)} \tag{5.6b}$$

where $\hat{B}_p\left(2\pi\left(kf + \epsilon\right)\right)$ is the upper sideband contribution at ϵ offset from harmonic q at port p, and $\hat{B}\left(2\pi\left(kf - \epsilon\right)\right)$ is the lower sideband contribution at ϵ offset from harmonic q at port p. Last, $\hat{A}_q\left(2\pi\left(lf + \epsilon\right)\right)$ is the upper sideband contribution at ϵ offset from harmonic l at port q and $\hat{A}^*_q\left(2\pi\left(lf + \epsilon\right)\right)$ is its complex conjugate. This is the small-signal tone that is input into the circuit. These Fourier coefficients can be calculated in many different ways.

In one method, $\hat{B}_p\left(2\pi\left(kf+\epsilon\right)\right)$ is calculated from B_p by

$$\hat{B}_p\left(2\pi\left(kf+\epsilon\right)\right)=\frac{2}{N_t}\sum_{n=0}^{N_t-1}B_p(t_n)\left[e^{-2\pi(kf+\epsilon)t_n}\right] \tag{5.7}$$

where $t_n=t_0+n\Delta t$, t_0 is the arbitrary starting time for the calculation, and N_t is the number of samples over which the calculation is performed.

For the calculation of the FB-terms from (2.54), it is often easier to eliminate the small-signal stimulus entirely and perform Fourier processing of the output waves so that

$$X_{p,k}^{(FB)}=\hat{B}_p\left(2\pi kf\right). \tag{5.8}$$

Other methods for extracting the Fourier coeffcients are with the fast Fourier transform (FFT) or through the use of a Goertzel filter [55]. The frequency resolution increases with longer sampling times, but this requires more memory because of the longer simulation time. Increasing ϵ and δ lessens the need for very long simulation times, but can result in a severe decrease in accuracy when the rules of thumb in (5.3) and (5.4) are not followed.

5.3 Example and Numerical Results

The lim2x process was run for the circuit in Fig. 5.2 with LIM and the X-parameters generated were compared to those generated by HB with the Agilent Advanced Design System (ADS) [34]. LIM inserts a fictitious series inductor at the input branch and a fictitious shunt capacitor at the output node. The gate-to-source capacitances were modeled with nodal shunt capacitances at the gate.

Several small-signal X-parameters were generated for 28 frequencies between 10 MHz and 10 GHz at an input power level in the nonlinear region of the buffer. The values for the fictitious capacitor and inductor and the total simulation runtime were scaled with frequency in order to guarantee minimal distortion of the data and at least 1000 periods of the steady-state circuit response for accurate Fourier series coefficient extraction.

Figure 5.3 displays the magnitudes and phases generated by both LIM

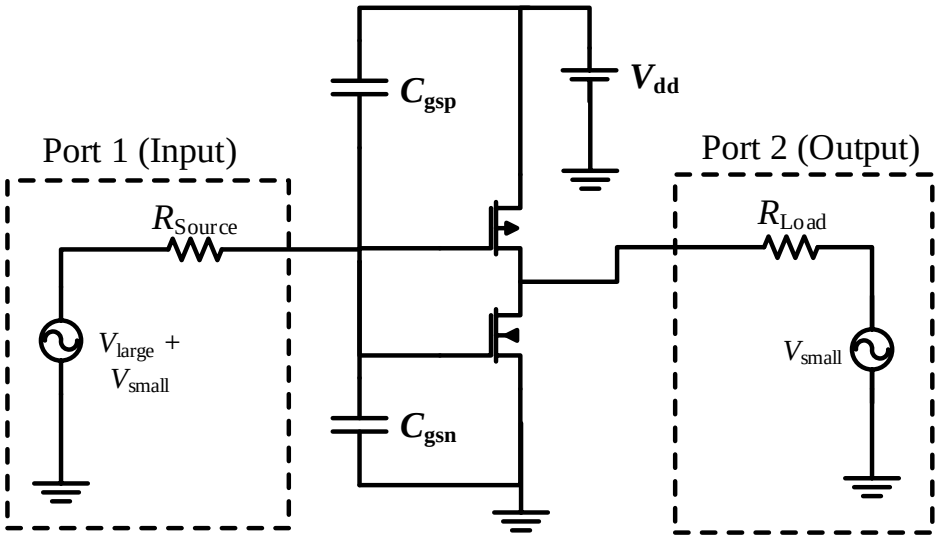

Figure 5.2: Simple inverter circuit used for X-parameter generation.

and HB for $X^{(S)}_{2,1;1,2}$, $X^{(S)}_{2,2;1,2}$, and $X^{(S)}_{2,3;1,2}$. Figures 5.4 and 5.5 display the magnitude comparisons for various other parameters, including $X^{(S)}_{2,2;2,2}$ and $X^{(S)}_{2,3;2,2}$ for which the harmonic small tone was applied at port 2.

Next, several large-signal X-parameters were generated for a wide range of input powers at a resolution of 1 dB at 1 GHz for at least 1000 periods of the steady-state circuit response to ensure accurate Fourier series coefficient extraction. Figure 5.6 displays the magnitude and phase of $X^{(FB)}_{1,1}$ and $X^{(FB)}_{2,1}$ versus input power as generated by LIM and HB. Figure 5.7 shows the magnitude and phase of $X^{(FB)}_{2,2}$ and $X^{(FB)}_{2,3}$ versus input power as generated by LIM and HB.

The X-parameters generated with LIM closely match those generated by HB in all instances. Some of the small discrepancies between the two simulators may be a result of the fictitious reactive elements. These could be set to smaller values at the expense of a smaller time step and longer simulation times. Overall, lim2x is shown to produce results that match those generated by HB.

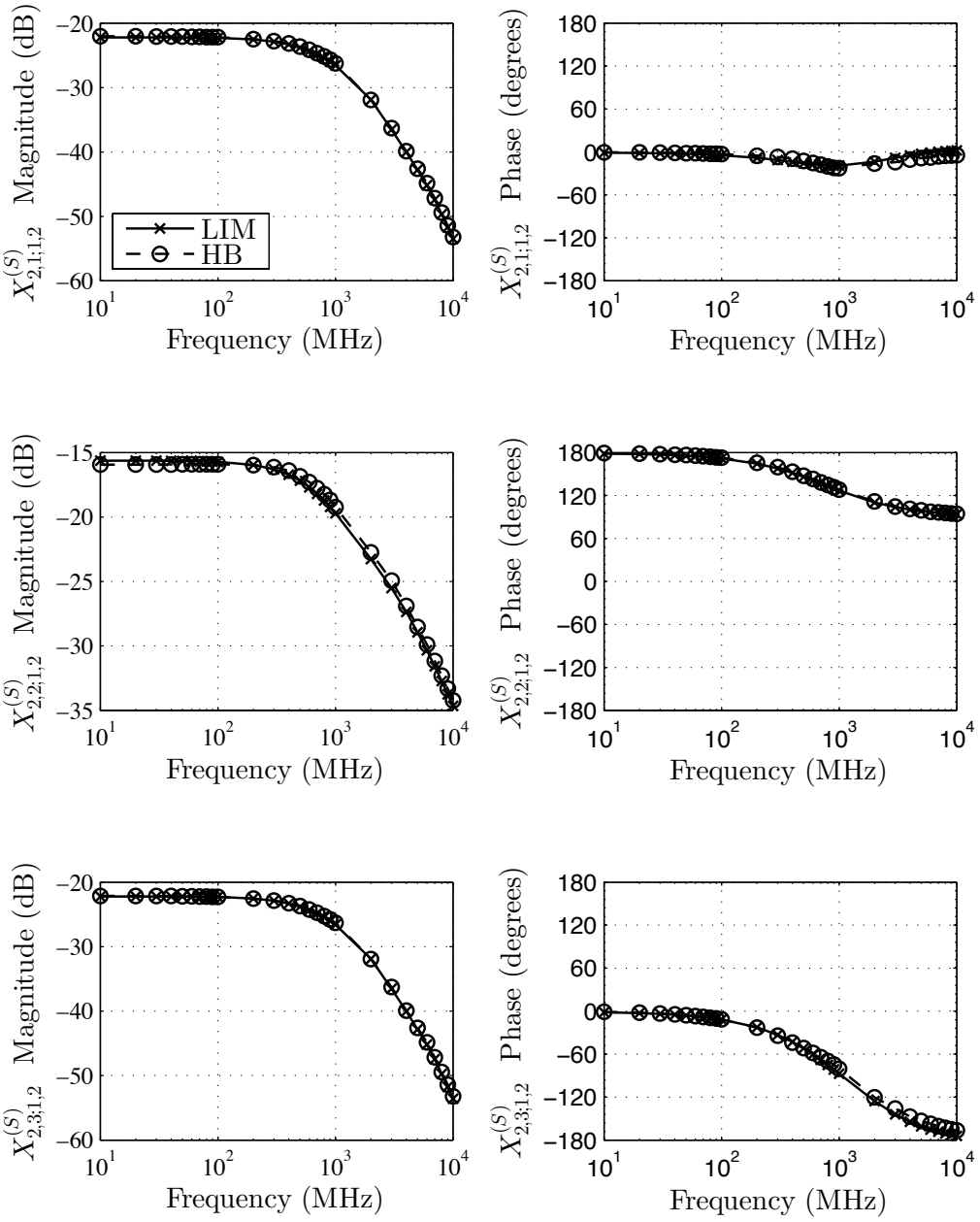

Figure 5.3: Comparison of magnitude and phase of $X^{(S)}_{2,1;1,2}$, $X^{(S)}_{2,2;1,2}$, and $X^{(S)}_{2,3;1,2}$ parameters generated by LIM and HB.

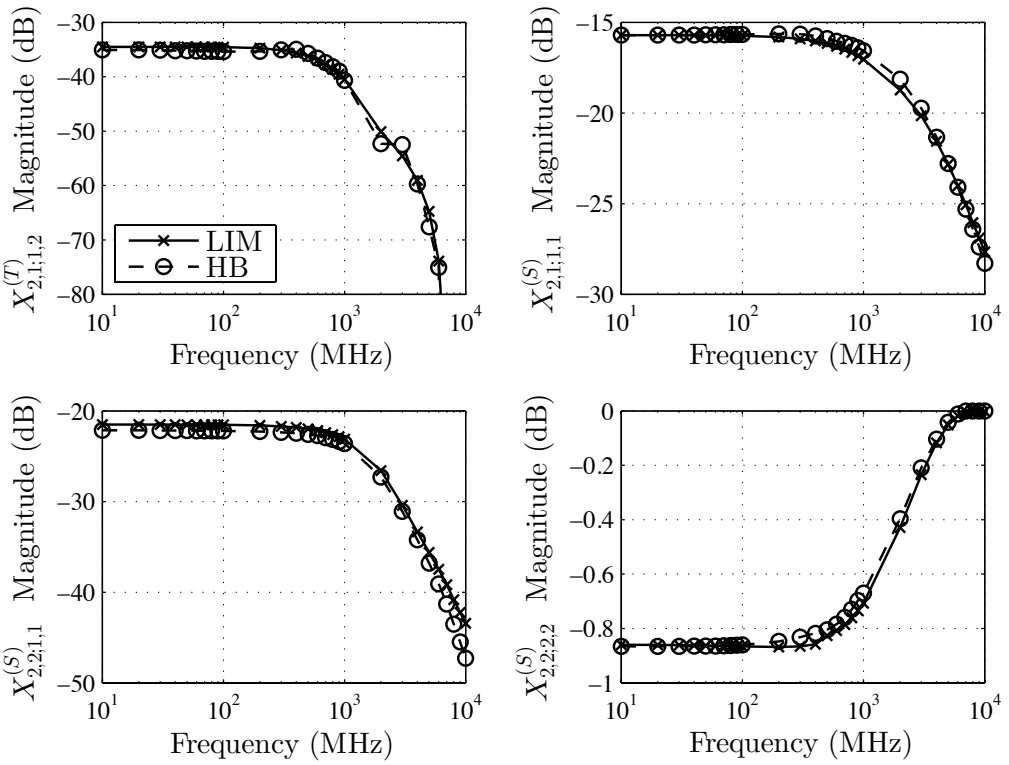

Figure 5.4: Comparison of $X^{(T)}_{2,1;1,2}$, $X^{(S)}_{2,1;1,1}$, $X^{(S)}_{2,2;1,1}$, and $X^{(S)}_{2,2;2,2}$ parameters generated by LIM and HB.

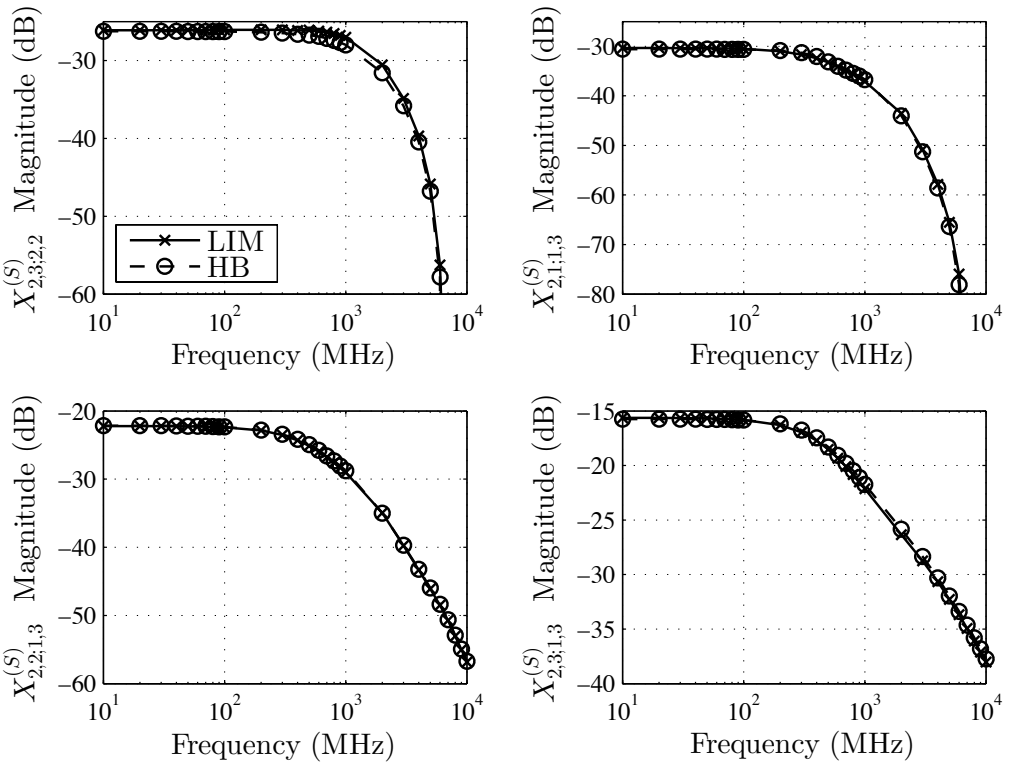

Figure 5.5: Comparison of $X^{(S)}_{2,3;2,2}$, $X^{(S)}_{2,1;1,3}$, $X^{(S)}_{2,2;1,3}$, and $X^{(S)}_{2,3;1,3}$ parameters generated by LIM and HB.

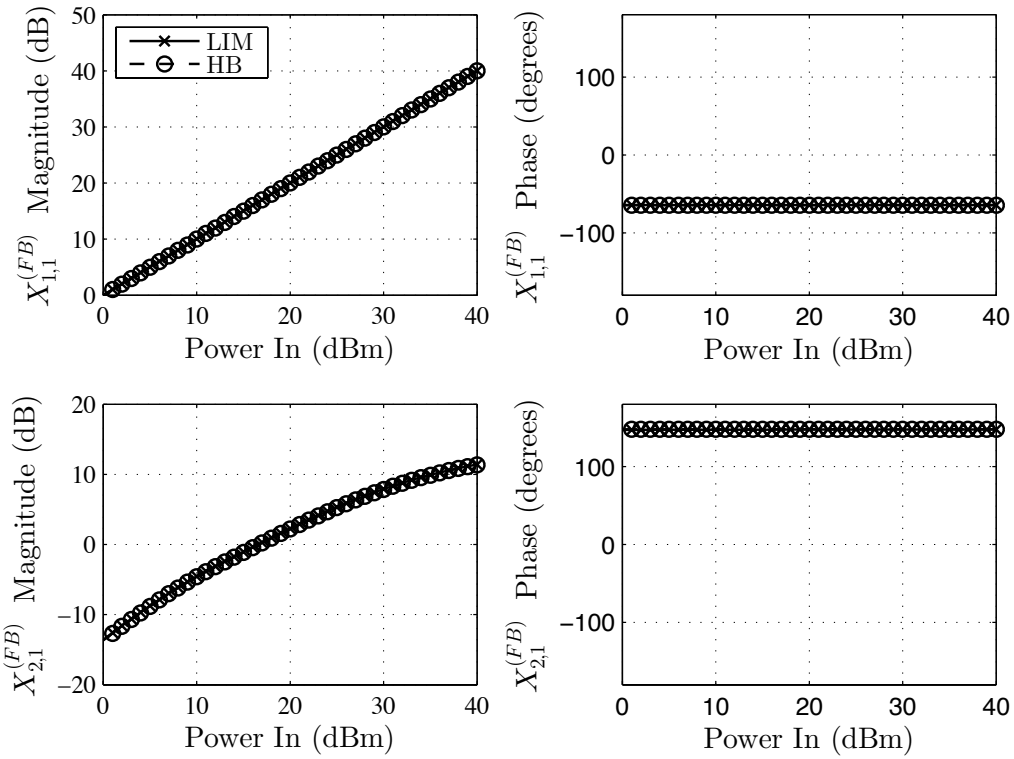

Figure 5.6: Comparison of the magnitude and phase of the large-signal $X_{1,1}^{(FB)}$ and $X_{2,1}^{(FB)}$ parameters versus input power at 1 GHz generated by LIM and HB.

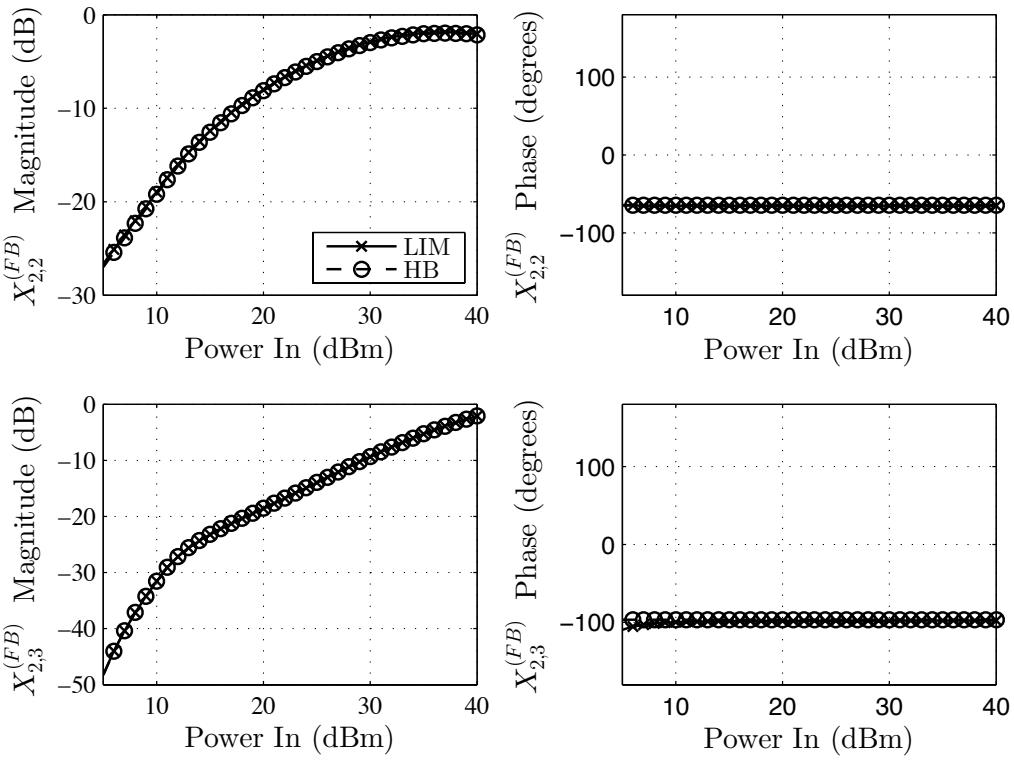

Figure 5.7: Comparison of the magnitude and phase of the large-signal $X_{2,2}^{(FB)}$ and $X_{2,3}^{(FB)}$ parameters versus input power at 1 GHz generated by LIM and HB.

5.4 Comments and Future Work

While lim2x was able to produce excellent results, it does entail a few concerns. First, all simulators have numerical rounding errors and for a transient simulation, the longer the simulation time, the more these errors can accumulate [56]. Since the transient simulations needed in lim2x have to run for many periods to allow for accurate X-parameter extraction, care must be taken to manage this error. In this chapter, we have shown that the lim2x process accurately generates X-parameters using LIM. Of future interest would be to develop a commercial-grade LIM simulator so as to perform some benchmarking on the performance of the lim2x process and identify any scenarios where it might outperform generation of X-parameters by HB. Part of this process would involve implementing some of the enhancements to the LIM algorithm, such as Partitioned LIM [57], which further optimizes the performance of LIM by partitioning the circuit so that portions with larger latencies can be run with a larger time step. Future work could also implement additional transistor models into LIM. Regardless, lim2x enables any LIM simulator to extend its utility to include X-parameter generation. Further, the X-parameter stimulus and extraction procedure outlined in this chapter can be applied to any time-domain simulation, including SPICE, to generate X-parameters in situations where an HB simulator is unavailable.

CHAPTER 6

X2IBIS

In Chapter 5, we used lim2x to demonstrate a time-domain method for generating X-parameters with a simulation engine that will scale well for very large circuits, the kinds we encounter when studying I/O buffers. Now that we have done so, we shift our focus to showing the efficacy of X-parameters for modeling the behavior of I/O buffers. As we discern how to accomplish this, we first note that the current industry standard for modeling the behavior of I/O buffers is IBIS, which we outlined in Sec. 4.3. IBIS is already established in the signal integrity culture, which despite all of the technological expansion happening as a part of it, carries significant inertia when it comes to adopting new measurement or modeling techniques. There is huge strategic value in first using X-parameters to generate IBIS models. Doing so will establish a baseline level of performance for using X-parameters to model I/O buffers from which we can expand.

Therefore, the topic of this chapter is x2ibis, a new process in which X-parameters are measured or simulated and then used in simulation to generate the fundamental components of an IBIS model, namely the I-V and V-t tables.

The entire process is shown in the flowchart in Fig. 6.1. This particular flow assumes that we are beginning with a SPICE netlist, but the same ideas can be used in the actual measurement of the X-parameters of a buffer with a nonlinear vector network analyzer (NVNA), which was briefly described in Sec. 3.1. In this chapter, we will first outline the X-parameter model simulation process. Then, we show how to use these simulated or measured X-parameter model files to generate the I-V and V-t tables.

Harmonic balance (HB) simulations, which are described in Sec. 3.2, can be used to generate *.xnp files, which contain X-parameter data, but separate X-parameter measurements must be taken for the I-V curves and the V-t curves. This is because the former is a one-port DC measurement with the

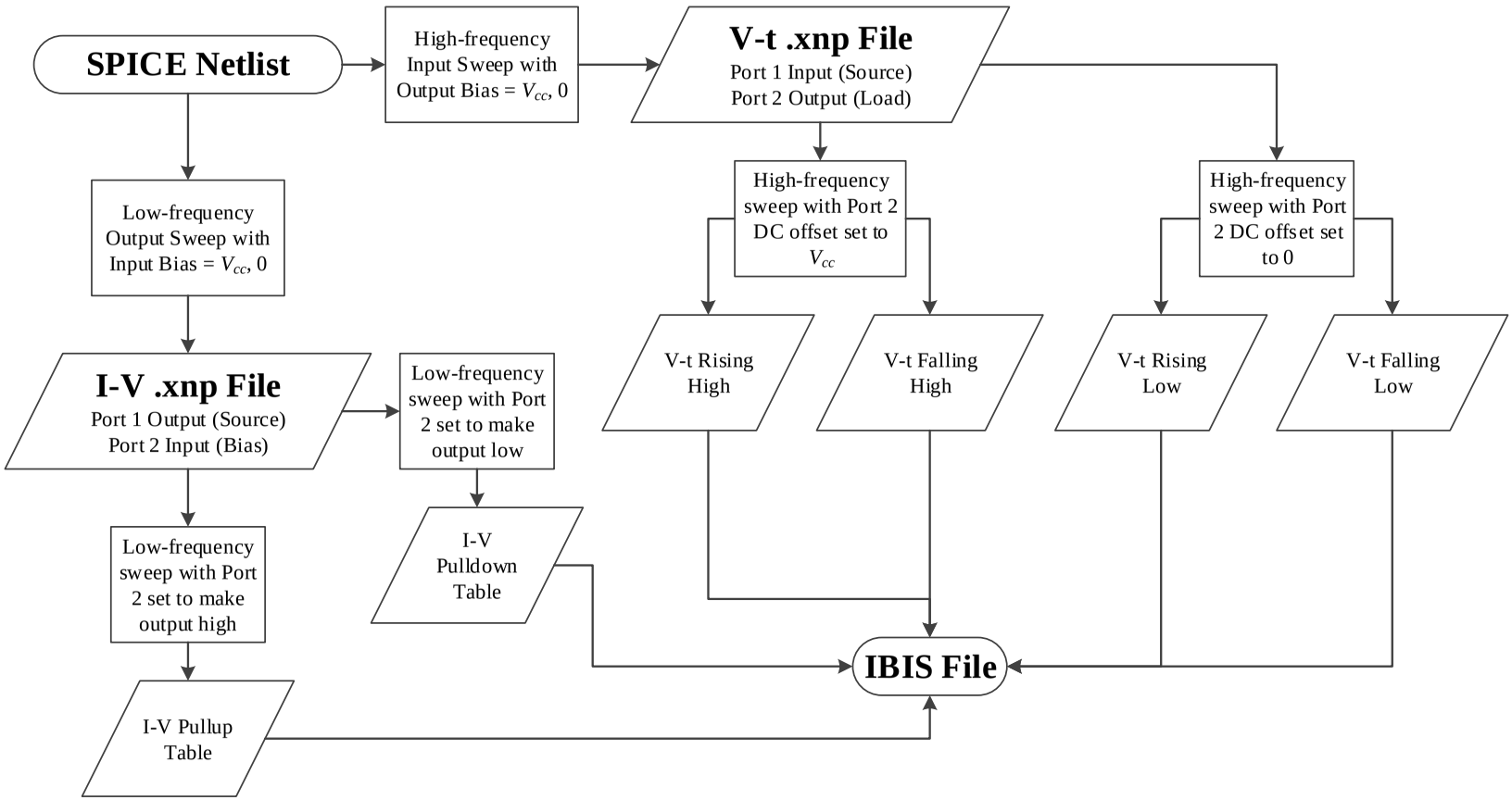

Figure 6.1: The x2ibis flow chart: Starting with the SPICE netlist, the user first generates different *.xnp files for the I-V and V-t tables. The user then uses these *.xnp files to generate the I-V and V-t tables.

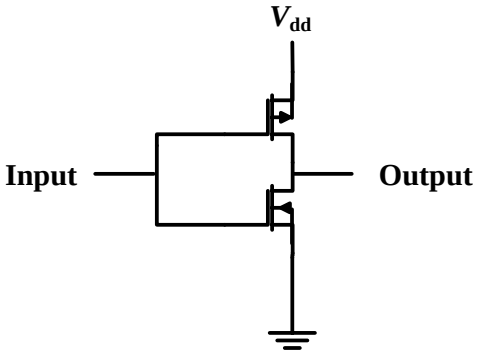

Figure 6.2: Simple inverter circuit used in this example of the x2ibis process.

large-signal at the output and the latter is a two-port microwave measurement with the large-signal at the input. All X-parameter simulations in this chapter have been performed with ports that have a characteristic impedance of 50 Ω in order to match the impedance of the ports of a standard NVNA, but this is not necessary because there are attachments to NVNAs that allow for port impedances to be transformed to any arbitrary complex value.

The x2ibis process is then demonstrated for a simple inverter and the performance of the resulting IBIS model is compared to that generated by s2ibis, which we described in Sec. 4.4.

6.1 Generating the X-Parameter Files

The test circuit in this example of the x2ibis process is a simple inverter shown in Fig. 6.2 with $V_{\mathrm{dd}} = 2.5V$. The typical supply pin labeling conventions for the field effect transistor (FET) are "V_{dd}" and "V_{ss}" for the positive and negative supply pins, respectively, but the IBIS convention is to identify the positive voltage supply as V_{cc} and the negative voltage supply as Gnd, so we will be following the IBIS convention in the rest of this discussion. As mentioned in Sec. 4.4, the IBIS Cookbook [48] provides recipes for the generation of the IBIS I-V and V-t curves. We will be approximating these recipes as well as possible within the X-parameter formalism.

Again, the I-V curve generation and the V-t curve generation are best

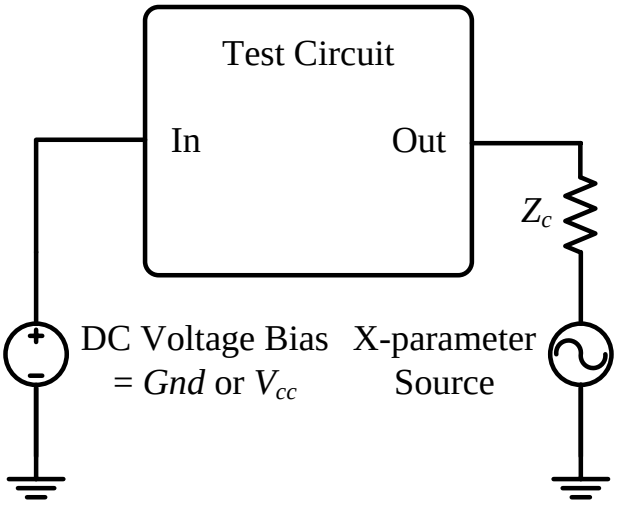

Figure 6.3: Measurement setup for the generation of the X-parameter file for the I-V curve generation. This measurement setup captures the DC behavior of the buffer.

separated into different processes because the former is a static one-port measurement where the large-signal tone is applied to the buffer's output port with the input port merely holding a DC voltage bias while the latter is the typical paradigm where the large-tone is applied to the input port and the output waveforms are of primary interest.

For I-V curve *.xnp file generation, the input port is connected to an X-parameter DC voltage bias of *Gnd* and V_{cc} and the output port is connected to an X-parameter source as shown in Fig. 6.3. The source has a DC voltage bias of 0.5 V_{cc} and $|A_{11}|$ to correspond to a peak-to-peak voltage of 3 V_{cc} as demonstrated in (5.1). It also has source impedance equal to the system impedance, Z_c. The frequency, f, of the simulation should be set as low as possible to approximate DC behavior best. For this test circuit, we used 11 harmonics, but more could be included for higher accuracy at the expense of having a slightly longer simulation and larger *.xnp file.

For V-t curve *.xnp file generation, the input port is connected to the X-parameter source and the output to an X-parameter load termination as shown in Fig. 6.4. The source should have a DC voltage bias of $0.5V_{cc}$ and $|A_{11}|$ to correspond to a peak-to-peak voltage of V_{cc}. The frequency should be set to $f = (t_{\text{rise}} + t_{\text{fall}})^{-1}$. The output should be connected to

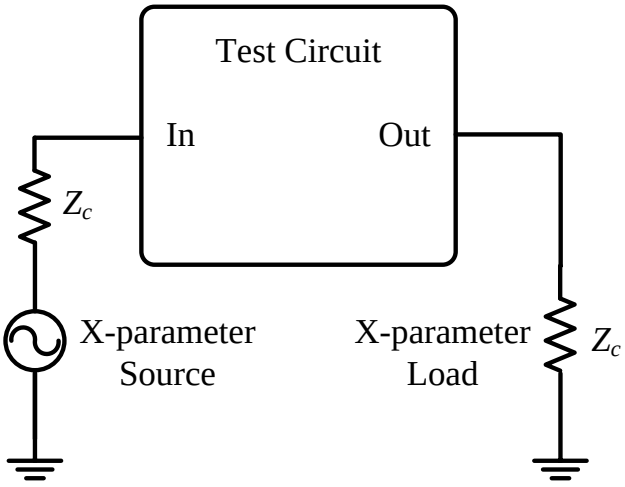

Figure 6.4: Measurement setup for the generation of the X-parameter file for the V-t curve generation. This measurement setup captures the switching behavior of the buffer.

an X-parameter load with DC voltage bias of Gnd and V_{cc}. Both input and output ports should have an impedance of Z_c. Using seven harmonics proved to be sufficient for this measurement, but more could be used for increased accuracy. To generate V-t tables for different rise and fall times, a user could always measure the X-parameters for multiple frequencies.

One of the biggest concerns with X-parameter measurements is the sheer number of parameters that are generated as the number of examined fundamental frequencies, harmonics, DC biases, input power levels, and measurement ports increases. With the current number of harmonics, the sizes of the two *.xnp files together totaled fewer than 100 kilobytes. Our restriction to include only one power level and one frequency for each measurement is the primary reason that the file is so small. This setup is justifiable because the inputs of I/O buffers generally do not vary much in amplitude or data rate. In circumstances where this assumption is not valid, more power levels or frequencies can be included in the .xnp file at the expense of a larger file.

6.2 Generating IBIS Tables from X-Parameter Files

Together, these two *.xnp files contain all of the information in the I-V and V-t tables of a normal IBIS file. At this point, these X-parameter files could be sent to a different individual with expertise in IBIS modeling to generate the IBIS file without exposing any of the intellectual property (IP) of the buffer design to that new individual. In the signal integrity community, this is an especially desirable characteristic.

In order to generate the desired curves from these *.xnp files, we insert them into HB simulations. These simulations will produce phasors, complete with harmonic contributions, of the scattered and incident waves, B and A, from which it is easy to calculate voltage and current phasors

$$V = \sqrt{Z_C}(A + B) \tag{6.1a}$$

$$I = \frac{(A - B)}{\sqrt{Z_C}}. \tag{6.1b}$$

The time-domain waveforms can then be generated from these phasors.

To calculate the Pulldown I-V Curve, we take the I-V *.xnp file, connect an HB source with impedance Z_c to the output with the same DC bias, power level, frequency, and number of harmonics as with the generation and connect the input directly to the appropriate DC voltage source to set the buffer in the low state. We extract the voltage and current waveforms from the simulation results and normalize the I-V curve so it passes through (0 V, 0 mA). We then bias the input to set the buffer in the high state and re-run this process to extract the Pullup I-V curve.

To generate the Rising and Falling high V-t waveforms, we take the V-t *.xnp file, connect an HB source with impedance Z_c to the input with the same DC bias, power level, frequency, and number of harmonics as with the generation and connect the output to an HB termination with impedance Z_c and a DC voltage bias of V_{cc}. We generate the time-domain voltage response of the output from the results of the simulation, separating this response into rising and falling portions. To generate the Rising and Falling low V-t waveforms, we change the DC voltage bias to *Gnd*. Next, we apply a linear transformation on all four waveforms to match the beginning and end points to the I-V data using load-line analysis as mentioned in Sec. 4.4. Finally, all of these curves can be tabulated and put into an IBIS file, ready for

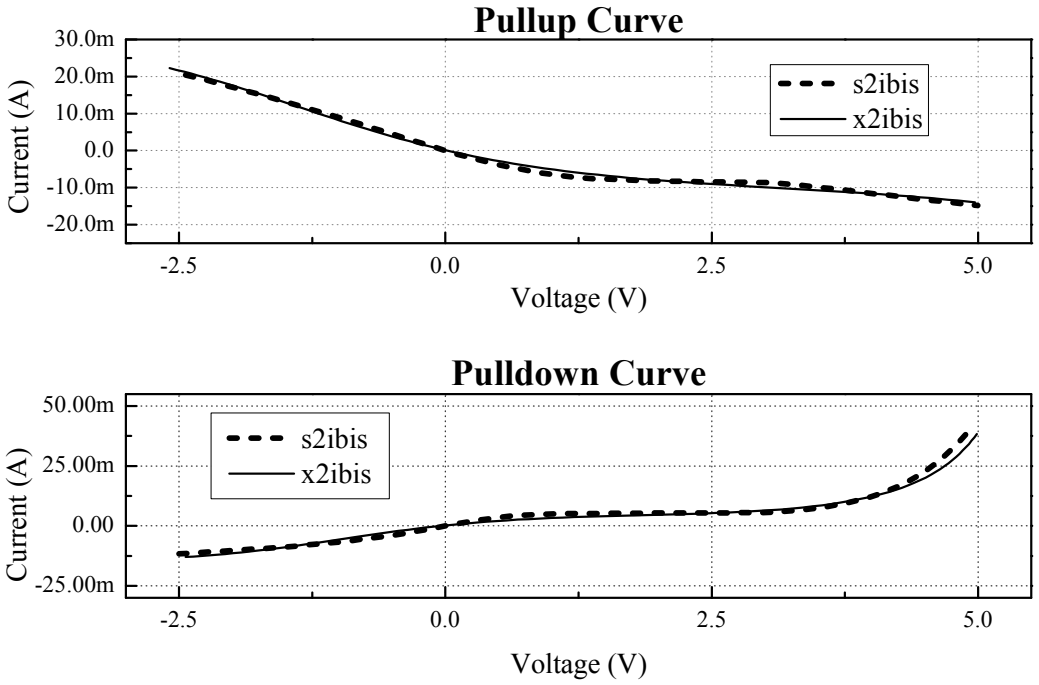

Figure 6.5: Comparison of I-V curves generated by x2ibis and s2ibis.

simulation in an EDA tool.

6.3 Example and Numerical Results

Figures 6.5 and 6.6 show a comparison between s2ibis and x2ibis for all of the I-V and V-t curves. As is shown, the results from both methods match reasonably well despite the approximations that were made in the generation in x2ibis. The I-V curve file generation used the transient simulation approximation from the IBIS Cookbook and the V-t curve file generation roughly approximated the ideal ramp input with a sinusoid. Last, Fig. 6.7 shows both IBIS files being used in a circuit simulation with a pseudo-random bit sequence as a source. The waveforms match well.

6.4 Comments and Future Work

We have utilized X-parameter measurements in the generation of an IBIS model, which is the current standard for modeling I/O buffer circuits. We

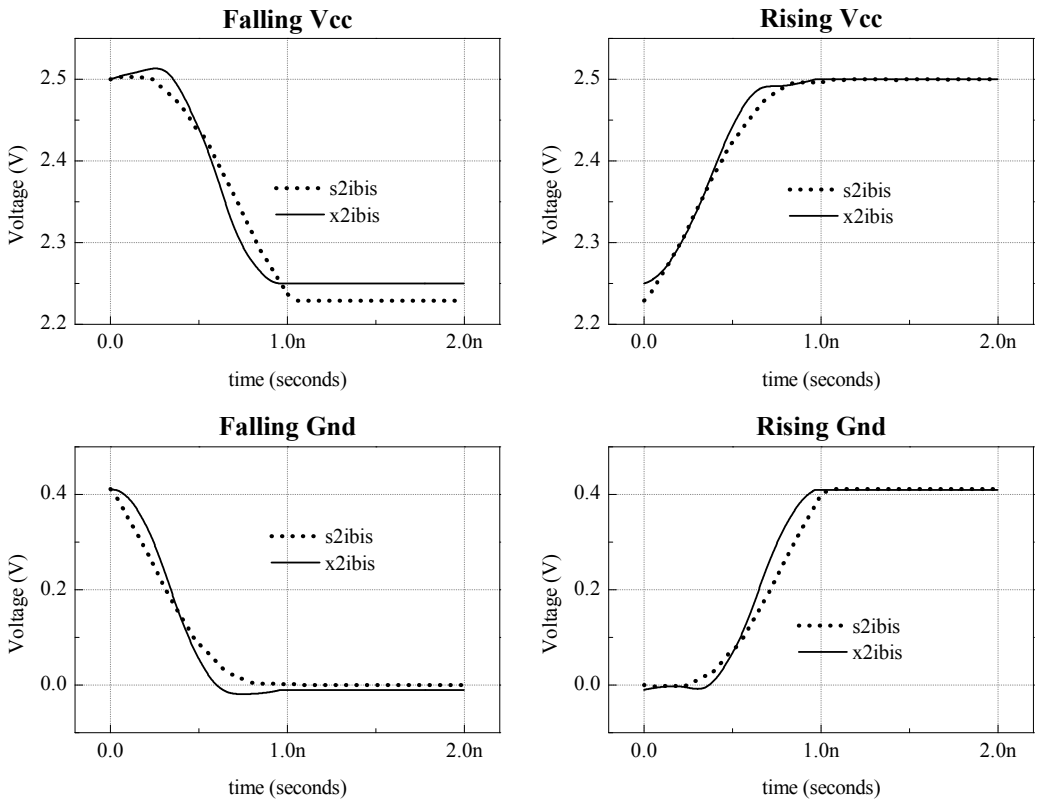

Figure 6.6: Comparison of V-t curves generated by x2ibis and s2ibis.

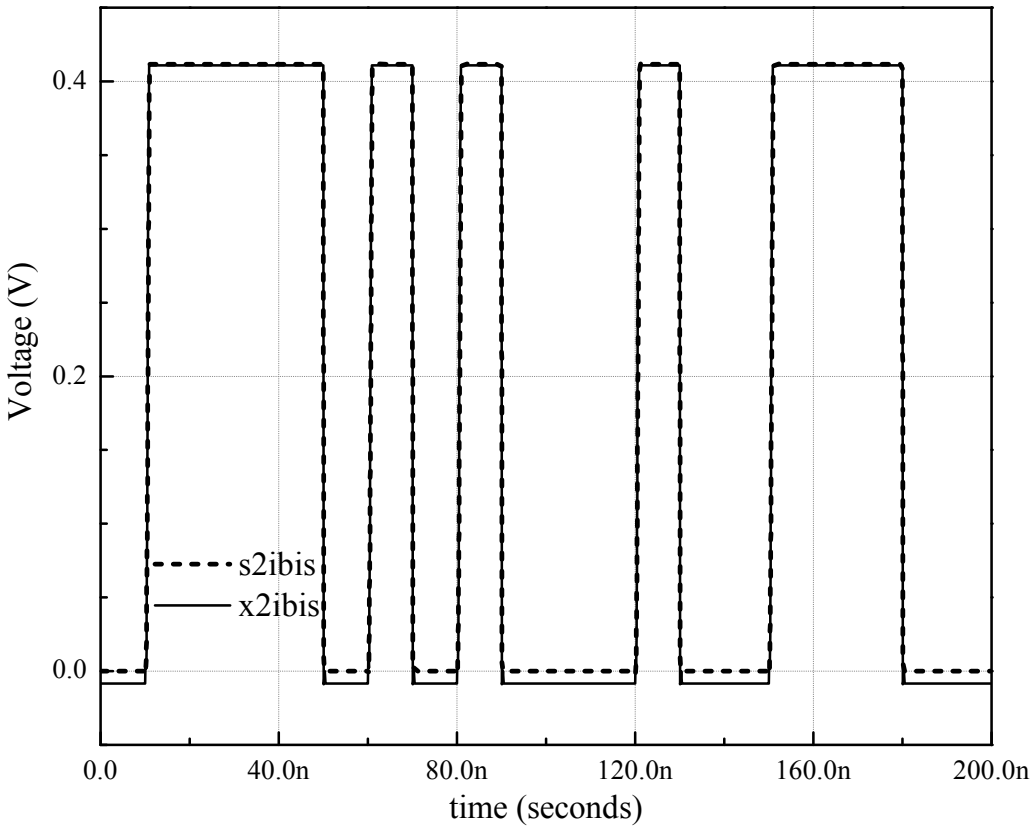

Figure 6.7: Comparison of results for IBIS models generated by x2ibis and s2ibis with pseudo-random bit sequence stimulus.

have demonstrated that this method, x2ibis, produces results that agree well with those generated using s2ibis. Thus, we have shown that the X-parameter formalism and the NVNA are both powerful tools for basic IBIS model generation. With the advent of the Algorithmic Modeling Interface (AMI), outlined in Sec. 4.5, the analog portion of an I/O buffer has been minimalized in the IBIS modeling flow. Therefore, it might not be necessary to be able to generate an IBIS model that is much more intricate than the one generated for the circuit in Fig. 6.2.

As for the x2ibis process, there is room for improvement. Thus far, the number of harmonics used in both the I-V and V-t tables has been chosen heuristically. A case study of the effect of the number of harmonics on the quality of the solution might yield some insights into the degree of nonlinearity of a particular class of buffer circuit. As for the approximation of the ideal step function for the stimulus in the V-t curve generation, there is another option. We can approximate a pulse from its Fourier series representation. This was attempted, but it did not produce good results for a reasonable number of harmonics because the behavior of the output waveform was dominated by the Gibbs phenomena that resulted from the limited number of harmonics. Last, x2ibis could be performed on actual X-parameter measurements from the laboratory gathered using an NVNA. Regardless, we have achieved the primary purpose of x2ibis, to show that all of the information contained in the analog portion of an IBIS model, particularly the V-t tables, can be extracted from an X-parameter model.

CHAPTER 7

DISCUSSION

"A theory is something nobody believes, except the person who made it. An experiment is something everybody believes, except the person who made it."
-Albert Einstein

7.1 Overview

The purpose of this dissertation has been to apply X-parameters to signal integrity applications. Throughout our work with X-parameters, we have learned that the biggest hurdle in using them is the challenge involved in developing a good understanding of how they are formulated and measured. Historically, entire senior-level undergraduate lectures and laboratory courses have been dedicated to the study and measurement of scattering parameters. Hence, it is very reasonable to treat X-parameters, a nonlinear superset of scattering parameters, as an advanced topic. We have provided an X-parameter primer as well as an example of measuring and using the X-parameters of an amplifier and simulating and using the X-parameters of a simple equalizer circuit. It is our hope that resources such as this dissertation and [12] will make future studies of X-parameters and nonlinear modeling less intimidating and more fruitful. When researchers have more knowledge of the X-parameter formalism, more problems can be formulated and solved using it.

The latency insertion method (LIM) is a linear numerical complexity, all-purpose circuit simulation tool, ideal for simulating large, high-speed circuits, which naturally have reactive elements. We have demonstrated lim2x as an X-parameter generation process with LIM that can handle large modern, high-frequency I/O buffer circuits. We then demonstrated how X-parameters can be used to generate Input/Output Buffer Information Spec-

ification (IBIS) models, the current standard for modeling I/O buffers.

7.2 Future Work

Looking back on the genesis of IBIS, it seems that its fundamental premise is that a buffer's behavior can be primarily described as DC, with the occasional transition to the opposite state. While this was a fairly justifiable sentiment in the early 1990s when IBIS was first created, it is becoming less true as we increase the transmission rates of high-speed links to tens of gigabits-per-second. The process x2ibis is valuable because IBIS is the current standard for modeling I/O buffers, but future work using X-parameters to model I/O buffers will benefit from including X-parameter measurements as part of a different equivalent circuit which acknowledges that a high-speed link operates at microwave frequencies.

When using scattering parameters in a transient simulator, the simulator can perform an inverse Fourier transform to extract the impulse response [7]. This impulse response can then be convolved with any arbitrary input to generate a result. Provided that scattering parameters are sampled or well-approximated from DC to the maximum frequency of the simulation, this method is accurate, albeit slow. A similar idea for transient simulation with an X-parameter model was pursued in [9], where the X-parameter of type FB was linearized and all of the nonlinear behavior was modeled in the existence of harmonics. We demonstrated in Sec. 3.6 that this approximation is not valid for modeling normal buffer operation.

Modeling the buffer as "almost linear" is not an effective long-term solution since the X-parameter formalism is fundamentally a bandpass model, but this property makes it ideal for HB or circuit envelope (CE) simulations [58]. Also shown in Sec. 3.6, HB simulations with X-parameter models are able to match the steady-state transient behavior of a buffer. These simulations were performed with simple sinusoidal input stimuli, but future work can leverage more elaborate circuit envelope (CE) simulation techniques to model more interesting stimuli, such as a pseudo-random bit sequence. The outputs of these simulations could be used to construct an eye diagram and calculate bit error rate (BER).

Also, signal integrity applications need not be limited to the single large-

tone X-parameter model. Multiple large-tone X-parameters can be generated if needed to simulate typical input signals to a circuit more accurately. X-parameters have also been extended to model long-term memory effects [12]. These extensions increase the flexibility of the X-parameter formalism and will prove valuable in its use in signal integrity applications.

APPENDIX

A.1 Using X-Parameters to Model a Varactor Diode

In this section, we will be describing X-parameter measurements made on a varactor diode. A varactor diode, pictured in Fig. A.1 is a diode whose capacitance changes as a function of the voltage across its terminals. When a *pn*-junction diode is reverse-biased, it creates a depletion layer that exhibits a charge-storage effect modeled by a junction capacitance C_j, which is a function of the reverse bias voltage V_R according to

$$C_j = \frac{C_{j0}}{\left(1 + \frac{V_R}{V_0}\right)^m} \tag{A.1}$$

where C_{j0} is the value of C_j for zero applied voltage, V_0 is the voltage across the *pn* junction with no external voltage applied, and m is the grading coefficient [59].

As can be seen from (A.1), the behavior of a varactor diode is nonlinear. Our goal is to characterize the nonlinear microwave behavior of a Skyworks SMV1235 varactor diode [60] using X-parameters. This varactor diode can be used as a reconfigurable element in an antenna. We will verify the X-

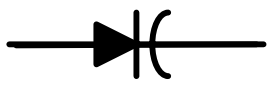

Figure A.1: A varactor diode. The diode, when reverse-biased, acts as a variable capacitor.

parameter measurements against the behavioral model of the varactor diode based on (A.1).

The varactor diode was placed in parallel to a connectorized microstrip line to allow for easy X-parameter measurement. The microstrip line height is 1.575 millimeters with a relative dielectric constant of 2.2. The connectorized varactor diode's X-parameters were measured in two different sweeps. The first sweep measured 11 harmonics at ten frequency points from 10 MHz to 100 MHz and at six power points from -5 to 20 dBm with an intermediate frequency bandwidth (IFBW) of 1 kHz. The second sweep measured 11 harmonics at 35 MHz and from -5 to 20 dBm with 1-dB steps with an intermediate frequency bandwidth (IFBW) of 10 kHz. In both sweeps, a bias tee was used to provide a DC bias of 3.25 V to reverse bias the varactor diode along with DC blocks at both test ports to prevent the DC power from saturating the receivers in the nonlinear vector network analyzer (NVNA). The calibration reference plane was set so as to remove the effects of the bias tee and the DC blocks.

These measurements were then used in a harmonic balance simulation to compare the X-parameter measurements to the equivalent circuit model provided by the vendor. The test setup of the vendor equivalent circuit is shown in Fig. A.2. The test setup of the X-parameter model is shown in Fig. A.3.

These test setups were both used in a harmonic balance (HB) simulation. The HB simulation contained one fundamental frequency at 35 MHz and it considered ten harmonics. The simulation converged for each model. Figure A.4 shows a plot comparing the magnitudes of the harmonic frequency components of the voltage at the output load port for each model.

As can be seen, the results using X-parameter model match closely to those of the vendor model for the first three harmonics and the fifth harmonic. The fourth harmonic differs by about an order of magnitude and the higher harmonics are higher than those predicted by the vendor model, albeit still very small. It is hard to tell if this high-frequency discrepancy is due to the noise floor of the measurement system or to the limited modeling range of the vendor model. Regardless, this actual X-parameter measurement data of the varactor diode can be used in larger circuits to determine the behavior of an entire microwave system.

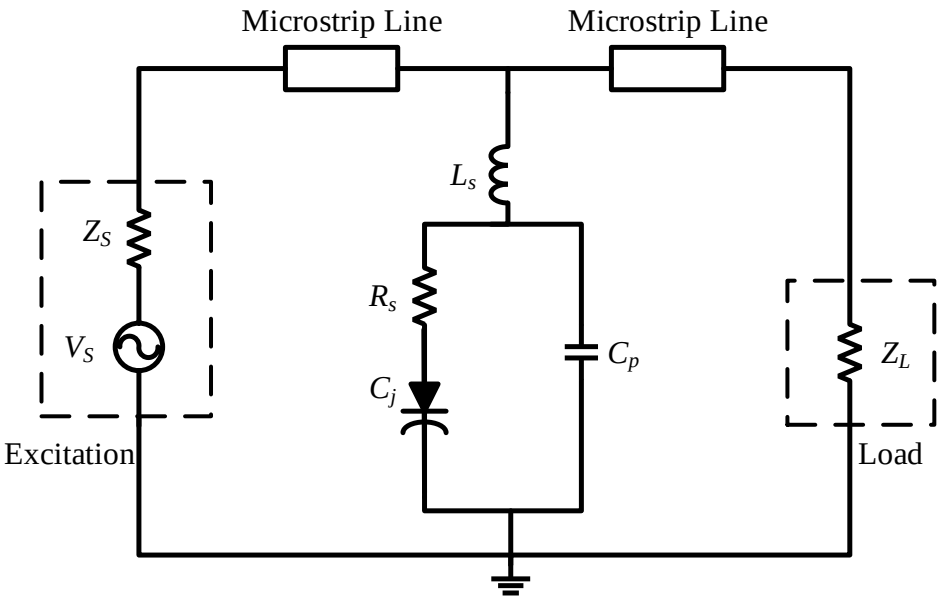

Figure A.2: Simulation setup for the complete varactor diode circuit connected in parallel with a microstrip line with excitation and load. The values for the varactor diode packaging parameters are $C_p = 2.15$ pF, $R_s = 0.6\ \Omega$, and $L_s = 0.7$ nH. The varactor diode parameters are $C_{j0} = 15.85$ pF, $V_0 = 8.78$ V, and $m = 4.57$. Each microstrip line has a height of 1.575 mm and a relative dielectric constant of 2.2. The signal traces of each portion of the microstrip line have a width of 4.9 mm and a length of 15 mm. The port impedances Z_S and Z_L are both 50 Ω. The source provided 35 MHz stimulus at 10 dBm input power. The source also contains a 3.25 V DC offset to reverse-bias the varactor diode.

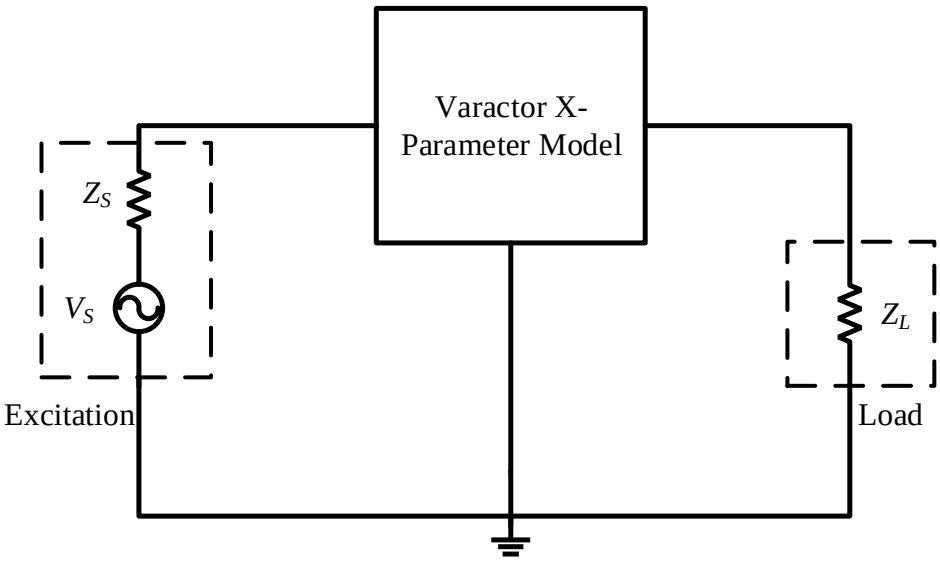

Figure A.3: Simulation setup for using X-parameter varactor diode measurements to compare with varactor behavior model. The port impedances Z_S and Z_L are both 50 Ω. The source provided 35 MHz stimulus at 10 dBm input power. The source also contains a 3.25 V DC offset to correspond to the circumstances under which the X-parameter model was generated.

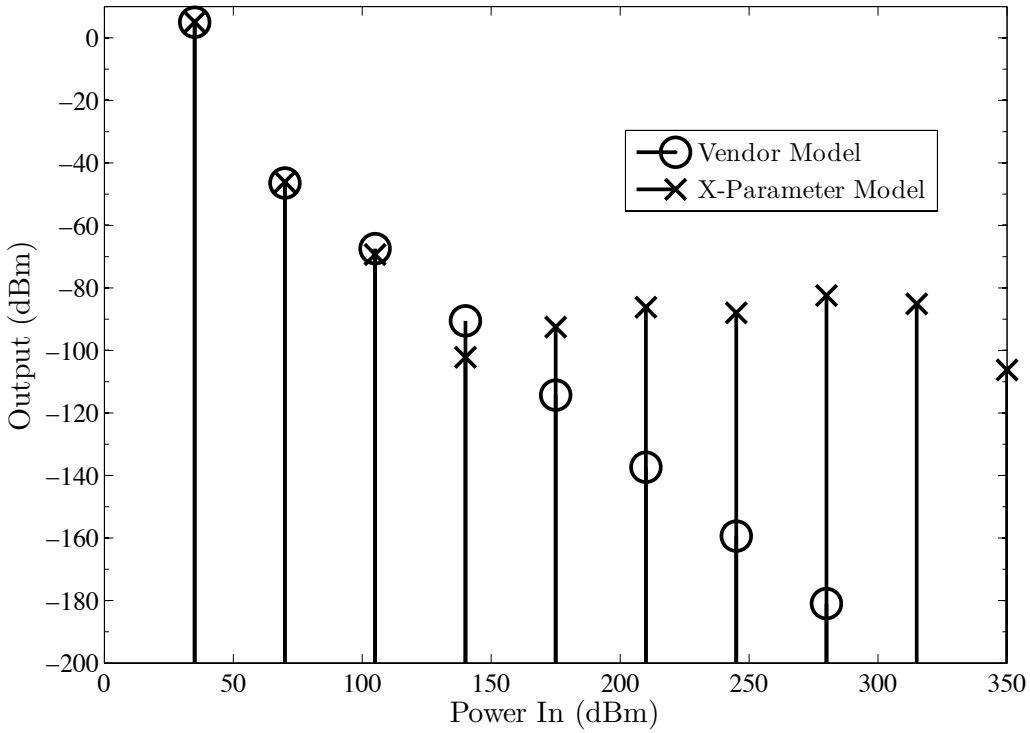

Figure A.4: Results comparing the magnitudes of the harmonic frequency components of the voltage at the output load port for each model.

REFERENCES

[1] E. Bogatin, *Signal Integrity – Simplified.* Upper Saddle River, NJ: Prentice Hall, 2004.

[2] J. A. Kong, *Electromagnetic Wave Theory.* Cambridge, MA: EMW Publishing, 2000.

[3] P. Milosevic, "Crosstalk mitigation of high-speed interconnects using modal signaling," Ph.D. dissertation, University of Illinois at Urbana-Champaign, 2011.

[4] S. H. Hall and H. L. Heck, *Advanced Signal Integrity for High-Speed Digital Designs.* Hoboken, NJ: Wiley-IEEE Press, 2009.

[5] The IBIS Open Forum, "I/O Buffer Information Specification Version 6.0." Ratified September 20, 2013. [Online]. Available: http://www.eigroup.org/ibis/

[6] A. Muranyi, "What's wrong with IBIS?" presentation at IBIS Summit, DesignCon, Santa Clara, CA, January 2013.

[7] J. E. Schutt-Aine and R. Mittra, "Scattering parameter transient analysis of transmission lines loaded with nonlinear terminations." *IEEE Transactions on Microwave Theory and Techniques*, vol. 36, no. 3, pp. 529–536, 1988.

[8] Agilent Technologies, Inc., "X-Parameters Trademark Usage, Open Documentation and Partnerships." [Online]. Available: http://www.home.agilent.com/agilent/editorial.jspx?cc=US\&lc=eng\&ckey=1822138\&id=1822138\&cmpid=zzfindeesof-x-parameters-info

[9] J. E. Schutt-Aine, P. Milosevic, and W. T. Beyene, "Modeling and simulation of high speed I/O links using X parameters," in *2010 IEEE 19th Conference on Electrical Performance of Electronic Packaging and Systems, EPEPS 2010*, 2011.

[10] Agilent Technologies, *Agilent Nonlinear Vector Network Analyzer (NVNA)*, 2011.

[11] J. Schutt-Aine, "Latency insertion method (LIM) for the fast transient simulation of large networks," *IEEE Trans. Circuits Syst. I, Fundam. Theory Appl. (USA)*, vol. 48, pp. 81–89, 2001.

[12] D. E. Root, J. Verspecht, J. Horn, and M. Marcu, *X-Parameters: Characterization, Modeling, and Design of Nonlinear RF and Microwave Components*. Cambridge: Cambridge University Press, 2013.

[13] S. J. Franke, *ECE 453 Wireless Communication Circuits Course Notes, Fall 2013*. Class notes for ECE 453, Department of Electrical and Computer Engineering, University of Illinois at Urbana-Champaign, 2013.

[14] D. M. Pozar, *Microwave Engineering*, 4th ed. Hoboken, NJ: Wiley, 2012.

[15] J. P. Dunsmore, *Handbook of Microwave Component Measurements: With Advanced VNA Techniques*. Chichester, West Sussex, United Kingdom: John Wiley & Sons, Inc., 2012.

[16] J. Verspecht and D. E. Root, "Polyharmonic distortion modeling," *IEEE Microwave Magazine*, vol. 7, no. 3, pp. 44–57, 2006.

[17] D. Root, J. Xu, J. Horn, M. Iwamoto, and G. Simpson, "Device modeling with NVNAs and X-parameters," in *2010 Workshop on Integrated Nonlinear Microwave and Millimeter-Wave Circuits (INMMIC)*, 2010, pp. 12–15.

[18] J. Verspecht, D. E. Root, J. Wood, and A. Cognata, "Broad-band, multiharmonic frequency domain behavioral models from automated large-signal vectorial network measurements," in *IEEE MTT-S International Microwave Symposium Digest*, 2005, pp. 1975–1978.

[19] D. E. Root, J. Verspecht, D. Sharrit, J. Wood, and A. Cognata, "Broad-band poly-harmonic distortion (PHD) behavioral models from fast automated simulations and large-signal vectorial network measurements," in *IEEE Transactions on Microwave Theory and Techniques*, 2005, pp. 3656–3664.

[20] L. Betts, "X-parameters and nonlinear vector network analysis (NVNA) going beyond S parameters," May 2009. [Online]. Available: http://www.ieee-sem.org/ChapterIV/090504_LorenBetts_NVNA.pdf

[21] M. E. L. Yaagoubi, G. Neveux, D. Barataud, J. Nebus, and J. Verspecht, "Accurate phase measurements of broadband multitone signals using a specific configuration of a large signal network analyzer," in *IEEE MTT-S International Microwave Symposium Digest*, 2006, pp. 1448–1451.

[22] S. El-Rabaie, V. Fusco, and C. Stewart, "Harmonic balance evaluation of nonlinear microwave circuits — A tutorial approach," *Education, IEEE Transactions on*, vol. 31, no. 3, pp. 181–192, 1988.

[23] "Guide to harmonic balance simulation in RFDE," Agilent Technologies, Inc., Tech. Rep., May 2007.

[24] S. A. Maas, *Nonlinear Microwave and RF Circuits*, 2nd ed. Boston, MA: Artech House, 2003.

[25] L. W. Nagel and D. Pederson, "SPICE (Simulation Program with Integrated Circuit Emphasis)," EECS Department, University of California, Berkeley, Tech. Rep., Apr 1973. [Online]. Available: http://www.eecs.berkeley.edu/Pubs/TechRpts/1973/22871.html

[26] A. Vaezi, A. Abdipour, and A. Mohammadi, "Nonlinear analysis of microwave amplifiers excited by multicarrier modulated signals using envelop transient technique," *Analog Integrated Circuits and Signal Processing*, vol. 72, no. 2, pp. 313–323, 2012.

[27] "Circuit envelope simulation," Agilent Technologies, Inc., Palo Alto, CA, Tech. Rep., September 2004.

[28] G. Gonzalez, *Microwave Transistor Amplifiers: Analysis and Design*, 2nd ed. Upper Saddle River, NJ: Prentice Hall, 1997.

[29] Mini-Circuits, "Surface mount monolithic amplifier," Gali-1+ datasheet. [Online]. Available: http://www.minicircuits.com/pdfs/GALI-1+.pdf

[30] Mini-Circuits, "Evaluation board and circuit," TB-409-1+ datasheet. [Online]. Available: http://www.minicircuits.com/pcb/WTB-409-1+_P02.pdf

[31] A. Saleh, "Frequency-independent and frequency-dependent nonlinear models of TWT amplifiers," *Communications, IEEE Transactions on*, vol. 29, no. 11, pp. 1715–1720, 1981.

[32] P. Singerl and G. Kubin, "Constructing memory-polynomial models from frequency-dependent AM/AM and AM/PM measurements," in *Circuits and Systems, 2007. MWSCAS 2007. 50th Midwest Symposium on*, 2007, pp. 321–324.

[33] T. M. Comberiate and J. E. Schutt-Ainé, "Modeling I/O buffers using X-parameters," in *22st IEEE Conference on Electrical Performance of Electronic Packaging and Systems, EPEPS-2013*, 2013, pp. 25–28.

[34] *Agilent Advanced Design System*, Version 2013.06. Copyright 1983-2013, Agilent Technologies.

[35] K. Yee, "Numerical solution of initial boundary value problems involving Maxwell's equations in isotropic media," *IEEE Transactions on Antennas and Propagation*, vol. AP-14, no. 3, pp. 302–307, 1966.

[36] J. Schutt-Aine, "Stability analysis for semi-implicit LIM algorithm," in *APMC 2009 — Asia Pacific Microwave Conference 2009*, 2009, pp. 155–158.

[37] T. Sekine and H. Asai, "Nonlinear block-type leapfrog scheme for the fast simulation of multiconductor transmission lines with nonlinear drivers and terminations," in *Electrical Performance of Electronic Packaging and Systems (EPEPS), 2012 IEEE 21st Conference on*, 2012, pp. 284–287.

[38] Z. Deng and J. Schutt-Aine, "Stability analysis of latency insertion method (LIM)," in *IEEE Topical Meeting on Electrical Performance of Electronic Packaging*, 2004, pp. 167–170.

[39] S. N. Lalgudi and M. Swaminathan, "Analytical stability condition of the latency insertion method for nonuniform GLC circuits," *IEEE Transactions on Circuits and Systems II: Express Briefs*, vol. 55, no. 9, pp. 937–941, 2008.

[40] J. Schutt-Aine, "Stability analysis of the latency insertion method using a block matrix formulation," in *2008 Electrical Design of Advanced Packaging and Systems Symposium, IEEE EDAPS 2008 — Proceedings*, 2008, pp. 155–158.

[41] P. Goh and J. E. Schutt-Aine, "Latency insertion method (LIM) for CMOS circuit simulations with multi-rate considerations," in *2011 IEEE 20th Conference on Electrical Performance of Electronic Packaging and Systems, EPEPS-2011*, San Jose, CA, 2011, pp. 125–128.

[42] H. Shichman and D. Hodges, "Modeling and simulation of insulated-gate field-effect transistor switching circuits," *Solid-State Circuits, IEEE Journal of*, vol. 3, no. 3, pp. 285–289, 1968.

[43] P. K. Goh, "A fast multi-purpose circuit simulator using the latency insertion method," Ph.D. dissertation, University of Illinois at Urbana-Champaign, 2012.

[44] J. E. Schutt-Aine, J. Tan, P. Liu, F. Al-Hawari, and A. Varma, "IBIS modeling using latency insertion method (LIM)," in *2012 IEEE 16th Workshop on Signal and Power Integrity, SPI 2012 — Proceedings*, 2012, pp. 97–100.

[45] IBIS Open Forum. [Online]. Available: http://www.vhdl.org/ibis/

[46] Y. Wang and H. N. Tan, "The development of analog SPICE behavioral model based on IBIS model," in *Proceedings of the Ninth Great Lakes Symposium on VLSI, GLS '99*, 1999, pp. 101–104.

[47] IBIS Open Forum, "IBIS 5.0 and IBISCHK5." [Online]. Available: http://www.eda.org/ibis/info/info_ibis.html

[48] IBIS Open Forum, "IBIS modeling cookbook for IBIS version 4.0," [Online]. Copyright 2005 Government Electronics and Information Technology Association and the IBIS Open Forum.

[49] s2ibis3 v1.1. Copyright North Carolina State University. Last modified: March 27, 2006.

[50] C. Warwick and F. Rao, "Explore the SERDES design space using the IBIS AMI channel simulation flow," Agilent EEsof EDA, Tech. Rep., 2012.

[51] W. Katz, M. Steinberger, and T. Westerhoff, "IBIS-AMI terminology overview," in *DAC 2009 IBIS Summit*, 2009.

[52] T. Westerhoff, A. Hawes, M. Steinberger, K. Dramstad, W. Katz, and B. Katz, "Predicting BER with IBIS-AMI: Experiences correlating SerDes simulations and measurement," in *DesignCon 2010*, 2010.

[53] C. Warwick, "Four things that drove me nuts about IBIS 5.1," September 2012, Signal Integrity Blog, Agilent EEsof. [Online]. Available: http://signal-integrity.tm.agilent.com/2012/four-things-that-drove-me-nuts-about-ibis-5-1/

[54] S. Palermo, "High-speed serial I/O design for channel-limited and power-constrained systems," in *CMOS Nanoelectronic Analog and RF VLSI Circuits*, K. Iniewski. New York, NY: McGraw-Hill, 2011, 289-336.

[55] R. G. Lyons, *Understanding Digital Signal Processing*, 2nd ed. Upper Saddle River, NJ: Pearson Education, Inc., 2004.

[56] A. Brambilla and D. D. Amore, "Simulation errors introduced by the SPICE transient analysis," *IEEE Transactions on Circuits and Systems I: Fundamental Theory and Applications*, vol. 40, no. 1, pp. 57–60, 1993.

[57] P. Goh, J. E. Schutt-Aine, D. Klokotov, J. Tan, P. Liu, W. Dai, and F. Al-Hawari, "Partitioned latency insertion method with a generalized stability criteria," *IEEE Transactions on Components, Packaging and Manufacturing Technology*, vol. 1, no. 9, pp. 1447–1455, 2011.

[58] A. Soury, E. Ngoya, and J. Rousset, "Behavioral modeling of RF and microwave circuit blocks for hierarchical simulation of modern transceivers," in *Microwave Symposium Digest, 2005 IEEE MTT-S International*, 2005.

[59] A. S. Sedra and K. C. Smith, *Microelectronic Circuits*, 5th ed. New York: Oxford University Press, 2004.

[60] Skyworks, "SMV123x series: Hyperabrupt junction tuning varactors," datasheet, June 2012. [Online]. Available: http://www.minicircuits.com/pcb/WTB-409-1+_P02.pdf